Continuous GPS Carrier-Phase Time Transfer

by

Jian Yao

B.S., Nanjing University, 2009

M.S., University of Colorado at Boulder, 2012

A thesis submitted to the

Faculty of the Graduate School of the

University of Colorado in partial fulfillment

of the requirements for the degree of

Doctor of Philosophy

Department of Physics

2014

This thesis entitled:
Continuous GPS Carrier-Phase Time Transfer
written by Jian Yao
has been approved for the Department of Physics

_____
Prof. Judah Levine

_____
Prof. Neil Ashby

Date_____

The final copy of this thesis has been examined by the signatories, and we find that both the content and the form meet acceptable presentation standards of scholarly work in the above mentioned discipline.

Yao, Jian (Ph.D., Physics)

Continuous GPS Carrier-Phase Time Transfer

Thesis directed by Prof. Judah Levine

Time transfer (TT) is the process of transmitting a timing signal from one place to another place. It has applications to the formation and realization of Coordinated Universal Time (UTC), telecommunications, electrical power grids, and even stock exchanges. TT is the actual bottleneck of the UTC formation and realization since the technology of atomic clocks is almost always ahead of that of TT. GPS carrier-phase time transfer (GPSCPTT), as a mainstream TT technique accepted by most national timing laboratories, has suffered from the day-boundary-discontinuity (day-BD) problem for many years. This makes us difficult to observe a remote Cesium fountain clock behavior even after a few days. We find that day-BD comes from the GPS code noise. The day-BD can be lowered by ~40% if more satellite-clock information is provided and if a few GPS receivers at the same station are averaged. To completely eliminate day-BD, the RINEX-Shift (RS) and revised RS (RRS) algorithms have been designed. The RS/RRS result matches the two-way satellite time/frequency transfer (TWSTFT) result much better than the conventional GPSCPTT result. With the RS/RRS algorithm, we are able to observe a remote Cesium fountain after half a day. We also study the BD due to GPS data anomalies (anomaly-BD). A simple curve-fitting strategy can eliminate the anomaly-BD. Thus, we achieve continuous GPSCPTT after eliminating both day-BD and anomaly-BD.

Dedication

To all I love.

Acknowledgements

I want to take this opportunity to acknowledge my debts to all those who helped me with my Ph.D. study. There are so many people to thank and I apologize in advance to those whose names I failed to recognize.

First, I thank my advisor, Dr. Judah Levine, for all his support. He knows almost everything about timing, such as GPS carrier phase and common-view time transfer, time scale and atomic clocks, network synchronization, frequency stability analysis, time/frequency measurements, and two-way satellite time/frequency transfer (TWSTFT), just to name a few. It is a great joy to discuss scientific problems with him because he is so knowledgeable. I learn a lot of things after talking with him. Sometimes, I'm a little worried about how to explain the complicated research details to him. But he gets my point immediately. However, this does not mean that he is condescending. Instead, he is a patient listener and gives me very helpful suggestions. When I come across some difficulties in research, he always encourages me. Judah has also introduced me to many well-known people in this field. Thus, I feel there is a think tank just behind me whenever I confront the unknown world.

Special thanks go to Dr. Marc Weiss (NIST Boulder). He introduced me to this intriguing research field. Without him, I might never have known anything about time transfer and GPS. He taught me a lot, from the RINEX file format to the GPS common-view, from programming skills to the time scale. He is always patient to explain everything to me, even though I sometimes ask silly questions.

I am also deeply grateful to Victor Zhang (NIST Boulder). He is an expert on TWSTFT and GPS time transfer. We have had a lot of discussions about the error sources in TWSTFT and the problems with GPS time transfer. He has always been available to help me, from answering questions about my research to advising me on my personal life. He encouraged me a lot and introduced my research work to other people.

I also want to thank Dr. Tom Parker (NIST Boulder). He helped me a lot with the analysis of the Cesium fountain data and also gave many constructive and practical suggestions on my research. Dr. Neil Ashby is another person that I am very grateful to. He explained the GPS relativistic effects to me using the easy-to-understand language. I also thank Dr. Stefania Romisch (NIST Boulder) for her generosity in providing me with summer funding. Thanks also go to Dr. Dennis Akos. He shared the Novatel Grafnav software with me and explained how to use it in great detail. Trudi Peppler (NIST Boulder) is thanked for sharing PCWork, a software package for the frequency-stability analysis. The clusters at JILA enabled me to do a lot of calculations simultaneously, which reduced the time of my Ph.D. career. Thus, I am grateful to all the staff members of the JILA computing group.

There are also many people outside of Boulder to thank. Dr. Francois Lahaye (Natural Resources Canada) and Dr. Pascale Defraigne (Royal Observatory of Belgium) are thanked for providing the NRCan PPP software and the Atomium PPP software. Without these software packages, I wouldn't have been able to do the research presented here. Dr. Demetrios Matsakis and Stephen Mitchell (both from the United States Naval Observatory) are thanked for very helpful discussions on GPS carrier-phase time transfer. I also thank Dr. Stefan Weyers (PTB, Germany), and Dr. Michel Abgrall (OP, France) for sharing their Cesium fountain data. IGS is acknowledged for providing GPS tracking data, station coordinates, and satellite ephemerides. Also thank those people who maintain the GPS receivers in NIST, PTB, USNO, OP, NICT, and AMC.

I also want to take this opportunity to thank my Comps III and thesis committee: Dr. Judah Levine, Dr. Neil Ashby, Dr. Peter Bender, Dr. Penina Axelrad (Department of Aerospace Engineering Sciences), and Dr. Dennis Akos (Department of Aerospace Engineering Sciences). It is my great honor to have them serve on my thesis committee. Their comments on my Comps III are very helpful to my later research. Julie Phillips (JILA Scientific Communications Office) is also thanked for spending her precious time proofreading this thesis.

Finally, I want to express my special thanks to my parents and girlfriend, Xiaorong Liu. Their love and support are a constant inspiration for my personal development.

31 October 2014 Jian Yao (尧剑)

Contents

Chapter

Tables

Table

Figures

Figure

Chapter 1

Introduction

1.1 Introduction to Time Transfer

Time is a dimension and measure in which events can be ordered from the past through the present and into the future. Periodic behaviors are used to measure time. In ancient times, human beings observed that the sun rises and sets again and again. Since then, humans have defined the time range between sunset and the next sunset as one day, or 24 hours. Much later, when the pendulum clock was invented, it provided better timing accuracy and precision. However, the same pendulum clock runs at slightly different rates when it operates at different places on the earth, because the acceleration due to the gravitational force is not exactly a constant.

In the modern world, we look for precise periodic behaviors or precise frequency sources for timekeeping. Quantum mechanics tells us that the transition between two atomic energy levels occurs at a specific frequency that can be used to build an unprecedentedly precise clock [1–5]. Since the quantum transition would be the same for any identical atom, we can, in principle, replicate the same clock

anywhere in the world. However, in practice, different environments (e.g., the magnetic field) lead to slightly different quantum transition frequencies [1–5]. Then new questions regarding clocks arise: which clock should be chosen as the standard clock? If this standard clock does not work, what shall we do? The robust solution to these questions is the establishment of a world time scale known as "Coordinated Universal Time (UTC)," which is formed by hundreds of clocks. In this way, we no longer need to be worried about whether a specific clock is working properly. The problem with this solution is that we have to gather time information of all the clocks to do averaging. So we need to transmit the time information of each clock to a central station. Comparing clocks within a laboratory can be done by many fancy techniques [6–9]. However, comparing clocks between laboratories is almost always a bottleneck of the world time formation. The process of transmitting the time information between laboratories is called "Time Transfer." As we can see from the above, time transfer is central to the formation and maintenance of a world time scale [10–12]. Without good time transfer, a precise clock would no longer be able to provide precise time information to other places.

Time transfer is also widely used whenever a reference time is required. For example, in the field of telecommunications, if the receiver is not synchronized to the transmitter, then slips (either overflows or underflows) will occur and degrade performance. The better the time transfer is, the smaller the bit error rate (BER) in the telecommunication link is. If we instead keep the same BER for the telecommunication link, then a better time transfer leads to a wider bandwidth [13].

As another example, if the clocks of generators are not well synchronized in an electrical power grid, then alternating currents with different phases from different generators will be added together, leading to a smaller amplitude than if the currents all had the same phase. Thus we lose power because of non-synchronization of time. The accurate and precise timing is also required in the stock market. Without good clock synchronization, you may pay for stocks that do not exist because they were already sold out a millisecond earlier. This kind of situation leads to chaos in a stock exchange. In fact, the stock market must be shut down if synchronization with the standard time fails. Precise time transfer also has applications in the field of fundamental research. A good example is the neutrino speed-measurement experiment. Since a neutrino flies at almost the speed of light, a few nanoseconds of time-transfer error can "make" the neutrino travel faster than light [14]. Nanosecond-level time-transfer accuracy is required in such state-of-the-art experiments.

Thus, we clearly see that time transfer is an old, but very important and very dynamic, research field. Time transfer affects world time formation, people's daily life and fundamental physical science.

Chapter 1 of this thesis is organized as follows: I first introduce frequency stability analysis and GPS principles in Sections 1.2 and 1.3. Then I review the mainstream time transfer techniques in Section 1.4. Section 1.5 discusses GPS carrier-phase time transfer, a widely used precise time-transfer technique in detail.

1.2 Frequency Stability Analysis[1]

A frequency source has a sine wave output signal given by

$$V(t) = [V_0 + \varepsilon(t)]sin[2\pi\nu_0 t + \phi(t)], \tag{1.1}$$

where V_0 is the nominal peak output voltage, $\varepsilon(t)$ is the amplitude deviation, ν_0 is the nominal frequency, and $\phi(t)$ is the phase deviation. The actual output-time error (or time offset) from the frequency source is $x(t) = \phi(t)/(2\pi\nu_0)$. For the analysis of frequency stability, we are concerned primarily with the $\phi(t)$ term. The instantaneous frequency is

$$\nu(t) = \nu_0 + \frac{1}{2\pi}\frac{d\phi}{dt}. \tag{1.2}$$

We define the fractional frequency as

$$y(t) = \frac{\Delta f}{f} = \frac{\nu(t)-\nu_0}{\nu_0} = \frac{1}{2\pi\nu_0}\frac{d\phi}{dt} = \frac{dx}{dt}. \tag{1.3}$$

Experimentally, we measure $x(t)$ or $y(t)$ every τ_0 seconds. τ_0 is called the data-sampling or measurement interval [15, Chapter 3].

A frequency source typically has the following noise types: white phase-modulation (PM) noise, flicker PM noise, white frequency-modulation (FM) noise, flicker FM noise, random walk FM, or flicker walk FM. Figure 1.1 shows examples of the last four noise types. In order to analyze the frequency stability of a frequency source, we introduce two approaches next.

The first approach is to characterize frequency stability in the frequency domain in terms of a power spectral density (PSD) that describes the intensity of

[1] This section is mainly based on "W. J. Riley, Handbook of frequency stability analysis, NIST Special Publication 1065, 2008" [15].

the frequency (or phase) fluctuations as a function of Fourier frequency. The other approach is to characterize frequency stability in the time domain based on the statistics, i.e., typically some type of variance, of the frequency (or phase) fluctuation as a function of time.

Frequency-domain analysis or spectral analysis can be done by doing a fast Fourier transform (FFT) on the time domain data. This analysis identifies the periodic components in the data very well. It is most often used to characterize the short-term (< 1 s) fluctuations of a frequency source. A frequency domain analysis can also distinguish the noise type. According to Section 3.2 of Reference [15], all noise types can be modeled by the form $S_y(f) \propto f^{\alpha}$, where $S_y(f)$ is the one-sided power spectral density of y, the fractional frequency fluctuations; f is the Fourier frequency; and α is the exponent of the power law noise process, which can be used to distinguish the noise type. Table 1.1 shows the relationship between noise type and the value of α.

Although frequency-domain analysis and time-domain analysis are equivalent in principle, time-domain analysis is usually preferred in the field of time transfer because of measurement and/or analysis convenience and tradition. In addition, time-domain analysis is usually used to provide information about the statistics of frequency source instability over a long interval (> 1 s). Because of these advantages, the remainder of this section will discuss time-domain analysis.

Time domain analysis is typically done using some type of variance. Before diving into the details of variance, we first introduce the concept of averaging time.

Although we measure $x(t)$ or $y(t)$ every τ_0 seconds experimentally, statistically, we may be more interested in the behavior of $x(t)$ or $y(t)$ with some other time interval. We define the time interval that we are statistically interested in as the averaging time $\tau = m\tau_0$, where m is typically an integer (otherwise we do not have the corresponding measured data). Next, we discuss all types of variance assuming that we have the fractional frequency value y_i every τ seconds, rather than every τ_0 seconds.

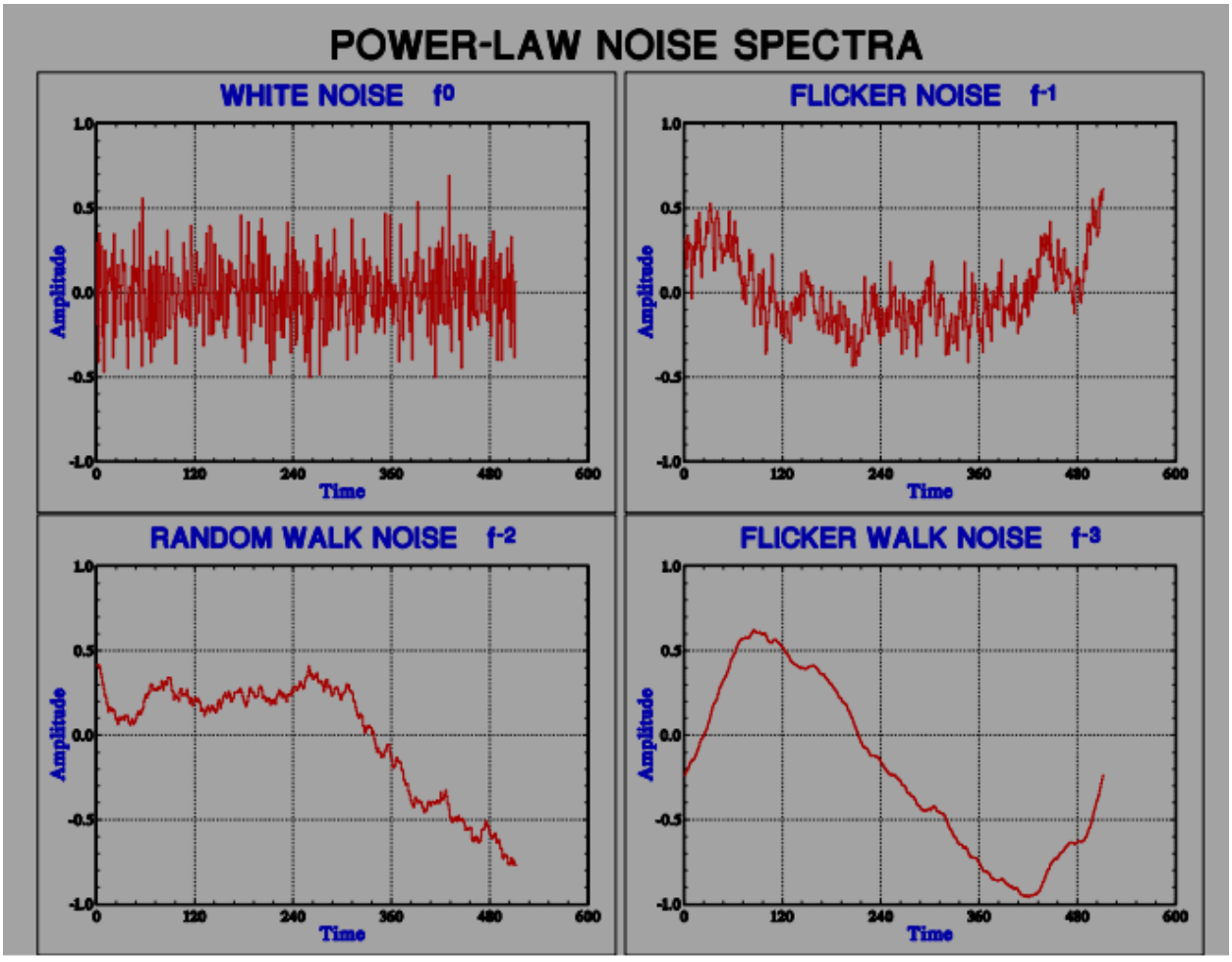

Figure 1.1. Examples of noise types, from [15].

Table 1.1. Spectral characteristics of noise types [15].

Noise Type	α
White PM	2
Flicker PM	1
White FM	0
Flicker FM	-1
Random Walk FM	-2
Flicker Walk FM	-3
Random Run FM	-4

The standard variance $s^2 = \frac{1}{N-1}\sum_{i=1}^{N}(y_i - \overline{y})^2$ is widely used in statistics. So one may think that the standard variance is good enough to describe the time-domain noise behavior. Although the standard variance is convergent for white PM, flicker PM and white FM, it is nonconvergent for the noise types of flicker FM and random walk FM [16], which are common in the H-maser frequency standard. The blue curve in Figure 1.2 illustrates the nonconvergence of the standard deviation for flicker FM noise. Here, we keep the averaging time τ a constant. As we increase the number of data points from 10 to 1000, the standard deviation (blue curve) increases from 1.5 to 2.8. However, we know the noise level is the same no matter how many data points we have. In other words, the deviation should be independent of the number of data points, if this deviation is a good indicator of noise level. Obviously, the standard deviation is not a good indicator. The problem with the standard deviation stems from its use in describing the deviations from the average, which is not stationary for the more divergent noise types.

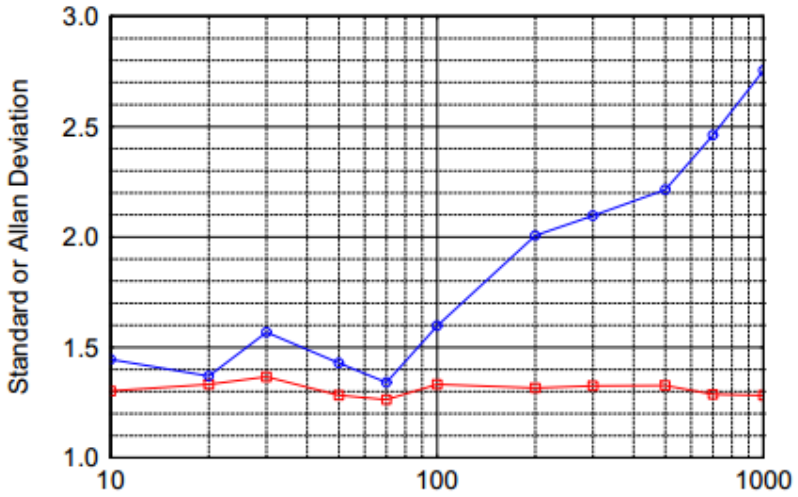

Figure 1.2. Convergence of standard and Allan deviation for flicker FM noise [15].

To solve this problem, David Allan introduced the Allan variance,

$$\sigma_y^2(\tau) = \frac{1}{2(N-1)} \sum_{i=1}^{N-1} (y_{i+1} - y_i)^2, \tag{1.4}$$

which uses the first differences of the fractional frequency values, rather than the differences between the fractional frequency values and the average value. The Allan variance is independent of the number of samples for flicker FM (see the red curve in Figure 1.2) and random walk FM. This independence means that the Allan variance well characterizes the stability of a frequency source in the time domain. Another property of the Allan variance is that it was designed to be the same as the standard variance for white FM noise. In addition, if the fractional frequency y has a periodic behavior with a period of T, then we can observe a bump at the averaging time of $T/2$ in the "log($\sigma_y(\tau)$)-log(τ)" diagram. (Notice that $\sigma_y(\tau) = \sqrt{\sigma_y^2(\tau)}$ and it is called the Allan deviation). Finally, the noise type can be distinguished by the slope

of the "log($\sigma_y(\tau)$)-log(τ)" diagram, as shown in Figure 1.3. There, the white FM has a slope of $-1/2$, while the flicker FM has a slope of 0.

However, the Allan deviation is not sufficient to distinguish white PM from flicker PM. The modified Allan deviation, $Mod\sigma_y(\tau)$, was designed to solve this ambiguity. The slope of the white PM becomes $-3/2$ by using the modified Allan deviation, while the slope of the flicker PM remains -1. The modified total deviation provides improved confidence at long averaging times. The time deviation, $\sigma_x(\tau) \stackrel{\text{def}}{=} \frac{\tau}{\sqrt{3}} \cdot Mod\sigma_y(\tau)$, is a measure of time stability based on the modified Allan deviation. Its unit is a second, instead of "1" as in Allan deviation. For details about these updated versions of Allan deviation, please see [15].

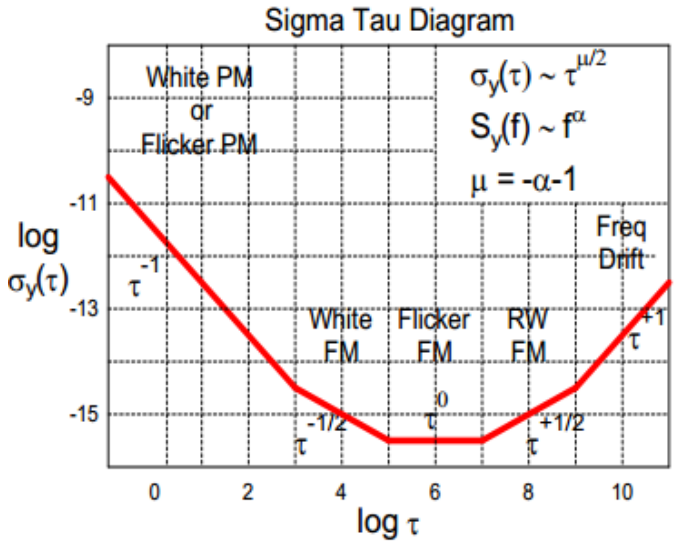

Figure 1.3. log($\sigma_y(\tau)$)-log(τ) diagram (or sigma-tau diagram) [15].

1.3 GPS Principles

The GPS satellite constellation consists of at least 24 satellites. The satellites are positioned in six Earth-centered nearly circular orbits with four satellites in each orbit. The dihedral angle between the orbit plane and equator is 55°. The six intersection points between the six satellite orbits and the equator are equally spaced at a 60° separation. The nominal orbital period of a GPS satellite is 11 h 58 min. Figure 1.4 presents the satellite orbits in a planar projection referenced to the very beginning of July 1, 1993 [17].

A GPS satellite transmits a signal with codes on the carrier wave. The code chipping rate is 1.023×10^6 chips/sec for civilian purpose. The carrier wave can be L1 (1575.42 MHz), L2 (1227.6 MHz), or L5 (1176.45 MHz). The time reference of the signal is the satellite clock. A GPS receiver generates a replica of the GPS signal based on the receiver clock. From the time difference between the received GPS signal and the replica GPS signal, we can tell the distance between the GPS satellite and the GPS receiver by simply multiplying by the speed of light [17].

There are two methods of getting the time difference. One method is to measure the time difference between the received code and the replica code. This is called pseudorange measurement or code measurement. The other method is to measure the phase difference between the received carrier wave and the replica carrier wave. This is called phase measurement. The difficulty of this method lies in the fact that we have no idea of the number of cycles between the satellite and the

receiver. We call the uncertainty of cycle number "integer ambiguity" or "phase ambiguity."

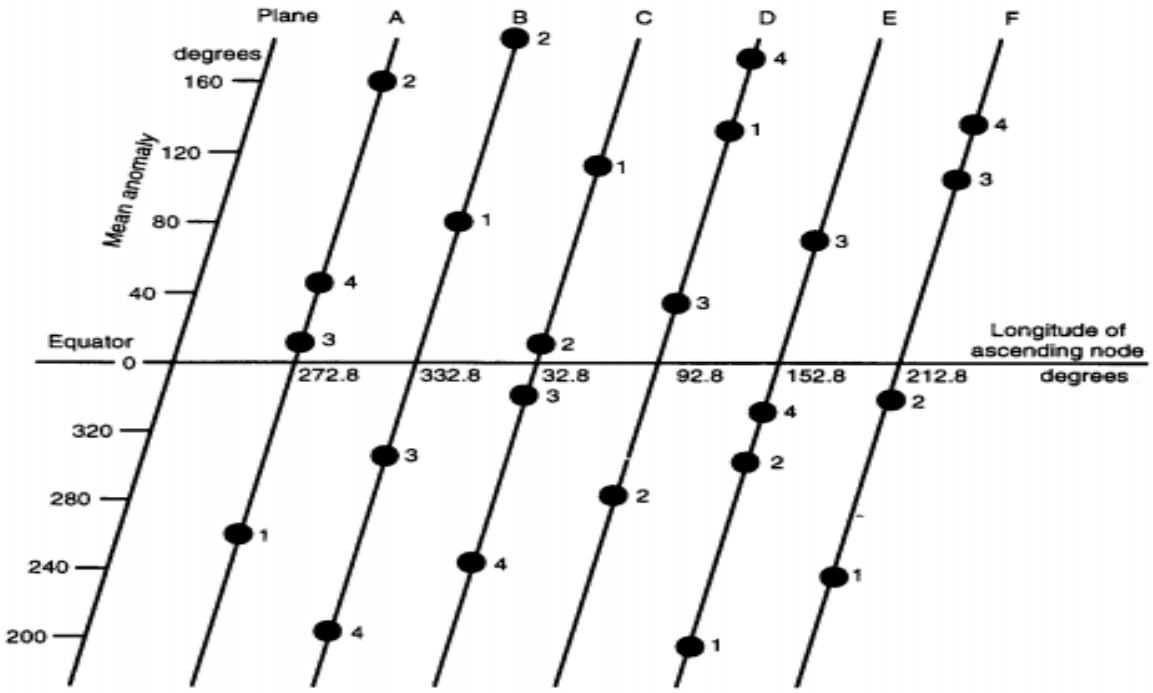

Figure 1.4. GPS constellation planar projection [17, Chapter 3].

Next, we discuss how to do positioning using GPS. In the Earth-centered Earth-fixed (ECEF) coordinate system, at GPS system time $t0$, a "j" GPS satellite at position $\vec{r}^{\,j} = (x^j, y^j, z^j)$, which has the satellite time of t^j (the satellite clock bias Δt^j is thus $t^j - t0$), transmits a signal with a carrier phase of φ^j. At epoch t_i, a GPS receiver "i" on the ground at position $\vec{r}_i = (x_i, y_i, z_i)$ (this position corresponds to t_i, instead of t^j) receives the signal. The replica carrier phase of the GPS receiver at this moment is φ_i. Then we have the following equations for code measurement and

phase measurement, respectively [18] (these two equations are called "observation equations"):

$$P_i^j \overset{\text{def}}{\equiv} c\left(t_i - t^j\right) = \left|\vec{r}^j - \vec{r}_i\right| + \Delta_{tropo} + \Delta_{ion} + c\Delta t_i - c\Delta t^j + \Delta MP_i^j + \Delta_{other} + \epsilon, \quad (1.5)$$

$$L_i^j \overset{\text{def}}{\equiv} c\frac{\varphi_i - \varphi^j}{2\pi f} = \left|\vec{r}^j - \vec{r}_i\right| + \Delta_{tropo} - \Delta_{ion} + c\Delta t_i - c\Delta t^j + \Delta MP_{i,\varphi}^j$$

$$+\Delta_{other,\varphi} + \epsilon_\varphi + \lambda N_i^j, \quad (1.6)$$

where Δt_i ($\Delta t_i \overset{\text{def}}{\equiv} t_i - t0$) is the receiver clock bias with respect to GPS system time; Δt^j is the satellite clock bias with respect to GPS system time; Δ_{tropo} and Δ_{ion} are the tropospheric delay and ionospheric delay, respectively; ΔMP_i^j is the multipath correction; Δ_{other} stands for other corrections such as earth tide and relativistic effect due to satellite eccentricity; ϵ is the noise term; N_i^j is the phase ambiguity. The multipath, Δ_{other}, and noise terms are different for code and phase measurements. ϵ_φ is much smaller than ϵ. Note that we use the subscript"φ" to distinguish code and phase.

We define the extra time delay $\Delta t_{D_i}^j$ as $(\Delta_{tropo} + \Delta_{ion} + \Delta MP_i^j + \Delta_{other})/c$, and the extra carrier phase time delay $\Delta t_{D_{i,\varphi}}^j$ as $(\Delta_{tropo} - \Delta_{ion} + \Delta MP_{i,\varphi}^j + \Delta_{other,\varphi})/c$. Now Eq. (1.5) and (1.6) become

$$P_i^j = \left|\vec{r}^j - \vec{r}_i\right| + c\Delta t_i - c\Delta t^j + c\Delta t_{D_i}^j + \epsilon, \quad (1.7)$$

$$L_i^j \overset{\text{def}}{\equiv} c\frac{\varphi_i - \varphi^j}{2\pi f} = \left|\vec{r}^j - \vec{r}_i\right| + c\Delta t_i - c\Delta t^j + c\Delta t_{D_{i,\varphi}}^j + \epsilon_\varphi + \lambda N_i^j. \quad (1.8)$$

Assuming that we already know $\{t^j, x^j, y^j, z^j\}$ and $\Delta t_{D_i}^j$, we need at least four satellites, i.e., four equations of Eq. (1.7), in order to determine the receiver's position x_i, y_i, z_i and clock bias Δt_i. Here, Eq. (1.8) does not help because it

introduces a new unknown N_i^j. If the receiver is static and there are code and phase measurements at many epochs, the smallest number of satellites number can go down to two [19, Chapter 6].

1.4 Mainstream Time Transfer Techniques

In this section, we review mainstream time transfer techniques. Regardless of which time transfer technique is applied, the most critical point in time transfer is always estimating or cancelling path delay accurately and precisely.

1.4.1 Transporting a Portable Clock

A straightforward way to do time transfer is to transport a clock from place A to place B. In theory, if the clock is transported so slowly that the time dilation effect is negligible and other relativistic effects are accounted for, we can achieve ideal time transfer. However, in practice, this method is not useful when the distance between the two places is long. First, because of the instability of a clock, the clock may become inaccurate after a long journey due to slow transportation. Second, if we use an airplane, we must consider the gravitational frequency shift, which requires the detailed trajectory information. Most importantly, it simply is not convenient to move a modern atomic clock, which is quite fragile. Even so, a small-size rubidium or cesium clock can be used if the transportation distance is small. In the OPERA neutrino speed measurement experiment, for example, the transport method was used to calibrate the fiber delay [14].

1.4.2 One-way Method

If the delay from the transmitter clock to the receiver can be determined by the use of ancillary data, we can use this method to transfer time [20]. Standalone GPS time transfer is an example of this method. By solving Eq. (1.7), we can get the receiver clock offset Δt_i with respect to GPS system time. Thus, we can synchronize a ground station to GPS system time if we correct the ground clock by $-\Delta t_i$. Here, the most important, but nontrivial challenge is how to obtain $\Delta t_{D_i^j}$ accurately with ancillary techniques. For example, the refractivity of the ionosphere contributes to about 65 ns extra time delay. With the measurement of the dispersion between signals at frequencies L1 and L2, this extra delay can be well determined. The total additional delay due to the refractivity of the troposphere is typically 6 ns in the zenith direction. For other non-zenith directions, some mathematical models (e.g., some mapping functions) are used to give a good estimation [17 Chapter 7, 20]. Besides, the uncertainty of satellite position and possible satellite clock offset can also affect the time transfer accuracy.

1.4.3 Two-way Method

The principle of two-way time transfer is shown in Figure 1.5. Epoch t_1 and Epoch t_4 are based on the timing system at Station A, while Epoch t_2 and Epoch t_3 are based on the timing system at Station B. We assume that the time difference between A and B is Δt_{AB}, which is what we are looking for.

First, Station A sends a timing signal to Station B at t_1. At t_2, B receives the signal. Then we have

$$t_2 = t_1 - \Delta t_{AB} + Delay(A \rightarrow B). \quad (1.9)$$

Second, Station B sends a timing signal to Station A at t_3 and A receives the signal at t_4. Now we have

$$t_4 = t_3 + \Delta t_{AB} + Delay(B \rightarrow A)\,. \quad (1.10)$$

If Delay(A→B) = Delay(B→A), then

$$\Delta t_{AB} = \frac{(t_4 - t_3) - (t_2 - t_1)}{2}. \quad (1.11)$$

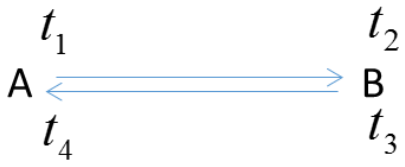

Figure 1.5. Illustration of two-way time transfer.

We see that the path symmetry in two-way time transfer is very critical. If the assumption " Delay(A→B) = Delay(B→A) " is not satisfied, we have to add corresponding corrections, which may be difficult [19].

Two-way satellite time and frequency transfer (TWSTFT) is a good example of this method, which is sometimes used to compare the clocks and time scales of different timing laboratories. First, a signal that is synchronized to the 1 Hz ticks of the local clock is transmitted to a geostationary satellite. The satellite, as a relay station, continues transmitting the signal to a remote station. After this, the remote station transmits another signal through the same path back to the local station. The timing accuracy is typically smaller than 1 ns [20–24]. The U. S. Naval

Observatory (USNO) uses TWSTFT to transfer time to the USNO Alternate Master Clock in Colorado to support GPS control [21].

1.4.4 Common View Method

This method was proposed at the beginning of 1980s [24] and has dominated the time transfer area for more than 20 years. To evaluate the common view method, we begin with Eq. (1.7). We encounter the problem of estimating $\Delta t_{D_i}^{\ j}$ as mentioned in Section 1.4.2. If the stations A and B (Figure 1.6(a)) are very close (i.e., within 1000 km), the ionospheric and tropospheric path delays are almost the same for A and B, no matter how big they are. If A and B observe the same satellite simultaneously, the $\Delta t_{D_i}^{\ j}$ term can be cancelled out so that we can compare clock A and clock B very accurately. Additionally, the uncertainty of satellite position and satellite clock offset can also be eliminated [25].

The common view method does not work very well when the baseline between A and B is greater than 1000 km because $\Delta t_{D_i}^{\ j}$ cannot be cancelled since the ionospheric and tropospheric path delays are no longer the same for A and B. At this time, the uncertainty of time transfer is usually greater than 5 ns. A detailed error budget study can be reached in [24, 26].

All-in-view method developed from the common view method basically implements a common time reference for all satellites' clocks. In the case where the baseline is greater than 1000 km, the common-view principle could be realized with respect to this common time reference even for stations that received time signals from different physical satellites [20]. Figure 1.6(b) illustrates this idea. Thus the

all-in-view method can compensate for the disadvantage of the common view method for long-baseline time transfer. A comparison between common view and all-in-view shows that the two have comparable performance (deviation is ~0.6 ns) if the baseline is shorter than 1000 km. When the distance is 17,000 km, common view has a 1.4 ns uncertainty, while all-in-view is still at the 0.6 ns level [26].

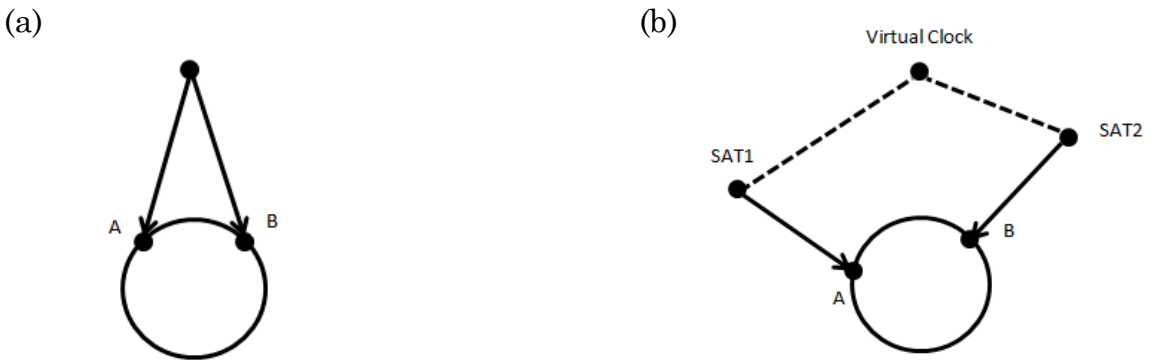

Figure 1.6. Common-view method (a) and all-in-view method (b).

1.4.5 Carrier Phase Method

As we mentioned in Section 1.3, the chipping rate of code much lower than the carrier wave frequency, and the code measurement noise, ϵ, is much bigger than the phase measurement noise, ϵ_φ. Thus the code measurement P_i^j is much less precise than the phase measurement L_i^j. We know that the code/phase measurement precision finally affects the time transfer precision. If we can use Eq. (1.8), instead of Eq. (1.7) as in the common view method, to do time transfer, we can potentially improve the precision by the two orders of magnitude. This is named carrier phase method [27–28]. The critical issue of carrier phase method is how to accurately estimate the phase ambiguity N_i^j. Without an accurate estimation of phase

ambiguities for two consecutive batches of GPS data, we get a discontinuity in the estimation of the receiver time and position. This phenomenon of man-made discontinuity is called boundary discontinuity. Although the precision of carrier phase time transfer has reached around 50 ps, its accuracy is only approximately 0.5 ns because of boundary discontinuity. This problem has been a big obstacle in the precision time transfer for more than 10 years [18, 29–33]. Since there is more to learn, we will discuss more details about this time transfer technique in the next section.

1.5 Details of GPS Carrier Phase Time Transfer

1.5.1 Theoretical Study of GPS Carrier Phase Time Transfer

The estimation of phase ambiguity is the central challenge of carrier phase time transfer. The difficulty of estimating accurate phase ambiguity comes from the delay and noise terms in Eq. (1.8). GPS satellite clock noise, satellite position uncertainty, ionospheric and tropospheric noise, multipath, receiver clock offset, and receiver circuit noise all affect the phase ambiguity estimation.

Double difference $L_{ik}^{jl} \stackrel{\text{def}}{=} \left(L_i^j - L_k^j\right) - \left(L_i^l - L_k^l\right)$ can get rid of the $c\Delta t_i$, $c\Delta t^j$ and $c\Delta t_{D}{}_{i,\varphi}^{j}$ terms and also the corresponding noises in Eq. (1.8), if the two receivers, "i" and "k", are within tens of kilometers of each other so that the tropospheric delay and ionospheric delay are almost the same. It is easy to get

$$L_{ik}^{jl} = r_{ik}^{jl} + \epsilon_{ik,\varphi}^{jl} + \lambda N_{ik}^{jl}, \tag{1.12}$$

where $r_{ik}^{jl} = (r_i^j - r_k^j) - (r_i^l - r_k^l) = (\hat{\boldsymbol{e}}_k^j - \hat{\boldsymbol{e}}_k^l) \cdot (\vec{r}_i - \vec{r}_k)$. Here, $r_i^j \stackrel{\text{def}}{=} |\vec{r}^j - \vec{r}_i|$, and $\hat{\boldsymbol{e}}_k^j$ is the unit vector from receiver "k" to satellite "j". With M satellites in view, there are $M-1$ independent double differences equations of Eq. (1.12), and $M-1$ unknown N_{ik}^{jl} and unknown $(\vec{r}_i - \vec{r}_k)$. Thus we have $M-1$ equations with $M+2$ unknowns, which won't allow us to solve for the unknowns. However, with more epochs of observation, we can solve the equations. Since N_{ik}^{jl} is a constant if the receivers are still tracking the satellites, the number of equations exceeds the number of unknown variables. Thus, we are able to solve N_{ik}^{jl} and $(\vec{r}_i - \vec{r}_k)$ [34].

Using this analysis, we can achieve precise relative positioning [i.e., $(\vec{r}_i - \vec{r}_k)$] by using the double difference technique. However, in the field of time transfer, we must know the absolute position of the GPS receiver. Any offset in the absolute position could lead to a slope in time transfer [18]. That means, the double difference technique is won't work well for carrier phase time transfer.

As mentioned at the beginning of this section, the phase ambiguity is related to noise and delays. If we can provide precise information about the terms on the right side of Eq. (1.8), such as the satellite clock offset and position, as well as the ionospheric and tropospheric delays, we can achieve an accurate estimation of phase ambiguity after many epochs of convergence. We can obtain the satellite clock and position information from the International GNSS Service (IGS) website. To eliminate the ionospheric delay, we can use an ionosphere-free combination of phase measurements to form a new phase ambiguity ${N_{IF}}_i^j$, which is no longer an integer. Now, ${N_{IF}}_i^j$ is more susceptible to noise than N_i^j which can withstand the noise of less

than half a cycle because of its integer property). Since tropospheric delay changes hour after hour, we can also introduce a new unknown variable "tropospheric zenith delay" (TZD). By solving for TZD, we get a better estimation of the tropospheric delay. We also need to use models for earth tides, the relativistic effect due to satellite eccentricity, etc. Now we know everything on the right side of Eq. (1.8) except those unknown variables that we want to solve for (e. g., receiver position and clock, phase ambiguity ${N_{IF}}_i^j$). Ideally, Eq. (1.8) itself is sufficient for doing time transfer.

However, there is a serious problem. Notice that $c\Delta t_i$ and $\lambda {N_{IF}}_i^j$ (or λN_i^j) in Eq. (1.8) are inseparable, no matter how many epochs of observation we have. A one meter increase in $c\Delta t_i$ can be compensated by a one meter decrease in $\lambda {N_{IF}}_i^j$. So Eq. (1.7) must be used to resolve this inseparability. Thus, code measurement noise comes into the uncertainty of phase ambiguity via the estimation of Δt_i.

Now we study the behavior of Δt_i.

First, we must use code measurements to get an unbiased Δt_i for the initial epoch. However, because of the big noise in code measurements, even though we may do averaging over many epochs of code measurements, Δt_i still has an uncertainty of a few hundred picoseconds. We use the random variable X to represent this uncertainty.

Second, at the initial epoch, because of the noise term ϵ_φ in Eq. (1.8), we have a biased estimation of ${N_{IF}}_i^j$. At later epochs, since the average of ϵ_φ is zero and ${N_{IF}}_i^j$ is kept the same as the initial estimation, Δt_i has an average bias of Y. For example,

at the initial epoch, ϵ_φ happens to be +1 cm. And Δt_i has already been estimated by code measurements, so it should not change at this epoch no matter what ϵ_φ is. Thus, $\lambda N_{IF}{}_i^j$ must have a bias of −1 cm in order to satisfy Eq. (1.8). In the later epochs, ϵ_φ has an average value of 0 cm, and $\lambda N_{IF}{}_i^j$ is kept a constant (i.e., it has a bias of −1 cm). So $c\Delta t_i$ must have an average bias of +1 cm. We can clearly see from this example that $Y = \epsilon_\varphi(initial\ epoch)/c$. The random variable X+Y describes the distribution of total bias in Δt_i. The boundary discontinuity is the time jump between two batches of data. For one batch, there is a total bias of X_1+Y_1 in Δt_i. For the other batch, the total bias is X_2+Y_2. Since X_1, Y_1, X_2, and Y_2 are typically independent of each other, the boundary discontinuity $BD = (X_2 + Y_2) - (X_1 + Y_1)$ has a standard deviation of $\sqrt{2}\sigma(X_1 + Y_1)$. This tells us that boundary discontinuity is related to both the code and phase noise.

Third, the relative change of Δt_i at all epochs within one data batch is determined by both the receiver clock noise and ϵ_φ. Thus as phase noise ϵ_φ increases, Δt_i becomes noisier from epoch to epoch.

In summary, although the implementation of carrier phase time transfer varies and may be somehow different than the theoretical analysis here, we know that the boundary discontinuity comes from both the code and phase noise. The time transfer noise within a single data batch is determined by the phase noise.

1.5.2 Implementation of GPS Carrier Phase Time Transfer

There are two methods of implementing carrier phase time transfer, the network method and the precise point positioning (PPP) method.

The network method assumes that all the parameters (e.g., Δt_i, Δt^j, $\vec{r}^j$) on the right side of Eq. (1.6) (or Eq. (1.8)) as unknowns and uses the GPS data from all receivers to solve for these parameters. If the receiver number R is much greater than the GPS satellite number, the computation burden is proportional to R^3 [35].

In contrast, the precise point positioning (PPP) method first uses a subset of S receivers to estimate the satellite parameters, earth orientation, and S sets of receiver parameters. Then GPS data from each of the remaining R-S receivers are analyzed, one receiver at a time. The computation burden is now proportional to R, instead of R^3. The PPP method provides results comparable in quality to the result of the network method [35]. This thesis work used the PPP method, if not specifically mentioned.

1.6 Thesis Outline

Boundary discontinuity is a major obstacle to achieving continuous GPS carrier phase time transfer. In practice, we can divide the boundary discontinuity into two categories.

The first category of boundary discontinuity is "data-batch boundary discontinuity." We must estimate the phase ambiguity for each data batch. An inaccuracy of phase ambiguity estimation almost always occurs because of code and

phase noise. Thus, there is a discontinuity of time transfer between two consecutive data batches. Typically, the length of a data batch is one day. In this case, we call it the “day boundary discontinuity” (day-BD).

The second category of boundary discontinuity is “boundary discontinuity due to GPS measurements anomaly” (for short, anomaly-BD). Within one data batch, there may have some missing data or bad data caused by a GPS receiver anomaly. In this case, the PPP software has to re-estimate the phase ambiguity. Thus, there can be a discontinuity between two arcs of good data.

We can see that both categories of boundary discontinuity come from the inaccuracy of phase ambiguity estimation. However, practically, two different strategies are used to eliminate the two categories of boundary discontinuity.

Chapters 2–4 focus on the day-BD. Chapter 2 describes the characteristics of the day-BD. The distribution of the day-BD is Gaussian, and different timing laboratories have different boundary discontinuities. The carrier-phase time transfer results of NRCan PPP, Atomium PPP, and Novatel GrafNav PPP software packages are also compared in this chapter. We can see that the NRCan PPP and Atomium PPP provide better performance than the Novatel GrafNav PPP.

Chapter 3 studies the origin of the day-BD. For a geodetic GPS receiver, it is the noise in the pseudorange that mainly contributes to the boundary discontinuity. By using the 30-sec IGS clock data instead of the 5-min IGS clock data, we are able to reduce the boundary discontinuity by 10–30%. Averaging over several receivers at the same station also leads to a 15–20% decrease of the boundary discontinuity.

We find that the network method of carrier-phase time transfer shows a smaller boundary discontinuity than the PPP method. The use of different tropospheric mapping functions provides little improvement to the boundary discontinuity. We need to mention that most conclusions in Chapter 2 and Chapter 3 should also work for the second category of boundary discontinuity (i.e., anomaly-BD).

Chapter 4, as the most important section of this thesis, designs a new algorithm (i.e., RINEX-Shift algorithm) to eliminate the day-BD. A series of tests show that the RINEX-Shift algorithm provides the best carrier-phase time transfer result.

Chapter 5 focuses on the anomaly-BD. A few minutes of GPS data anomaly can lead to a discontinuity of more than 200 ps in carrier-phase time transfer. In particular, if there is only a short term of valid data (e.g., less than 1 hour) before or after the anomaly, carrier-phase time transfer does not have enough time to converge. Consequently, the time-transfer result for this short term is seriously damaged. A straightforward strategy for dealing with this category of boundary discontinuity is to perform curve fitting for the anomaly. We find out that this strategy works very well for at least 20 min of measurement anomalies.

Chapter 6 concludes this thesis and discusses some future work in this field.

Chapter 2

Characteristics of Day Boundary Discontinuity[1]

2.1 Introduction

As stated in Section 1.5.1, a boundary discontinuity comes from the uncertainty of the estimation of phase ambiguities. Figure 2.1 shows an example of the boundary discontinuity. Here, we compare the time difference between the NIST time and the International GNSS Service (IGS) time scale by GPS carrier-phase time transfer. The NIST time [i.e., UTC(NIST)] is the standard time in the United States, provided by the National Institute of Standard and Technology (NIST), Boulder, USA. Note in Figure 2.1 that there are some constant cable delays that shift the time difference values away from 0 ns. Clearly, within a single day, the curve in Figure 2.1 is continuous. However, between two consecutive days, there is often a big boundary discontinuity. For example, the magnitude of the jump between Modified Julian Day (MJD) 55601 and 55602 is greater than 300 ps (as shown by the red oval in Figure 2.1).

[1] The results of this chapter are mainly based on [18].

Some people may think that a jump of a few hundred picoseconds, as shown in Figure 2.1, is too small and thus not a problem. However, in the field of time transfer for high-precision clocks, such as a Cesium (Cs) fountain and a Hydrogen-Maser (H-Maser), a few hundred picoseconds do matter. We will confirm this point by comparing Figure 2.2 and Figure 2.3 in the next paragraph.

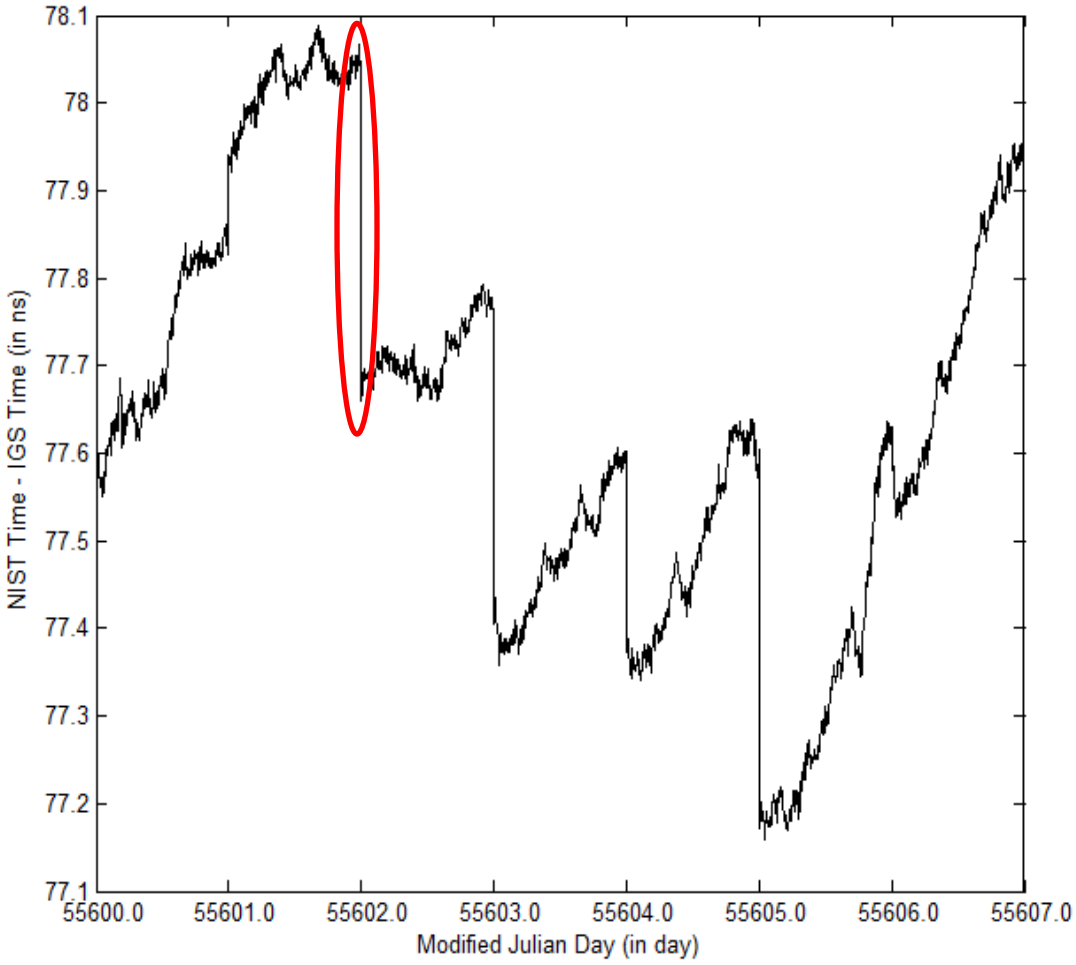

Figure 2.1. Illustration of the boundary discontinuity.

Figure 2.2 shows the frequency stability of the NIST F1 Cs fountain with respect to H-Maser (blue curve) and AT1E (black curve) [36]. The red curve is the

theoretical curve. We can see that for an averaging time of 1 day (i.e., 86400 s), the fractional frequency of the Cs fountain is approximately 1×10^{-15} (i.e., the uncertainty of the Cs fountain in one day is 86.4 ps.). For an averaging time of 10 days (i.e., 864000 s), the fractional frequency is approximately 3×10^{-16} (i.e., 250 ps per 10 days). In contrast, Figure 2.3 shows the frequency stability of the GPS carrier-phase time transfer result with the boundary discontinuities not removed, with respect to the Two Way Satellite Time and Frequency Transfer (TWSTFT) [37]. For an averaging time of 1 day, the fractional frequency of the GPS carrier-phase time transfer is approximately 7×10^{-15} (i.e., 604.8 ps per day), which is seven times as big as the Cs-fountain clock noise (i.e., 1×10^{-15}). This result means that for a time comparison between two long-distance Cs fountains, the time transfer noise, rather than the clock noise itself, dominates in the total uncertainty of the time comparison for an averaging time of 1 day. For an averaging time of 10 days, the fractional frequency of the GPS carrier-phase time transfer is about 1×10^{-15} (i.e., 864.0 ps per 10 days), which is still much larger than the fractional frequency of the Cs-fountain clock noise (i.e., 3×10^{-16}). In other words, the time transfer noise is still a major contributor to a long-distance time-comparison uncertainty even after 10 days. From the above, we clearly see than a few hundred picoseconds do matter in the time transfer of a high-precision clock. Without the boundary discontinuity removed, we cannot observe the actual clock behavior even though we have done 10 days of time comparison by the GPS carrier phase time transfer technique!

If we can find some ways to reduce or remove the boundary discontinuity, we can possibly decrease the GPS carrier-phase time transfer noise and thus start to observe the actual clock behavior after a shorter term of observations, rather than more than 10 days. An earlier observation of long-distance clock behavior has many advantages. For example, it allows us to know about a long-distance clock error timely. We can also more frequently steer a local clock to a long-distance clock, resulting in a better synchronization. In addition, it accelerates the formation of UTC and the realization of UTC at a local station.

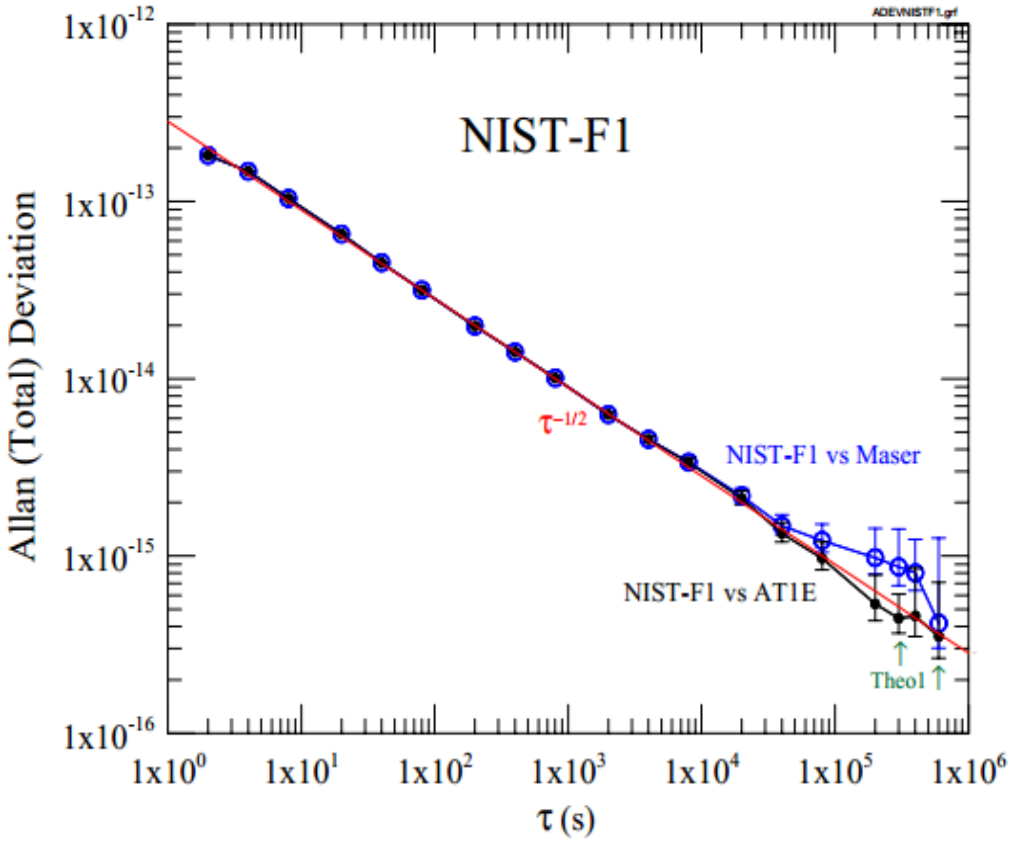

Figure 2.2. The frequency stability of the NIST F1 Cs fountain clock [36]. Note, AT1E is a time scale generated from the combined output of a cluster of hydrogen masers. The cluster of H-Maser noise in both short-term and long-term should be quite smaller than that of a single fountain. Thus the blue and black curves decribe the frequencyh stability of a single Cesium fountain clock.

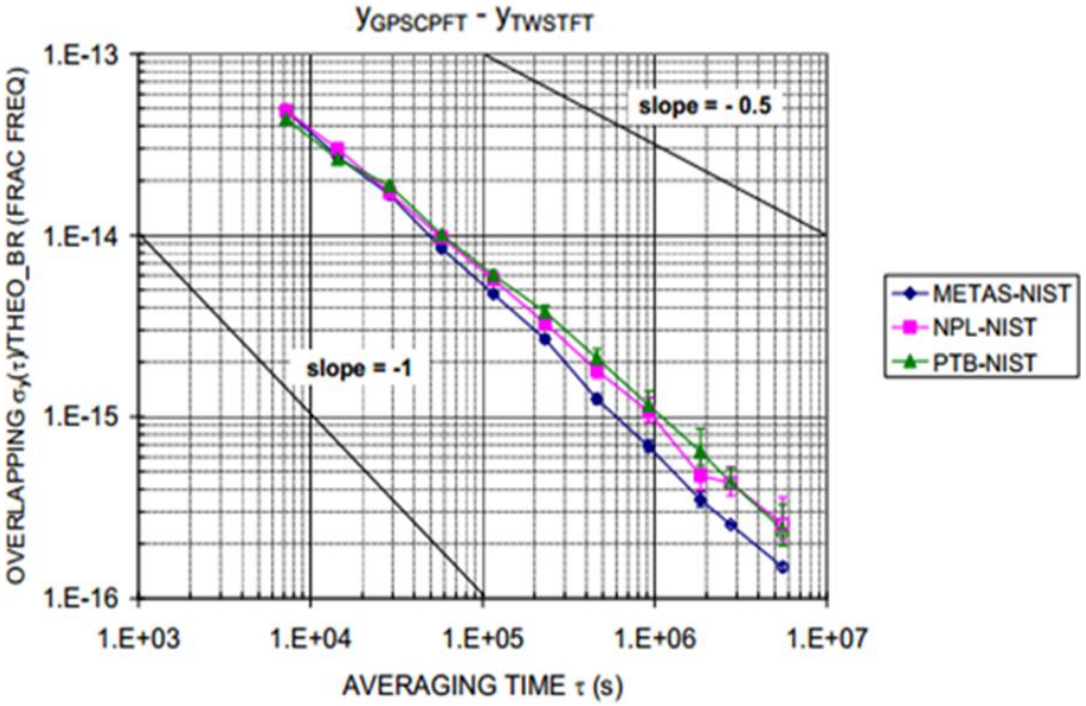

Figure 2.3. Frequency stability of the GPS carrier phase time transfer between two stations (METAS and NIST (blue), NPL and NIST (magenta), PTB and NIST (green)), with the boundary discontinuities not removed [37].

The above analysis shows the great importance of studying the problem of boundary discontinuity. In this chapter, we focus on the characteristics of boundary discontinuity. Section 2.2 introduces the NRCan PPP software package that is used to implement the GPS carrier-phase time transfer in this thesis. Section 2.3 discusses the methods of extracting boundary discontinuities. Sections 2.4–2.5 are the core parts of this chapter. They study the statistics of boundary discontinuity, e.g., the mean and the standard deviation (STD). Section 2.4 discusses the one-day boundary discontinuity ("one-day boundary discontinuity" is also called "day boundary discontinuity") and Section 2.5 discusses the multi-day boundary discontinuity. Finally, Section 2.6 compares NRCan PPP with other PPPs.

2.2 GPS Data Processing

The NRCan PPP [38–39] is used to do the GPS carrier-phase time transfer in this thesis. Other PPP programs are also run to compare them with the NRCan PPP in Section 2.6.

The inputs of the NRCan PPP are the IGS sp3 file, the IGS clk file, the RINEX file, and a few correction files. Here, the IGS sp3 file provides the coordinates of all the GPS satellites every 15 min [40]. The IGS clk file provides the clock offsets of all the GPS satellites and many ground stations every 5 min [41]. The IGS sp3 file and the IGS clk file together are called IGS products. The IGS products are computed by the network method, as mentioned in Section 1.5.2. There are three types of IGS products: IGS final (IGS has the highest quality, but about 2 weeks of latency), IGS rapid (IGR has a quality nearly comparable to that of the IGS final products, and about 17 hours of latency), and IGS ultra-rapid (IGU aims for real-time and near real-time use and is not discussed in this thesis). Reference [18] shows that the boundary discontinuity behavior does not change regardless of whether the IGS final products or the IGS rapid products are used, because the qualities of both products are almost the same. Thus, both IGS final products and IGS rapid products are used in our study of boundary discontinuity reported in this thesis. The RINEX file [42] is recorded by a local GPS receiver typically every 30 seconds. It has the code and phase measurements on both L1 and L2 for all visible GPS satellites. The RINEX file may also contain Doppler shifts and GPS signal strength. But these two parameters are not used in the NRCan PPP software. The correction

files have information about the antenna correction, P1–C1 code biases, ocean tide, tropospheric mapping function, etc.

The default settings of NRCan PPP are as follows: "USER DYNAMICS" is set to "STATIC" because all receivers used in this thesis are in static mode; we use the IGS final or rapid sp3 and clk products; the software solves for both the station position and the clock bias; the cutoff elevation is set to 10 degrees; the data-arc (or data batch) is 1 day; the weight of the code measurement is 1, while the weight of the phase measurement is 100.

Generally speaking, NRCan PPP solves the observation equations [i.e., Eq. (1.5)–(1.6)]. To be more specific, NRCan PPP first linearizes the observation equations around the a-priori parameters and then solves the equations by the least squares method with a-priori weighted constraints. The adjustment procedure of the a-priori weighted constraints is effectively a sequential filter that adapts to varying user dynamics (for details, see [38–39]). After a couple of hours, the PPP solutions converge to the level of a few centimeters. At the end of the data-arc, the NRCan PPP reverses and goes backward until the beginning of the data-arc. We extract the clock bias from the backward data, because the solutions converge better in the backward mode. The clock bias is very often not continuous between two consecutive days. This is the boundary discontinuity. Next section will discuss how to compute the jump value of the boundary discontinuity.

2.3 Methods of Extracting Boundary Discontinuity

We use two methods to compute the boundary discontinuity [18, 28]. The first method is called the "raw method" (Figure 2.4). This method computes the time difference between the average of 0:00 and 0:05 for each day (see the bottom black dot in Figure 2.4) and the average of 23:50 and 23:55 for the previous day (see the top black dot in Figure 2.4), and also corrects for the slope (the linear fit lines in Figure 2.4). The second method is called the "overlapping method" (Figure 2.5). This method first runs PPP for two consecutive days independently. Second, it runs PPP for the combined two days. Finally, it extracts the time difference between the first day and the combined two days $\Delta_{1\to X}$ and the difference between the combined two days and the second day $\Delta_{X\to 2}$. Then $\Delta_{1\to 2}= \Delta_{1\to X} + \Delta_{X\to 2}$ gives the jump value (i.e., the boundary discontinuity) between the two days.

These two discontinuity-extraction methods give us almost the same jump values. Statistically, the STD of the boundary discontinuity extracted by the overlapping method is slightly smaller (typically, ~15 ps smaller) than that extracted by the raw method, because the overlapping method removes the short term (i.e., 5 min) noise between the end of first day and the beginning of the second day by subtracting the 1-day data-arc PPP result from the 2-day data-arc PPP result. For the sake of consistency, we use the overlapping method except when mentioned specifically.

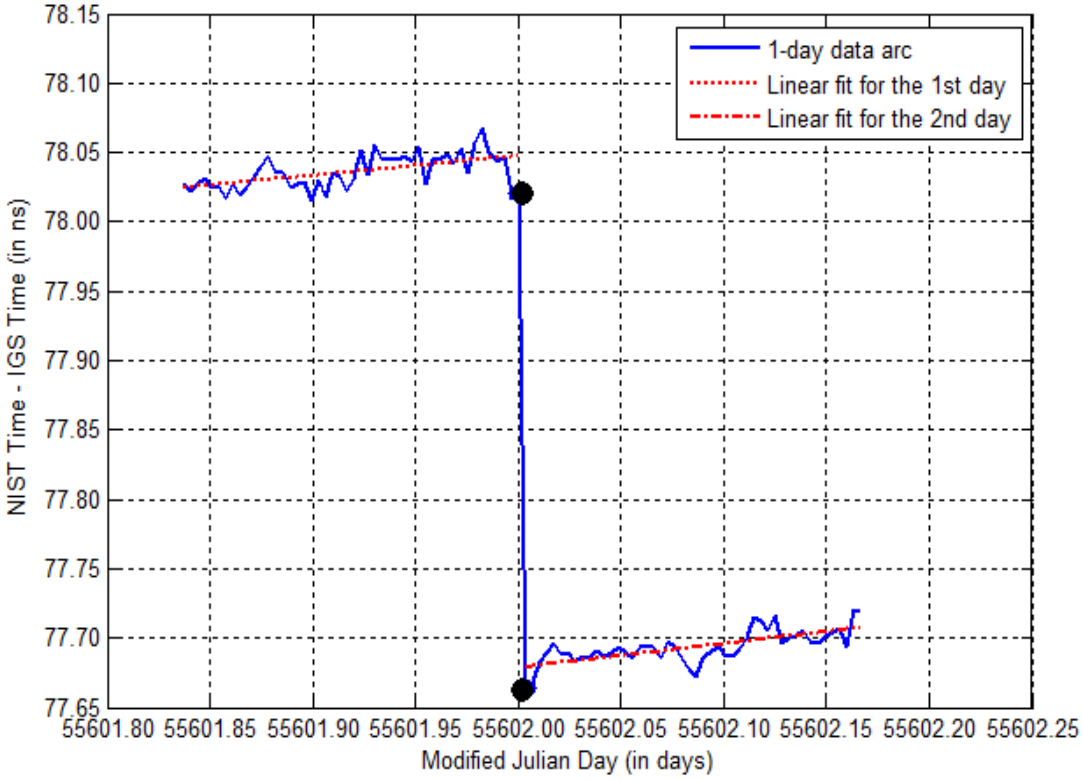

Figure 2.4 Illustration of Raw Method.

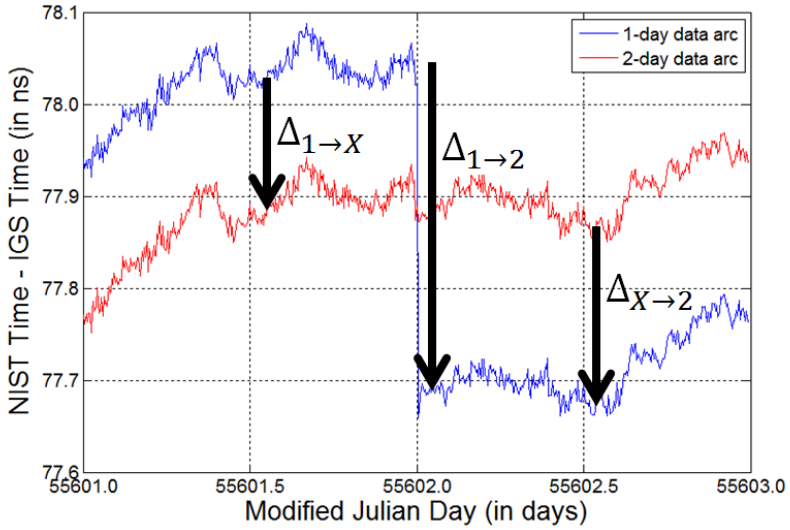

Figure 2.5. Illustration of Overlapping Method. $\Delta_{1\to X}$ is the average time difference between the first day and the combined two days from 15:00 to 21:00. $\Delta_{X\to 2}$ is the average time difference between the second day and the combined two days from 3:00 to 9:00. $\Delta_{1\to 2} = \Delta_{1\to X} + \Delta_{X\to 2}$, where $\Delta_{1\to 2}$ is the jump value estimated by the Overlapping Method.

2.4 Statistics of Day Boundary Discontinuity

Since the day boundary discontinuity varies day after day, we can hardly study its behavior based on the analysis of just a few days of GPS data. Thus, we consider the day boundary discontinuity as a random variable and study its statistical behavior, i.e., the mean value and the STD, based on more than 100 days of GPS data.

Here, we run NRCan PPP (1-day data-arc) with the IGR products as the input, for *NIST* [a GPS receiver at the National Institute of Standards and Technology (NIST), Boulder, USA], *PTBB* [a GPS receiver at the Physikalisch-Technische Bundesanstalt (PTB), Germany], and *USN3* [a GPS receiver at the United States Naval Observatory (USNO), DC, USA], during MJD 55600–55750. As an example, Figure 2.6 shows the NRCan PPP result for *NIST*. Between MJD 55667 and MJD 55668, there is an adjustment in the IGR time scale that leads to approximately a −7 ns jump. This jump is removed in our study. We extract the day boundary discontinuities by the overlapping method as discussed in Section 2.3. Figure 2.7 (a) shows the histogram of the jump values for *NIST*. Also, Figure 2.7 (b) and (c) are the histograms of the jump values for *PTBB* and *USN3*, respectively. We can clearly see from Figure 2.7 that the distribution of the boundary discontinuity is almost Gaussian [see the Appendix at the end of this chapter (i.e., Section 2.7), for the Gaussian-distribution test]. The mean values are −146.7 ps, 45.4 ps, and 21.4 ps, and the STDs are 236.7 ps, 138.5 ps, and 106.7 ps. Clearly, *USN3* provides the smallest boundary-discontinuity jump. In contrast, the mean value of *NIST* is far

from 0 ps, which makes the popular concatenating algorithm quite difficult to implement [43].

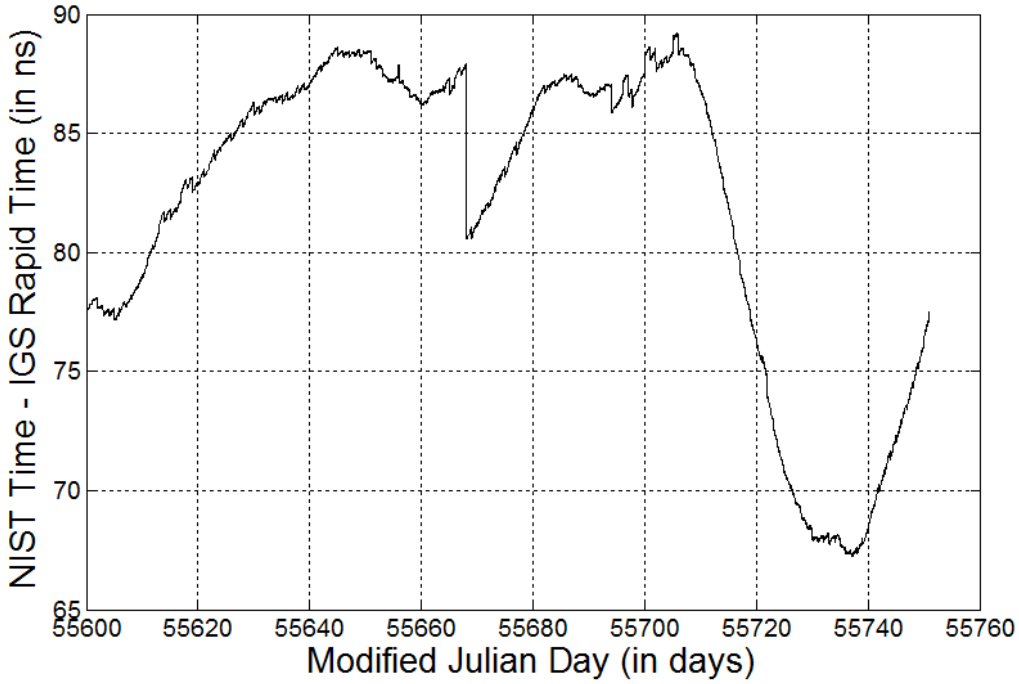

Figure 2.6. NRCan PPP result for the *NIST* time with respect to the IGR time.

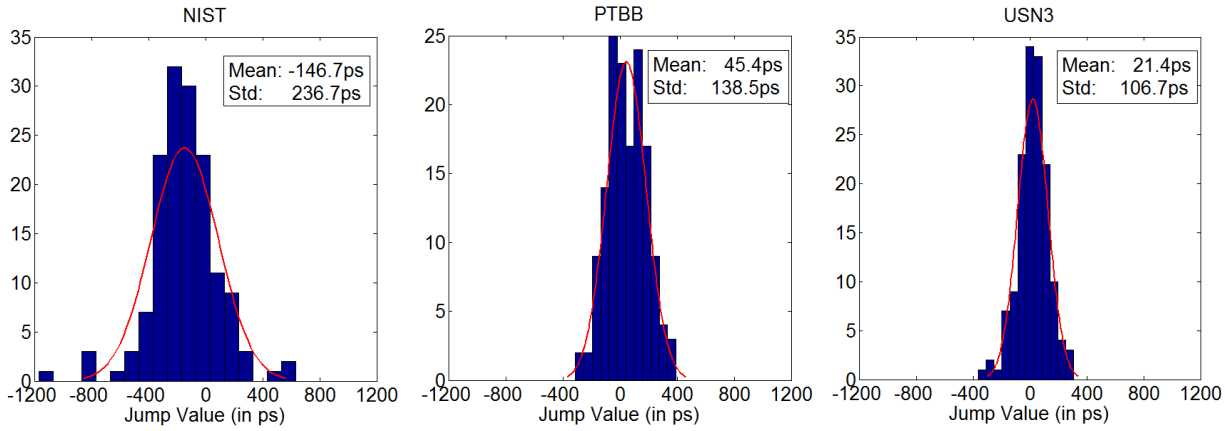

(a) (b) (c)

Figure 2.7. Histograms of jumps of *NIST*, *PTBB*, *USN3* for MJD 55600–55750, with respect to the IGS rapid (IGR) time.

2.5 Boundary Discontinuity of Different Data-arcs

Section 2.4 presented the statistics of the discontinuities for a 1-day data-arc. To avoid the problem of the day boundary discontinuity in the PPP processing, many organizations, including the Bureau International des Poids et Mesures (BIPM) [44], have started to use a longer data-arc (e.g., 35 days) in the PPP processing. In this way, a day boundary discontinuity is converted to a multi-day data-arc boundary discontinuity. However, we do not know how the boundary discontinuity changes as the data-arc increases from 1 day to a few days. Thus, we have no idea about how well the multi-day PPP result represents the "true" result.

2.5.1 Results

To clarify these unknowns, we run PPP for *USN3* for MJD 55500–55900. The length of a data-arc increases from 1 day to 4 days. We can see from the results (blue curves in Figure 2.8 (1a)–(1b)) that both the mean value and the STD of the boundary discontinuity increase as the length of a data-arc increases. Consequently, when a longer data-arc is used, we should expect a greater boundary discontinuity. Thus, a longer data-arc PPP processing does result in some time periods of the PPP result deviating more from the true result than a 1-day data-arc PPP processing.

We also run PPP for *PTBB*, *NIST*, and *AMC2* (a GPS receiver in Colorado Springs, USA) for MJD 55500–55900 (see the blue curves in Figure 2.8 (2a)-(4b)). Clearly, the mean value of the boundary discontinuity is almost proportional to the data-arc length. Although the STD is not always monotonically increasing, the

tendency of STD does increase as the data-arc length increases. This result further confirms the conclusion that the longer the data-arc is, the greater the boundary discontinuity becomes.

2.5.2 Theoretical Analysis

This section explains the results in Section 2.5.1 theoretically.

We consider the time result of PPP as $X + \Delta$, where X stands for the "true" time solution, and Δ is the shift due to the uncertainty of the phase ambiguity. Thus, the day boundary discontinuity obviously satisfies

$$BD^1_{M,M+1} = \Delta^1_{M+1,M+1} - \Delta^1_{M,M}, \tag{2.1}$$

where the superscript represents the length of a data-arc; the subscript (k, k+1) for BD represents the jump between the k^{th} day and the (k+1)$^{\text{th}}$ day; and the subscript (k, n) for Δ represents the timing shift for the PPP result between the k^{th} day and the n^{th} day.

We know from Section 1.5.1 that Δ depends on both the average of the code noise of the whole data-arc and the phase noise at the first epoch. Typically, the phase noise is at the level of approximately 10–20 ps, which is much smaller than the actual time shift Δ (typically, greater than 100 ps). Thus, Δ mainly depends on the average of the whole data-arc code noise. If the data-arc is increased to M days, then we have

$$\Delta^M_{1,M} = (\Delta^1_{1,1} + \Delta^1_{2,2} + \cdots + \Delta^1_{M,M})/M. \tag{2.2}$$

We can clearly see from the example in Figure 2.9 that the 4-day data-arc PPP result (the red curve) is almost an average of the four 1-day data-arc PPP results. This result verifies Eq. (2.2).

1(a)

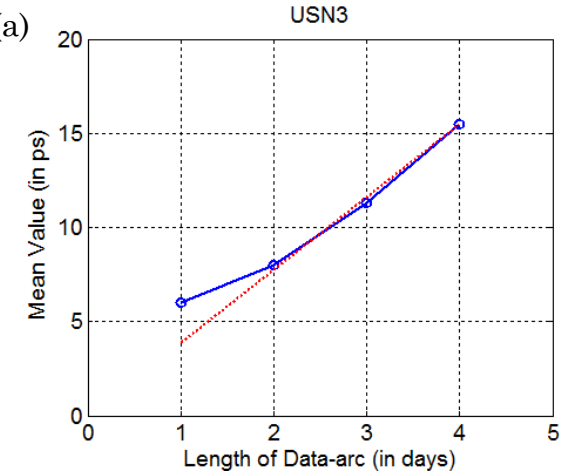

1(b)

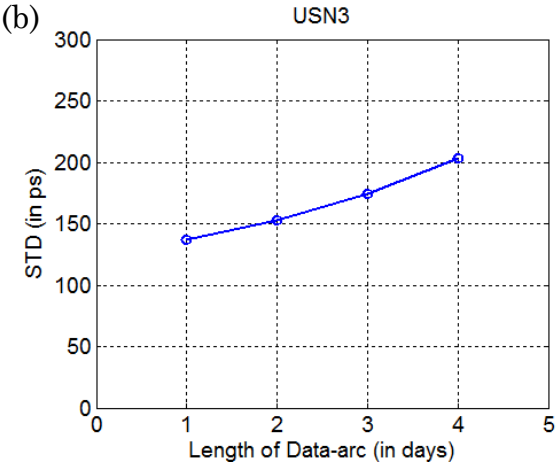

2(a)

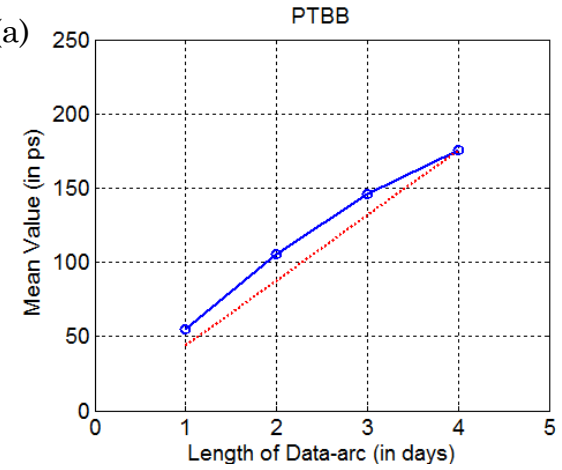

2(b)

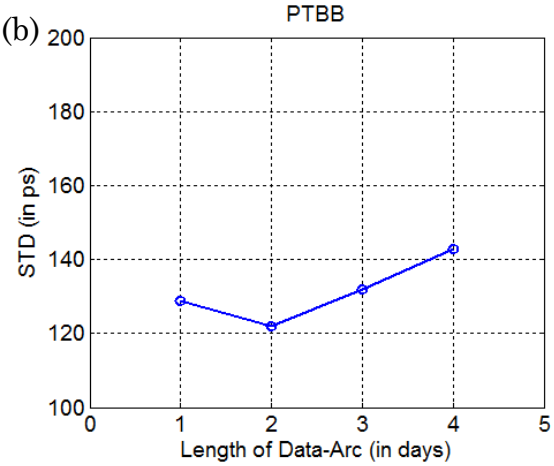

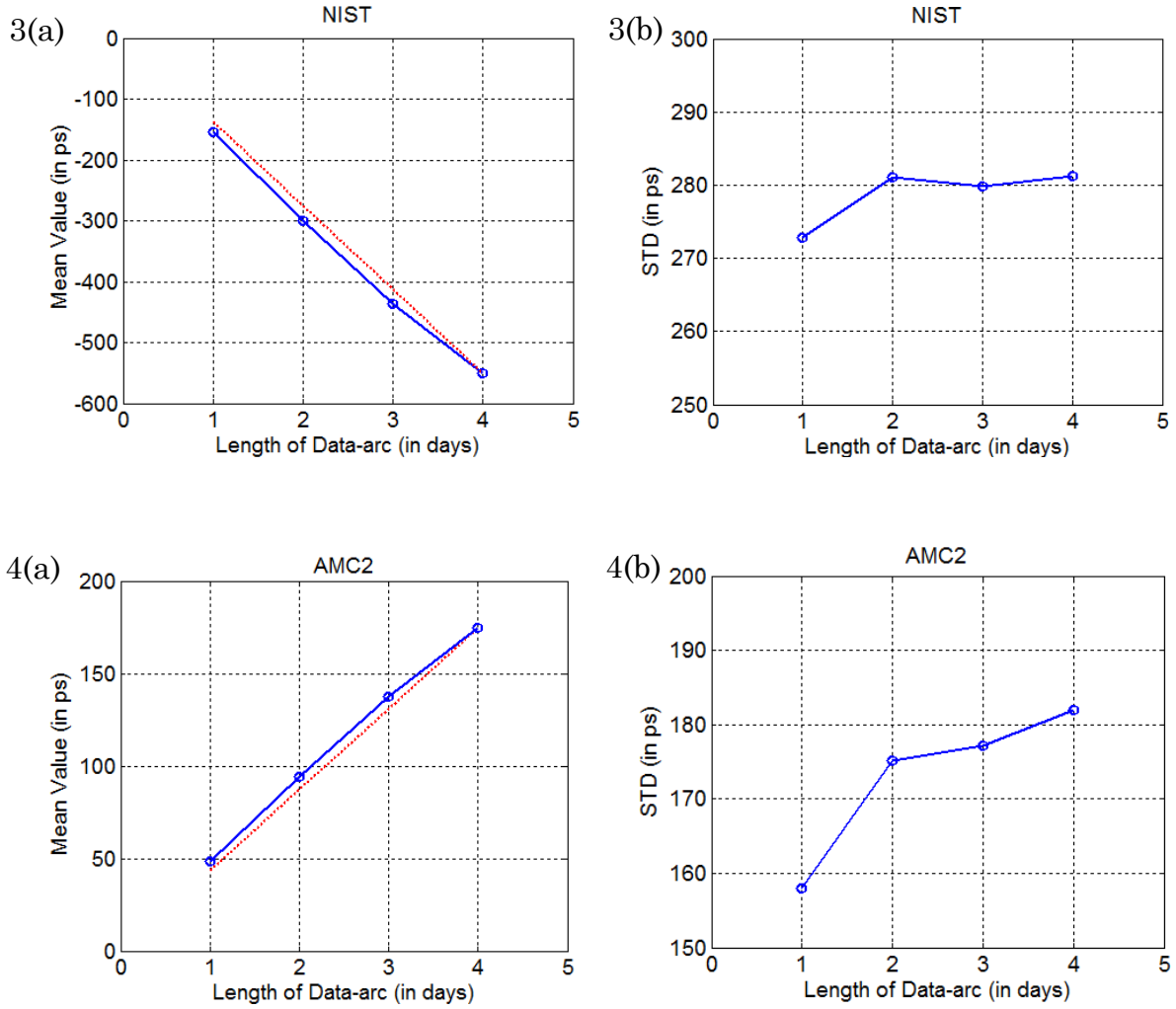

Figure 2.8. Statistics of the boundary discontinuity of different data-arcs for *USN3* [1(a) and 1(b)], *PTBB* [2(a) and 2(b)], *NIST* [3(a) and 3(b)], and *AMC2* [4(a) and 4(b)]. (a)s are for the mean value of the boundary discontinuity and (b)s are for the standard deviation of the boundary discontinuity. In all cases, the blue curves are the real results, while the red curves in the (a) are the theoretically predicted results.

Now, we study the multi-day data-arc boundary discontinuity. Similar to Eq. (2.1), the multi-day data-arc boundary discontinuity can be computed by Eq. (2.3).

$$BD^{M}_{M,M+1} = \Delta^{M}_{M+1,2M} - \Delta^{M}_{1,M}. \tag{2.3}$$

Now we plug in Eq. (2.2), obtaining

$$BD^{M}_{M,M+1} = \frac{[(\Delta^{1}_{M+1,M+1}+\Delta^{1}_{M+2,M+2}+\cdots+\Delta^{1}_{2M,2M})-(\Delta^{1}_{1,1}+\Delta^{1}_{2,2}+\cdots+\Delta^{1}_{M,M})]}{M}. \quad (2.4)$$

Because of Eq. (2.1), we can express the M-day data-arc boundary discontinuity $BD^{M}_{M,M+1}$ by the day boundary discontinuity $BD^{1}_{i,i+1}$. That is,

$$BD^{M}_{M,M+1} = (\sum_{i=1}^{M} BD^{1}_{i,i+1} + \sum_{i=2}^{M+1} BD^{1}_{i,i+1} + \cdots + \sum_{i=M}^{2M-1} BD^{1}_{i,i+1})/M. \quad (2.5)$$

Next, we study the statistics of the M-day data-arc boundary discontinuity.

First, for the expectation, we have the following equation:

$$E(BD^{M}_{M,M+1}) = E(\frac{\sum_{i=1}^{M} BD^{1}_{i,i+1} + \sum_{i=2}^{M+1} BD^{1}_{i,i+1} + \cdots + \sum_{i=M}^{2M-1} BD^{1}_{i,i+1}}{M}). \quad (2.6)$$

Because $BD^{1}_{i,i+1}$ observes the same distribution, we further have

$$E(BD^{M}_{M,M+1}) = \frac{M\cdot E(BD^{1}_{i,i+1}) + M\cdot E(BD^{1}_{i,i+1}) + \cdots + M\cdot E(BD^{1}_{i,i+1})}{M} = M \cdot E(BD^{1}_{i,i+1}). \quad (2.7)$$

Eq. (2.7) tells us that the mean value of the M-day data-arc boundary discontinuity is proportional to the data-arc length M. This theoretical calculation matches our actual results in Figure 2.8. The theoretically predicted mean value (red curve in all (a) figures) is very close to the actual mean value (blue curve in all (a) figures).

Second, we study the standard deviation of $BD^{M}_{M,M+1}$. Here, we can have two different, but both reasonable, assumptions. The two assumptions lead to completely different conclusions.

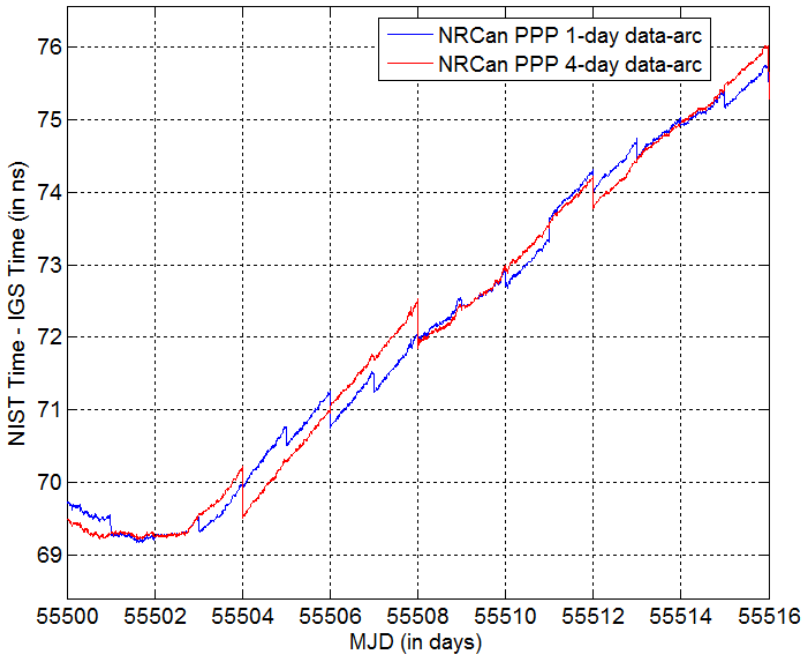

Figure 2.9. Illustration of Eq. (2.2). The blue curve is the 1-day data-arc NRCan PPP result, and the red curve is the 4-day data-arc NRCan PPP result. Clearly, the 4-day data-arc PPP result (the red curve) is almost an average of the four 1-day data-arc PPP results.

The first assumption is that for any k, $\Delta^1_{k,k}$ is Gaussian distributed and it is independent from $\Delta^1_{i,i}$ (where $i \neq k$). Physically, this assumption is based on the fact that the noise in the measurements is white, and thus the distribution of the estimated phase ambiguities is Gaussian. If this assumption is true, Eq. (2.4) reveals that

$$STD(BD^M_{M,M+1}) = \frac{1}{M}\sqrt{2M \cdot Var(\Delta^1_{i,i})} = \sqrt{\frac{2}{M}}STD(\Delta^1_{i,i}). \tag{2.8}$$

Because

$$STD(BD^1_{i,i+1}) = \sqrt{2}STD(\Delta^1_{i,i}), \tag{2.9}$$

we have

$$STD(BD^{M}_{M,M+1}) = \sqrt{\frac{1}{M}}\,STD(BD^{1}_{i,i+1}). \tag{2.10}$$

Eq. (2.10) tells us that the STD of the M-day data-arc boundary discontinuity is proportional to $\sqrt{\frac{1}{M}}$. Thus, by increasing the length of data-arc to a large value, the STD of the boundary discontinuity can be almost 0.

The second assumption is that $BD^{1}_{k,k+1}$ is Gaussian distributed and independent from $BD^{1}_{i,i+1}$ (where $i \neq k$). This assumption also makes sense because previous studies (see [18]) show that the boundary discontinuity can affect the slope of the PPP result. Thus, the boundary discontinuity may be more fundamental than the time shift Δ. So we can possibly assume that BD is white and independent. If this assumption is correct, Δ is actually a random-walk process, becasue $\Delta^{1}_{i+1,i+1} = \Delta^{1}_{i,i} + BD^{1}_{M,M+1}$. According to Eq. (2.5), we have

$$STD(BD^{M}_{M,M+1}) = STD\left(\frac{BD^{1}_{1,2}+2\cdot BD^{1}_{2,3}+\cdots+M\cdot BD^{1}_{M,M+1}+(M-1)\cdot BD^{1}_{M+1,M+2}+\cdots+BD^{1}_{2M-1,2M}}{M}\right), \tag{2.11}$$

thus, $STD(BD^{M}_{M,M+1}) = \frac{1}{M}STD\left(BD^{1}_{i,i+1}\right)\cdot\sqrt{1^2+2^2+\cdots+M^2+(M-1)^2+\cdots+1^2}$. (2.12)

Further simplification gives

$$STD(BD^{M}_{M,M+1}) = \sqrt{\frac{2M^3+M}{3M^2}}\,STD\left(BD^{1}_{i,i+1}\right). \tag{2.13}$$

When M is large, we have

$$STD(BD^{M}_{M,M+1}) \cong \sqrt{\frac{2M}{3}}\,STD\left(BD^{1}_{i,i+1}\right). \tag{2.14}$$

Thus, the STD of the M-day data-arc boundary discontinuity is proportional to $\sqrt{\frac{2M}{3}}$ when M is large.

Our actual results shown in Figure 2.8 (b) series are quite far away from what our first assumption predicts. In contrast, we can see that the second assumption works quite well for *USN3*. For other receivers, the STD of the boundary discontinuity increases, but not as much as $\sqrt{\frac{2M^3+M}{3M^2}}$. This may come from the case that there may have some correlation between two consecutive boundary discontinuities or that we are at somewhere between the first and second assumptions.

In a whole, the theoretical study shows that $Mean \propto Data\ Arc\ Length$. But for the STD, it could be either proportional to $\sqrt{Data\ Arc\ Length}$ or $1/\sqrt{Data\ Arc\ Length}$. The actual result matches the theoretical prediction on the mean value of the boundary discontinuity. The fact that the actual STD of the boundary discontinuity is closer to the tendency of $\sqrt{Data\ Arc\ Length}$ indicates that the PPP result is closer to a Brownian (or random-walk) process.

2.6 Other PPP Software Packages

Although NRCan PPP is a standard PPP program in the time transfer community, we still want to compare it with other PPP programs because other PPP programs may be comparable to or even better than NRCan PPP. Besides, other PPPs may be a good substitute when NRCan PPP is not available.

Here, we choose Atomium PPP [45–46] and Novatel PPP (or Novatel GrafNav PPP) to compare with NRCan PPP. Atomium PPP was developed by Dr. Pascale Defraigne who is well known in the time-transfer community. She has studied the

boundary discontinuity for many years. Thus, there may be some advantages of using Atomium PPP over NRCan PPP, in terms of boundary discontinuity. On the other hand, Novatel PPP is a commercial PPP program. It has a fancy graphic user interface and many useful functions (e.g., it can process GLONASS data; and it can process data forward, then reverse, and then forward again). Since Novatel is not targeted toward the time-transfer community, its performance of precise timing may not be as good as NRCan PPP and Atomium PPP. However, it is still interesting to evaluate the performance of such a commercial PPP in the area of precise timing.

Our main concerns about the performance of a PPP program are boundary discontinuity and frequency stability. To do the comparison, we first run the three PPP programs (i.e., NRCan, Atomium, Novatel) for *NIST*, *USN3* and *PTBB* for MJD 55600–55750 with respect to the IGS final time. We can clearly see from Figures 2.10–2.12 that all three curves are very close, indicating that all PPPs give very similar long-term (> 5 days) time-transfer results. However, the Novatel PPP result for *PTBB* has many outliers/spikes. These anomalies indicate that Novatel PPP may not be as robust as the other two PPPs.

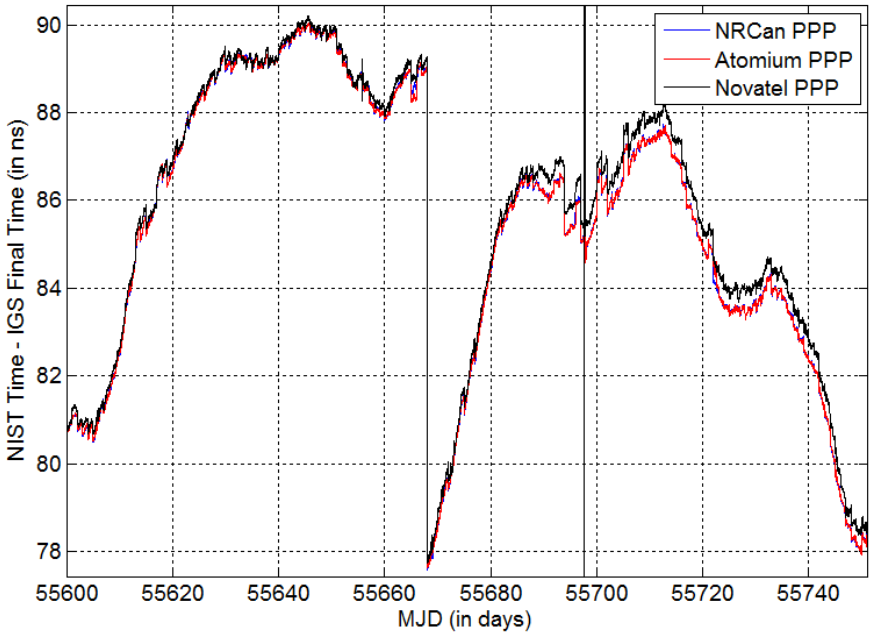

Figure 2.10. The results of three PPPs (NRCan, Atomium, and Novatel) for the *NIST* time with respect to the IGS final time, for MJD 55600–55750.

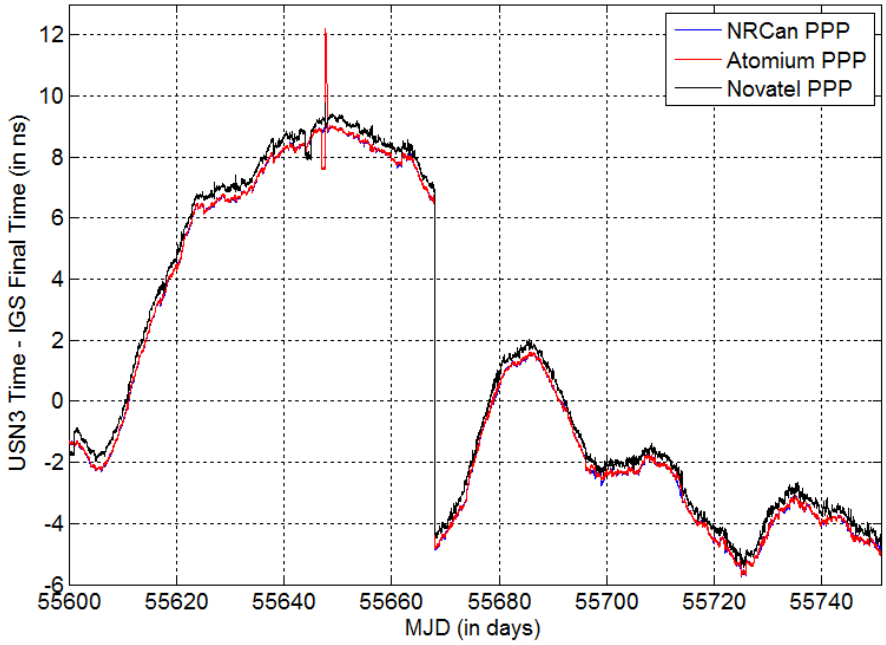

Figure 2.11. The results of three PPPs (NRCan, Atomium, and Novatel) for the *USN3* time with respect to the IGS final time, for MJD 55600–55750.

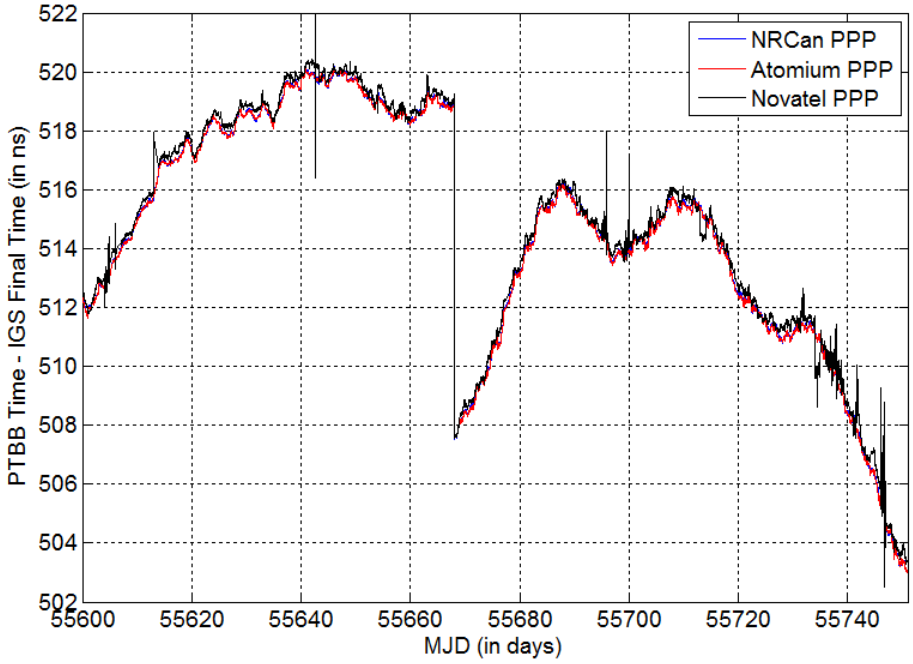

Figure 2.12. The results of three PPPs (NRCan, Atomium, and Novatel) for the *PTBB* time with respect to the IGS final time, for MJD 55600–55750.

The STDs of the boundary discontinuity for the three PPPs are shown in Table 2.1. Obviously, NRCan PPP and Atomium PPP have almost the same STD of the boundary discontinuity. In addition, they typically provide a smaller boundary discontinuity than Novatel PPP.

Next, we study the frequency stability of the three PPPs. We first enlarge Figures 2.10–2.11 to see the stability in the time-domain (Figures 2.13–2.14). Clearly, all three curves in Figures 2.13–2.14 have similar patterns. They reach the maxima and minima at the same epochs. For *NIST* (Figure 2.13), the three PPPs have quite comparable results. However, Novatel PPP is noiser than NRCan and Atomium for *USN3* (Figure 2.14). The tiny peaks in the blue/red curve are enlarged in the black curve! For example, in Figure 2.14, at around MJD 55653.5, there is a

peak of greater than 0.1 ns, while in the blue and red curves, the peaks are negligible. In the frequency domain (see Figures 2.15–2.16), we further confirm our above observation that Novatel PPP is noisier than NRCan PPP and Atomium PPP for *USN3*. Figure 2.16 shows that Novatel PPP is much worse than the other two for the averaging time of 1000 to 100,000 sec, for *USN3*.

Table 2.1. The standard deviation (STD) of the boundary discontinuity of the three PPPs (NRCan, Atomium, and Novatel) for *NIST*, *USN3*, and *PTBB*. Note, the STD of the Novatel PPP for *PTBB* STD (i.e., 308.4 ps) is the result after the dates with spikes in Figure 2.13 have already been removed.

	NRCan PPP	Atomium PPP	Novatel PPP
NIST	243.5 ps	247.8 ps	238.3 ps
USN3	118.6 ps	118.7 ps	192.1 ps
PTBB	145.3 ps	155.0 ps	308.4 ps

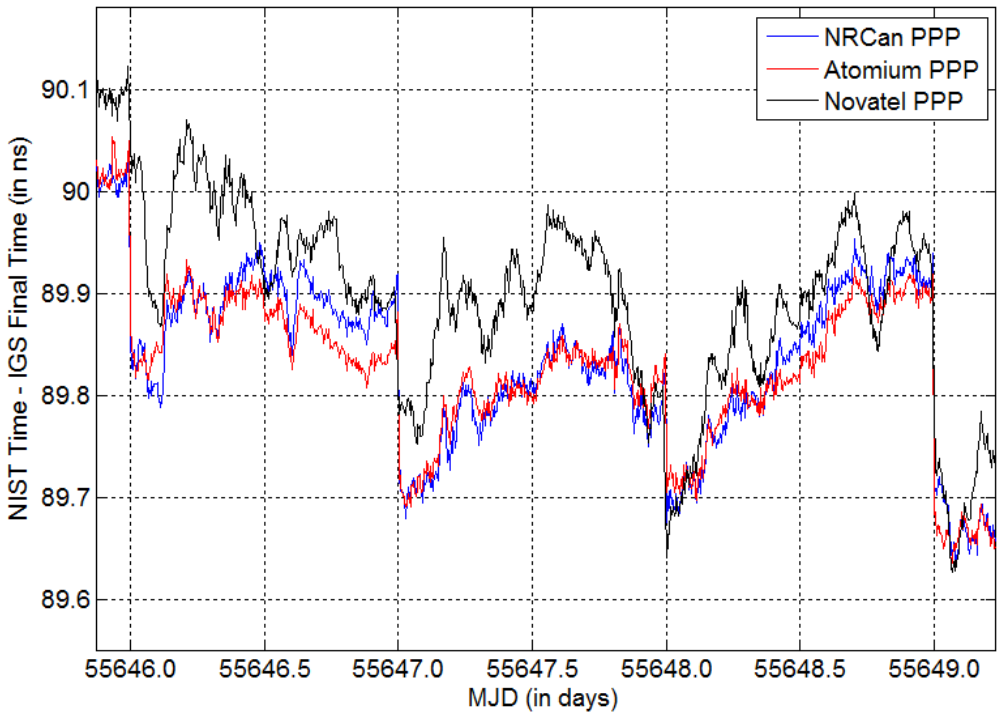

Figure 2.13. The results of three PPPs (NRCan, Atomium, and Novatel) for the *NIST* time with respect to the IGS final time, for MJD 55646–55648. This figure is enlarged from Figure 2.11.

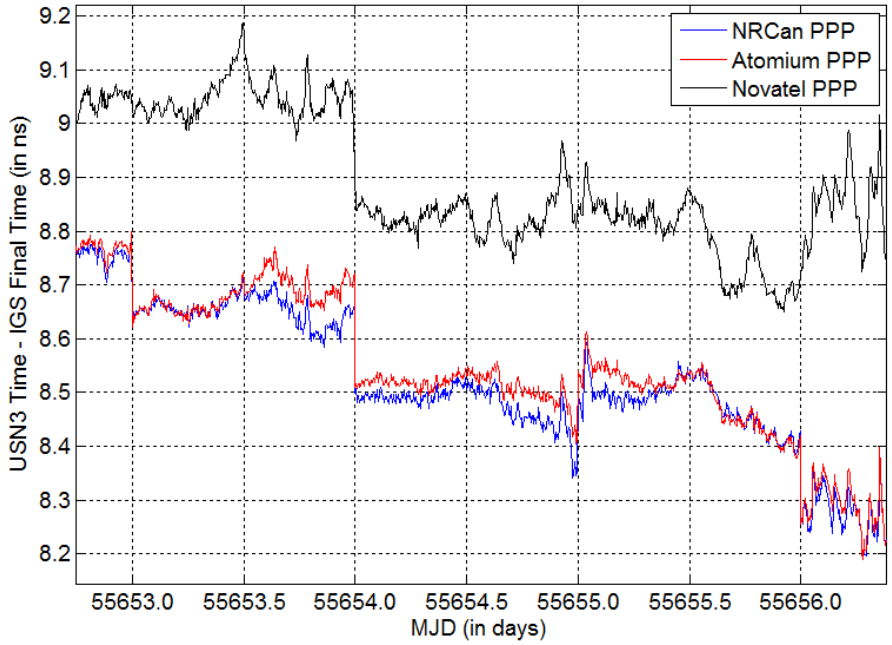

Figure 2.14. The results of three PPPs (NRCan, Atomium, and Novatel) for the *USN3* time with respect to the IGS final time, for MJD 55653–55655. This figure is enlarged from Figure 2.12.

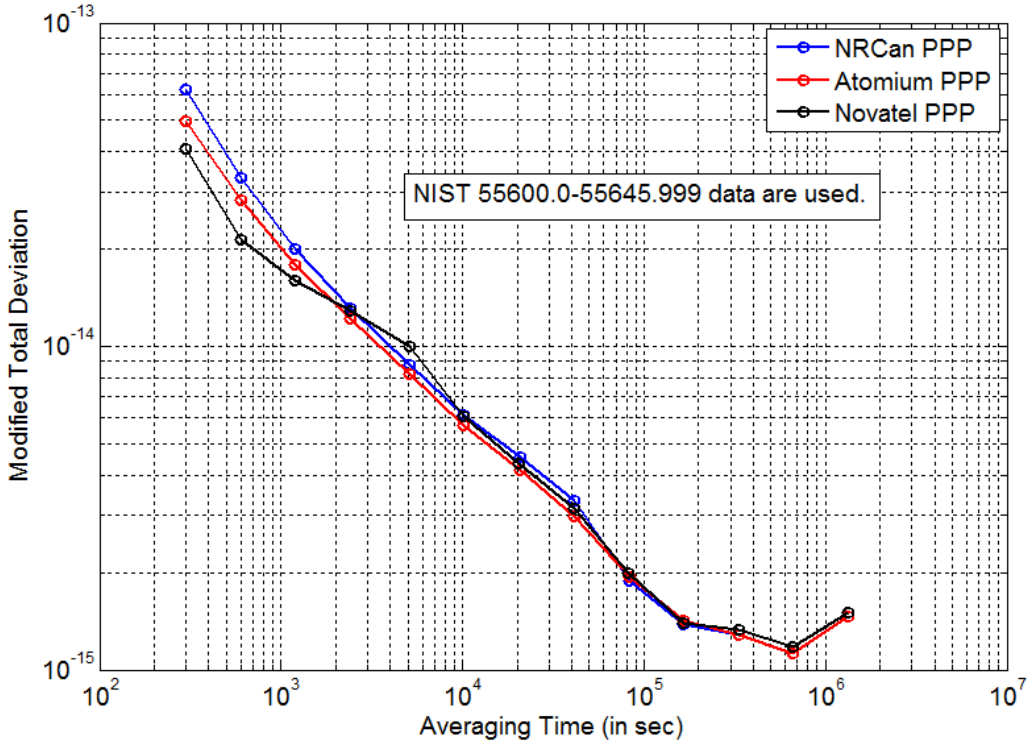

Figure 2.15. Frequency stability analysis of the three PPPs (NRCan, Atomium, and Novatel) for *NIST*, for MJD 55600–55645.

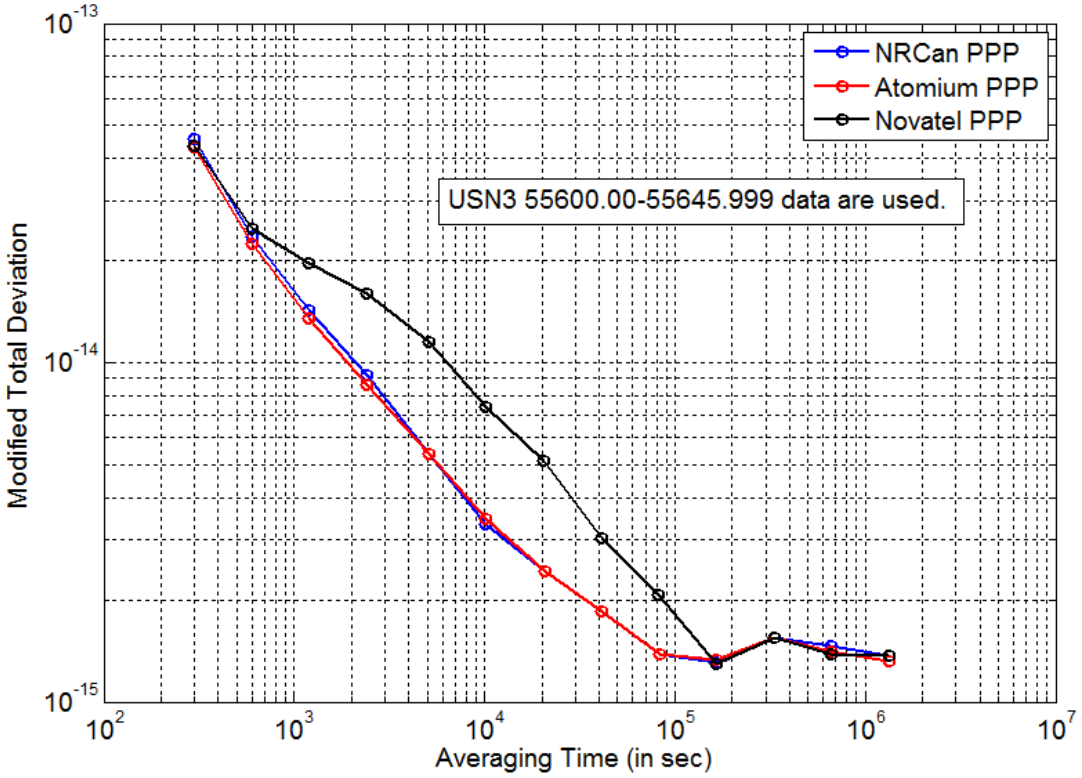

Figure 2.16. Frequency stability analysis of the three PPPs (NRCan, Atomium, and Novatel) for *USN3*, for MJD 55600–55645.

In summary, NRCan PPP and Atomium PPP exhibit a very similar performance in terms of boundary discontinuity and frequency stability. The Novatel PPP only works well for some stations. For other stations, the Novatel PPP timing results could have many outliers. In addition, Novatel PPP typically provides a bigger boundary discontinuity and worse frequency stability than the other two PPPs. Therefore, NRCan PPP and Atomium PPP are better than Novatel PPP.

2.7 Appendix: Gaussian-Distribution Test of Boundary Discontinuity

In this section, we test whether the boundary discontinuity satisfies the Gaussian distribution or not. Here, we use chi-squared (χ^2) test to determine the Gaussian distribution.

The basic principle of χ^2 test is as follows[1].

First, our null hypothesis states that the distribution of the boundary discontinuity is Gaussian. Next, the N boundary-discontinuity observations are divided among n equally-spaced cells. In each cell, we have O_i observations. The expected number of observations in each cell is E_i, based on the Gaussian distribution model. Then we get the following quantity.

$$\chi^2 = \sum_{i=1}^{n} \frac{(O_i - E_i)^2}{E_i}. \tag{2.15}$$

It can be shown that for the significance level α, if

$$\chi^2 \geq \chi_\alpha^2(n - m - 1), \tag{2.16}$$

where m is the number of unknown variables in the distribution model (in our case, m=2, because only the mean and STD in the Gaussian distribution are unknown), then we reject our null hypothesis at the significance level α.

Now let's apply the χ^2 test to the Gaussian-distribution test of boundary discontinuity. Figure 2.17 shows the boundary discontinuities of five GPS receivers with respect to the IGS final time, instead of the IGR time. Comparing this figure with Figure 2.7, we can see that the mean value and the STD are very close for

[1] The principle of χ^2 test is mainly based on "Pearson's chi-squared test" of Wikipedia. The website link is http://en.wikipedia.org/wiki/Pearson's_chi-squared_test.

NIST, *PTBB*, and *USN3*. This further confirms our statement in Section 2.2 that the boundary discontinuity behavior does not change regardless of whether the IGS final products or the IGS rapid products are used.

Actually, we do not need to implement the algorithm of the above χ^2 test by ourselves. MATLAB has already provided a function, called "chi2gof"[1], to do the χ^2 test for a Gaussian distribution. Here, we set the significance level $\alpha = 0.03$, which is a common setting. The corresponding command is "h = chi2gof(x, 'Alpha', 0.03)". If h is 0, then the test decision is that the data in vector x come from a Gaussian distribution with the significance level of 0.03.

The results show that *PTBB*, *USN3*, *OPMT*, and *USNO* pass the Gaussian distribution test. *NIST* is the only one that fails. Figure 2.17(a) tells us why *NIST* fails. There are a few big boundary discontinuities with more than 0.5 ns jump values. This makes the red curve wider than it should be. In the end, it makes the blue bars not match the red curve very well. This results in that *NIST* fails the Gaussian-distribution test. Without those big jumps, we can see that *NIST* still observes the Gaussian distribution. Based on the above analysis, we conclude that the boundary discontinuity is Gaussian at the significance level of 0.03. Or simply put, the boundary discontinuity is almost Gaussian.

[1] See http://www.mathworks.com/help/stats/chi2gof.html.

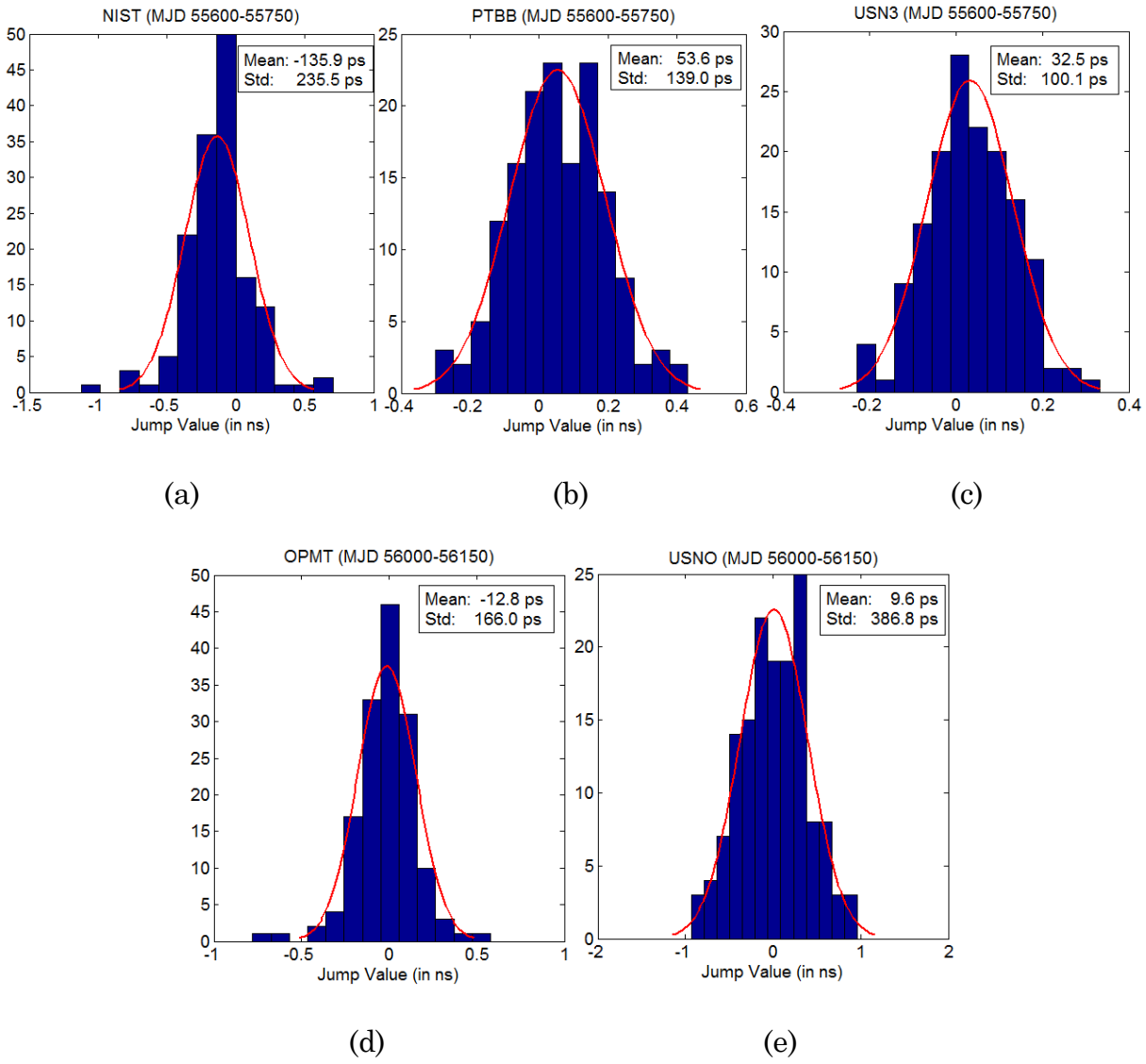

Figure 2.17. Histograms of jumps of *NIST*, *PTBB*, *USN3*, *OPMT*, and *USNO* with respect to the IGS final time. The red curve in each plot is the Gaussian-distribution fit.

Chapter 3

Origin of Day Boundary Discontinuity[1]

3.1 Introduction: Noise and Boundary Discontinuity

As stated in Section 1.5.1, in theory, the boundary discontinuity comes from both the code and phase noise. Here, we simulate the impact of the code and phase noise on the boundary discontinuity.

There are basically two methods for doing the simulation. One method is to generate ideal noise-free RINEX data. Then we add noise to the RINEX data and see the change in the boundary discontinuity. The difficulty with this method comes from the generation of noise-free RINEX data. Although there are some software packages available in the world [48], we do not know their details, e.g., whether they include the ionospheric and tropospheric delays. We may also need to revise the PPP software package to remove some corrections in PPP.

The other method involves adding white noise to the original measured RINEX data and studying the change in the boundary discontinuity. This method is easier

[1] The results of this chapter are mainly based on [18, 47].

to implement. And, it can reveal the relationship between measurement noise and boundary discontinuity quite effectively.

Here, we use the second method for our simulation. First, we keep the phase noise at the noise level of 0.01 cycle and increase the code noise from 0.0 m to 0.5 m (Figure 3.1). One thousand trials are done for each code noise level to get a reliable statistical distribution. We can see from Figure 3.1 that the STD of the clock offset at epoch 0 (that is, the very beginning epoch of the day) increases almost linearly as the code noise increases. For a code noise of 0.3 m and a phase noise of 0.01 cycle, which is a common noise level for the RINEX data, the STD is 85 ps, which corresponds to the STD of the boundary discontinuity of 85 ps $\times\sqrt{2}$ = 120 ps. This value matches the statistical result of the boundary discontinuity in Section 2.4 quite well.

We can also see from Figure 3.2 that the STD of the clock offset at epoch 0 changes little for a phase noise in the range of 0.00–0.02 cycle. Because the phase noise of the RINEX data after corrections (such as the satellite clock offsets, the earth tide, etc.) is typically below 0.02 cycle, the phase noise has little impact on the boundary discontinuity.

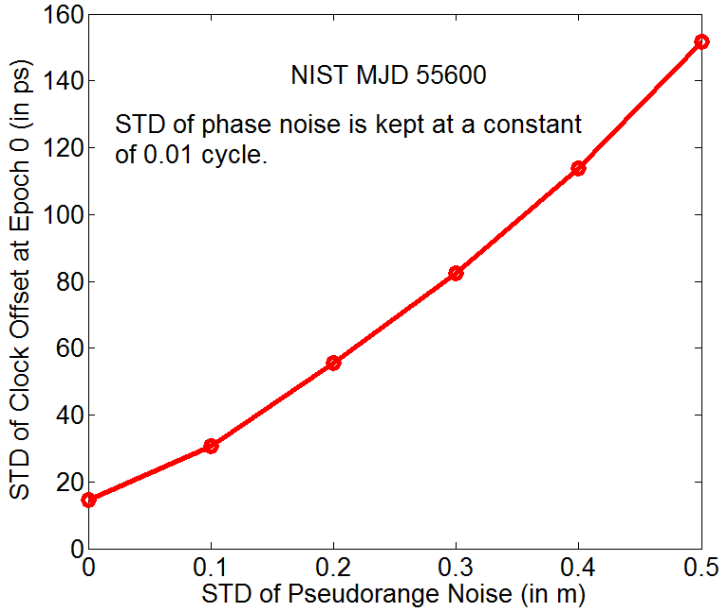

Figure 3.1. Relation between the clock offset at epoch 0 and the code noise (simulation result). The phase noise is kept at the STD of 0.01 cycle.

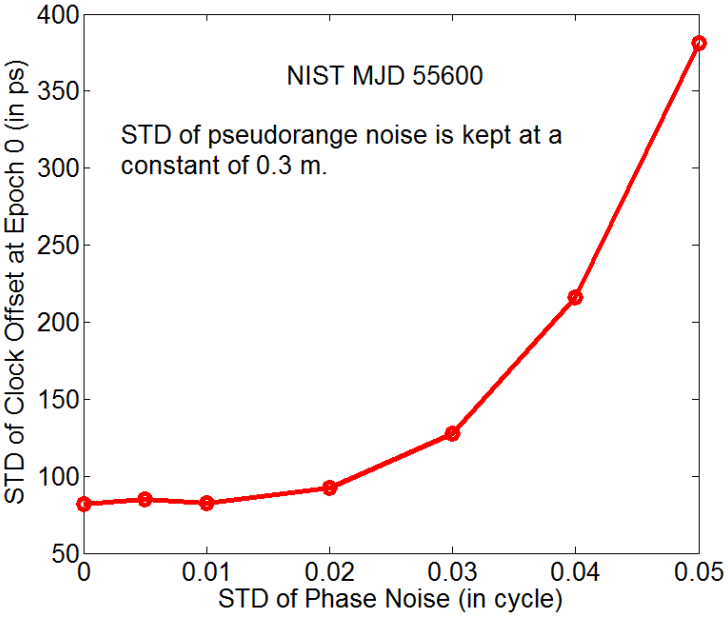

Figure 3.2. Relation between the clock offset at epoch 0 and the phase noise (simulation result). The pseudorange noise is kept at the STD of 0.3 m.

Next, we study the relation between the short-term (300 sec) stability of the carrier-phase (CP) time transfer and the measurement noise (Figure 3.3). The time deviation (TDEV) at an averaging time of 300 sec is used to characterize the short-term stability. The six curves in Figure 3.3 are very close to each other, which indicates that the code noise has little impact on the short-term stability of CP time transfer. TDEV (300 sec) increases from 8 ps to approximately 50 ps as the phase noise increases from 0 cycle to 0.05 cycle. This increase shows that the phase measurement plays an important role in the short-term CP time transfer.

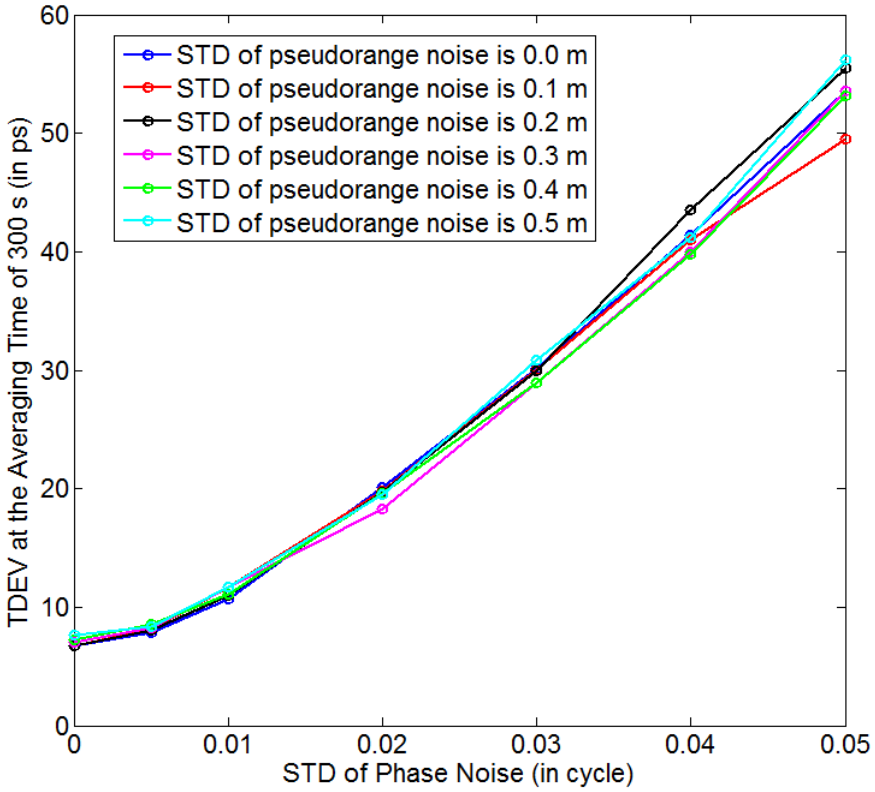

Figure 3.3. TDEV at 300 sec for different pseudorange noise and phase noise levels (simulation result).

The above analysis confirms our theoretical study reported in Section 1.5.1 that showed that both the code noise and the phase noise can affect boundary discontinuity. Practically, however, the phase noise is typically too small (< 0.02 cycle) to cause an effect. Therefore, the code noise is much more critical to the boundary discontinuity than the phase noise.

The code noise [see Eq. (1.5)] can be divided into two categories: systematic noise and outliers (or anomalies). Systematic noise can be further divided into three sub-categories: satellite-related noise, path-related noise, and receiver-related noise. Such systematic noise is always there, and the noise level typically remains very stable unless there is a sudden big improvement of the system design (such as the update of a GPS receiver, or a better estimate of the satellite clock offset by a new algorithm).

The satellite-related noise mainly comes from the uncertainty of satellite clock offset and position. IGS provides the IGS 30-sec clock product that has more information about the satellite clocks than the IGS 5-min clock product. Thus, using the IGS 30-sec clock product as the input of PPP can potentially reduce the boundary discontinuity. This issue will be discussed in Section 3.2. However, IGS does not provide the IGS 30-sec sp3 product. Thus, we cannot evaluate the impact of the satellite position on the boundary discontinuity, at least for the time being. However, we believe that the IGS 30-sec sp3 product [49] has a similar effect on the boundary discontinuity as the IGS 30-sec clock product.

The path-related noise is mainly ionospheric noise and tropospheric noise. The ionospheric noise can be cancelled out to the first order by using dual-frequency measurements. This is what the PPP does. However, the second order of ionospheric noise can still be as big as a few centimeters [50]. Triple-frequency measurements can cancel out the ionospheric noise to the second order. But a triple-frequency GPS receiver is not available in our lab. Therefore, we cannot explore the impact of high-order ionospheric noise on boundary discontinuity in this thesis. The tropospheric noise will be discussed in Section 3.3.

Section 3.4 will explore the receiver-related noise and propose a practical method for reducing the impact of the receiver-related noise on the boundary discontinuity.

An outlier or an anomaly in the RINEX data occurs quite unpredictably. The origin of an outlier can be almost anything. For example, the GPS receiver loses the tracking of a satellite, or the satellite-receiver line is blocked by an object, or the reference time for the receiver is adjusted, or even a man-made error occurs. The relationship between an outlier and the boundary discontinuity will be discussed in Section 3.5.

Note that the results in Sections 3.2–3.5 are all based on the PPP program. As mentioned in Section 1.5.2, the other implementation of the carrier-phase time transfer is the network method. Section 3.6 compares the PPP method with the network method. We'll see that the network method is superior to the PPP method, in terms of boundary discontinuity.

3.2 IGS Clock Data and Boundary Discontinuity

IGS provides the IGS 30-sec clock product that has more information about the satellite clocks than the IGS 5-min clock product. Therefore, using the IGS 30-sec clock product as the input of PPP could potentially reduce the boundary discontinuity.

Figure 3.4 confirms this prediction. We run PPP for *PTBB* (a GPS receiver in PTB, Germany) from Modified Julian Day (MJD) 56050 to MJD 56200 with the IGS 5-min clock product as the input [Figure 3.4(a)]. The STD of the boundary discontinuity jump values is 163.4 ps. Then we run PPP the same but with the IGS 30-sec clock product as the input [Figure 3.4(b)]. The STD of jump values becomes 115.7 ps. The improvement over the boundary discontinuity by using the IGS 30-sec clock product is as much as 29.2% for *PTBB*. Similarly, for *PTBG* (also in PTB, Germany), the improvement is 22.8% [Figure 3.4(c–d)]. In addition, the mean value of the boundary discontinuity becomes closer to 0 ps for both *PTBB* and *PTBG*.

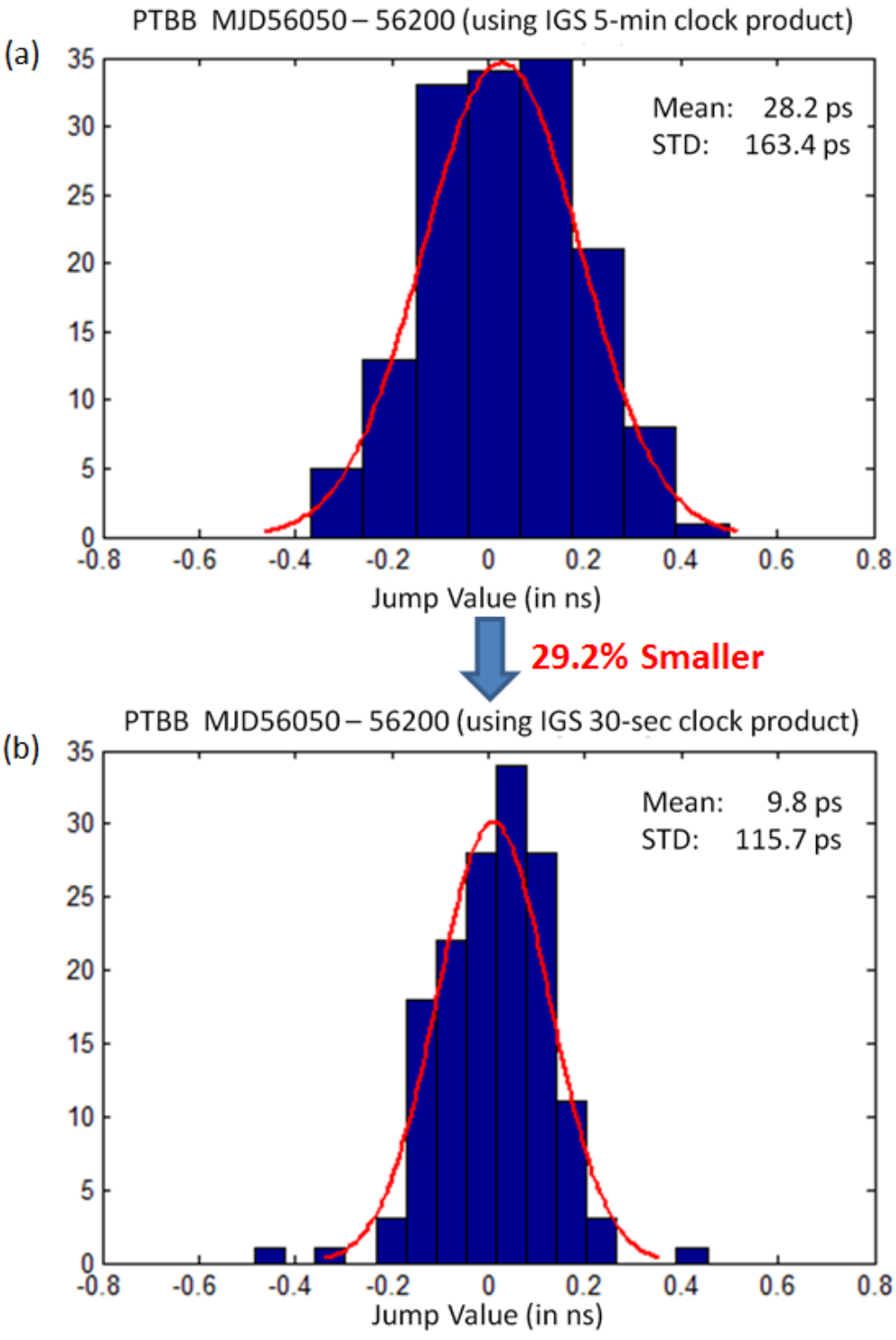
PTBB MJD56050 – 56200 (using IGS 5-min clock product)
(a)
Mean: 28.2 ps
STD: 163.4 ps
Jump Value (in ns)
29.2% Smaller
PTBB MJD56050 – 56200 (using IGS 30-sec clock product)
(b)
Mean: 9.8 ps
STD: 115.7 ps
Jump Value (in ns)

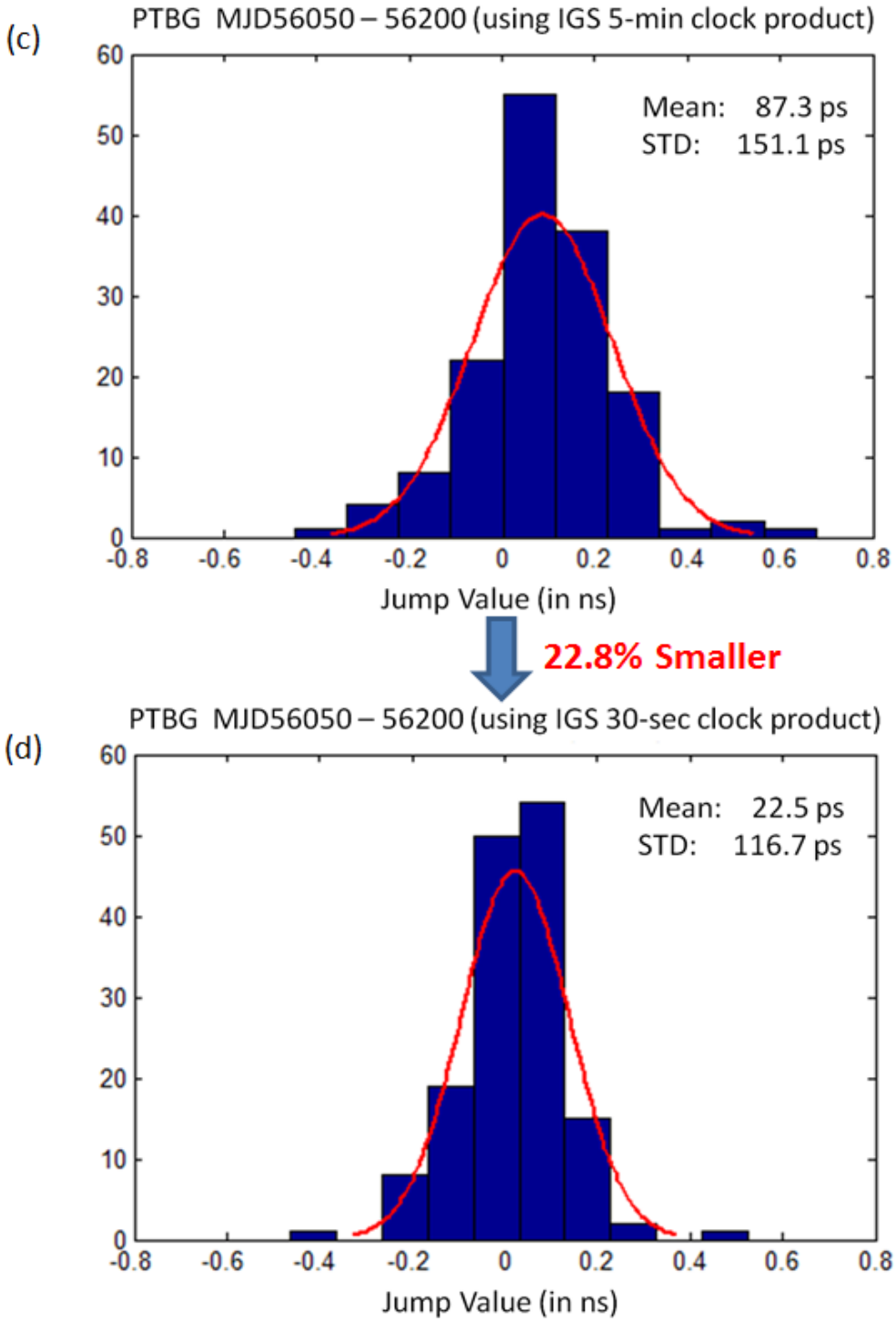

Figure 3.4. Boundary discontinuity using the IGS 5-min clock product vs using the IGS 30-sec clock product, for *PTBB* and *PTBG* from MJD 56050 to MJD 56200.

In principle, the time difference between two GPS receivers with the same reference time at a station should be a constant [51]. In practice, the time difference usually varies by a few nanoseconds. This variation comes from many reasons, such as the time-transfer noise, the receiver aging, the cable extension, etc. Thus, the comparison between two local GPS receivers can reveal whether there is any improvement of the time-transfer result. Figure 3.5 shows the time difference between *PTBB* and *PTBG* by using both IGS 5-min clock product and IGS 30-sec clock product. We can clearly see that the blue curve is obviously noisier than the red curve. This indicates that the time transfer result using the IGS 30-sec clock product is closer to the true values than that using the IGS 5-min clock product.

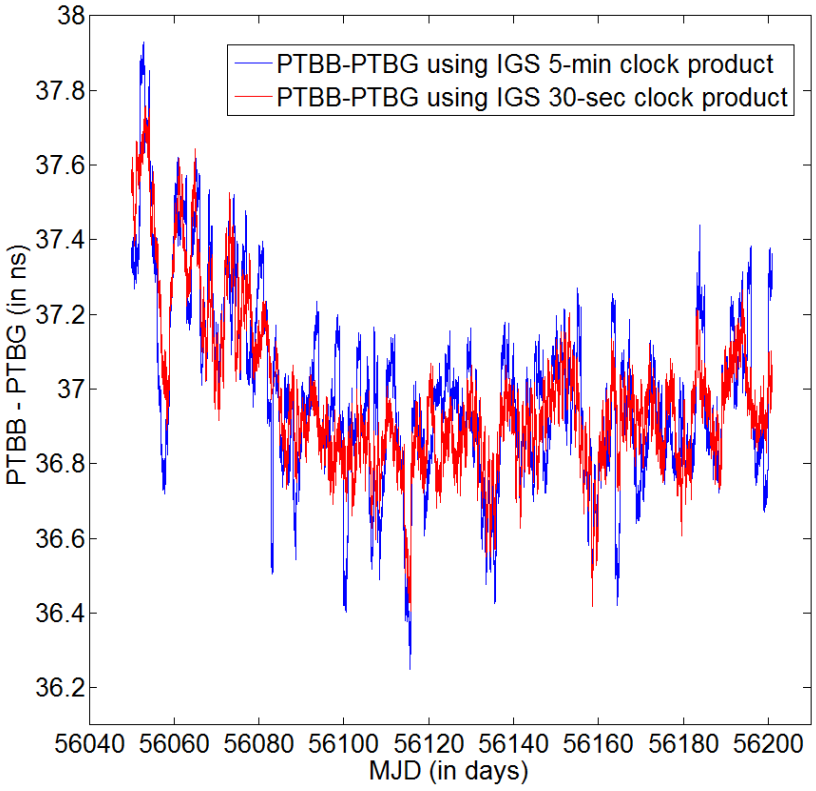

Figure 3.5. Time difference between *PTBB* and *PTBG* using the IGS 5-min clock product (blue curve) and using the IGS 30-sec clock product (red curve).

The improvement over the boundary discontinuity using the IGS 30-sec clock product at several timing laboratories in the world is shown in Figure 3.6. The improvement is typically 10–30%.

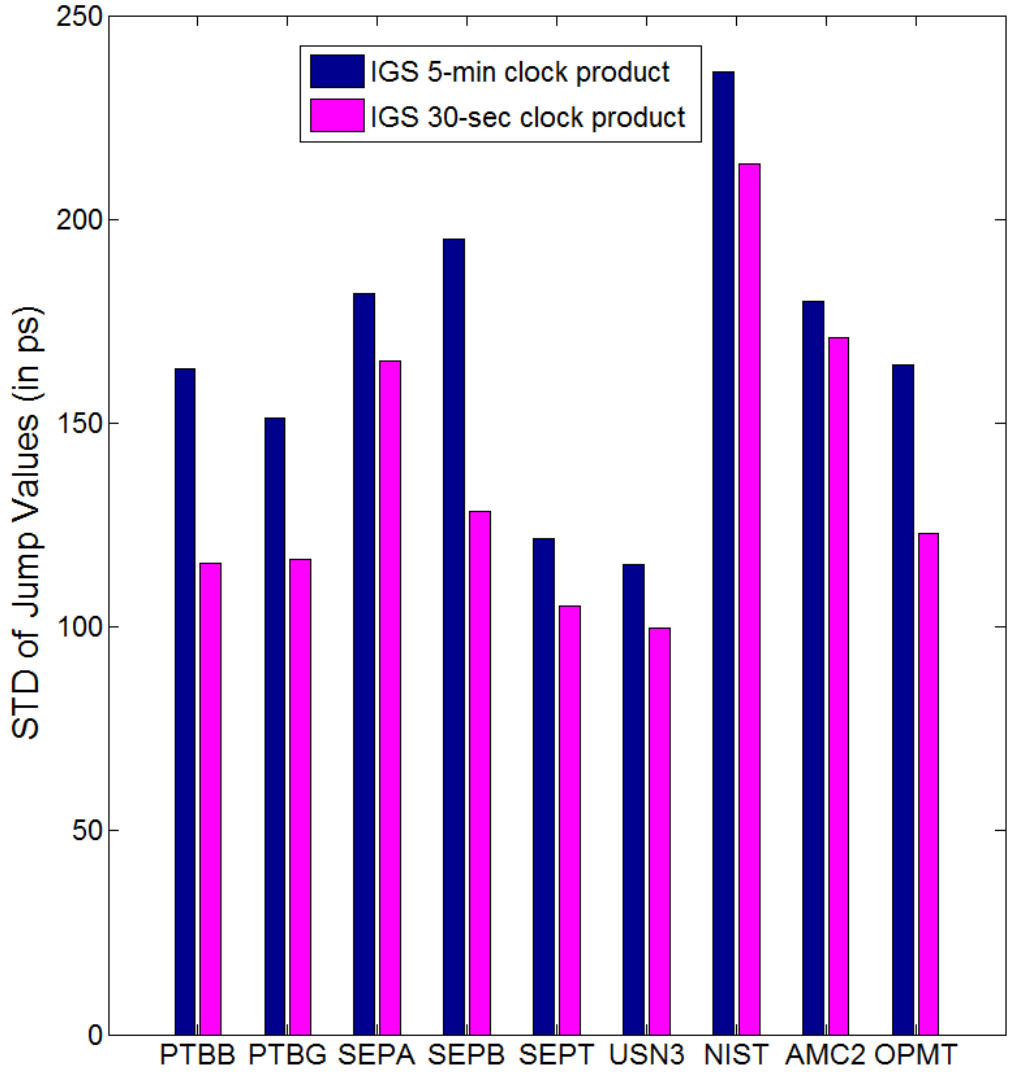

Figure 3.6. Boundary discontinuity using the IGS 5-min clock product vs using the IGS 30-sec clock product, for several GPS receivers in the world (*PTBB* 56050-56200, *PTBG* 56050-56200, *SEPA* 55927-56077, *SEPB* 55927-56077, *SEPT* 55927-56077, *USN3* 56050-56200, *NIST* 55600-55750, *AMC2* 56050-56200, and *OPMT* 56050-56200).

3.3 Tropospheric Delay and Boundary Discontinuity

The tropospheric delay is separated into a predominant and well-behaved hydrostatic (or dry) part and a much smaller and volatile wet part. Each part can be expressed as a product of the zenith path delay (*ZPD*) and mapping function (*M*). Therefore, the Δ_{tropo} term in Eq. (1.5) can be expressed as

$$\Delta_{tropo} = M_{dry} * ZPD_{dry} + M_{wet} * ZPD_{wet}. \tag{3.1}$$

The dry *ZPD* (i.e., ZPD_{dry}) can be modeled and considered known, but the wet *ZPD* (i.e., ZPD_{wet}) must be estimated when running the PPP program [39].

There are several types of mapping functions, such as Niell mapping function (NMF), Global mapping function (GMF), and Vienna mapping function 1 (VMF1) [52].

NMF is expressed by Eq. (3.2):

$$M(e) = \frac{1+\frac{a}{1+\frac{b}{1+c}}}{\sin e+\frac{a}{\sin e+\frac{b}{\sin e+c}}}, \tag{3.2}$$

where *e* is the elevation of the satellite with respect to the GPS receiver, and the parameters *a*, *b*, and *c* are different for the hydrostatic and wet components of the atmosphere. Each of the parameters is a constant or a function of site latitude (symmetric about the equator) and day of year. Thus, NMF's temporal resolution is about one month. VMF1 uses the output of a numerical weather analysis to provide the information with a temporal resolution of six hours, specifically for a particular station. Thus, VMF1 provides a quite significant improvement of the tropospheric delay over NMF. GMF is a "back-up" mapping function or a compatible empirical

representation of VMF1. The parameters of a, b, c in GMF are computed based on the average of many years of data from the numerical weather model, instead of being estimated every 6 hours as in VMF1. Thus, GMF does not have as high resolution as VMF1. In fact, the temporal resolution of GMF is similar to that of NMF. Nevertheless, GMF is closer to the reality than NMF [52].

The three mapping functions of NMF, GMF, and VMF1 are shown in Figure 3.7. Clearly, VMF1 has a much higher resolution than the other two mapping functions. NMF is away from the average and thus leads to a bias in the tropospheric delay estimation. GMF is a good representation of VMF1 over the long term (a few months or more).

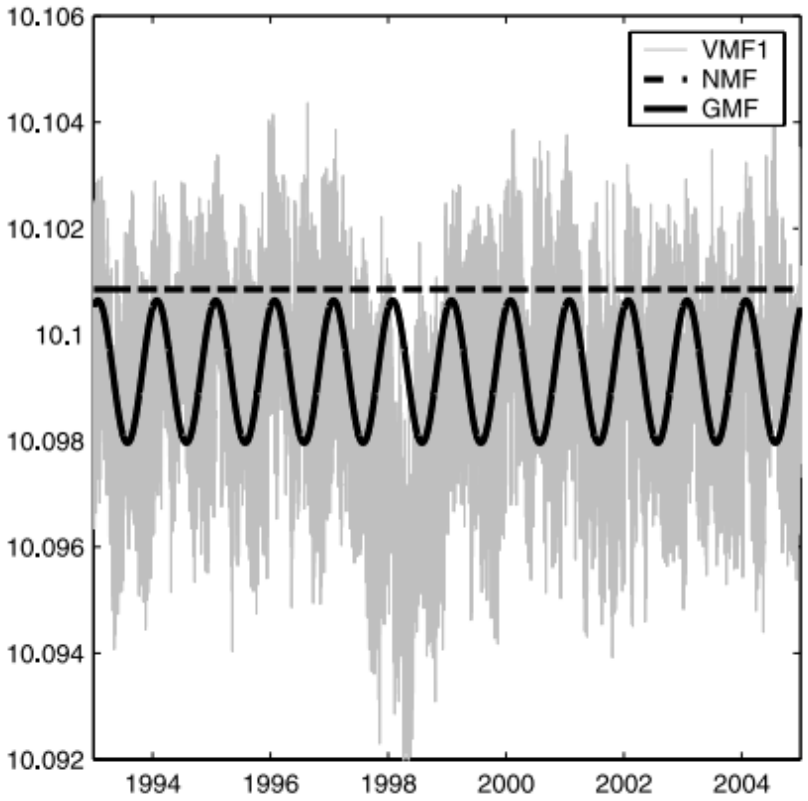

Figure 3.7. Hydrostatic (dry) mapping function at 5 degree elevation at Fortaleza, Brazil [52].

We use GMF and VMF1 in the PPP program because we want to know whether a mapping function affects the boundary discontinuity. Thus, we run the PPP program by using GMF and VMF1. In principle, the resolution of VMF1 (6 hours) is much higher than that of GMF (~1 month). Thus, if the tropospheric correction in the PPP matters a lot to the boundary discontinuity, then the boundary discontinuity should significantly decrease when we replace GMF with VMF1. However, the boundary discontinuities we obtain using GMF and VMF1 are almost the same (See Figures 3.8–3.9). This result indicates that the current tropospheric correction in PPP is already good enough, and thus the noise in the tropospheric correction has little impact on the boundary discontinuity.

3.4. Receiver-Related Noise and Boundary Discontinuity

Since we have already studied the relationship between satellite-related and path-related noise and the boundary discontinuity in Sections 3.2–3.3, the next step is to study the relationship between the receiver-related noise and the boundary discontinuity.

3.4.1. Boundary Discontinuity of Receivers at the Same Station

Receivers at the same station have many common features: the same GPS constellations, the same GPS signal transmission path, and the same reference time for the receiver. The measurements that receivers have done differ only in their multipaths, antennas, antenna-to-receiver cables, and receivers' internal circuits. Taken together, these differences make up "receiver-related noise". The noise in the

reference time for a receiver should typically be negligible, in a national timing laboratory. If the common features of receivers at the same station (i.e., the satellite-related noise and the path-related noise) play an important role in the boundary discontinuity, the jump values of receivers at the same station should be highly correlated.

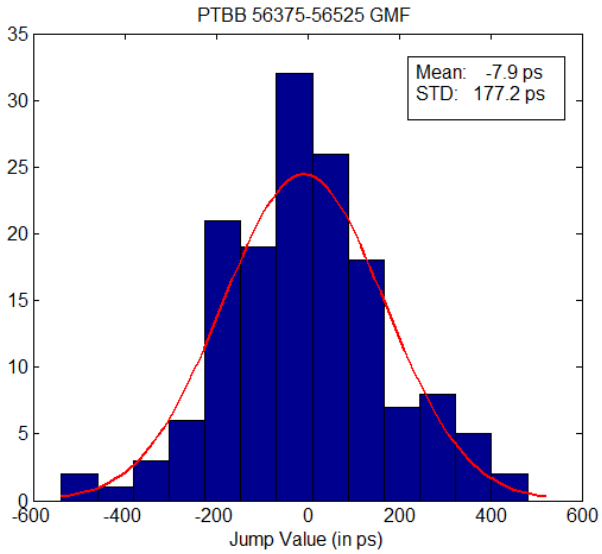

Figure 3.8. Histograms of jumps of *PTBB* for MJD 55600-55750, by using GMF.

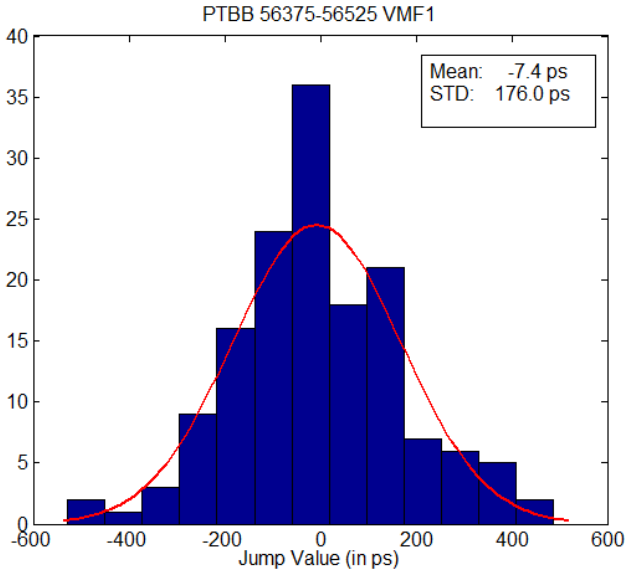

Figure 3.9. Histograms of jumps of *PTBB* for MJD 55600-55750, by using VMF1.

However, our experimental results contradict the above assumption. *SEPA*, *SEPB*, and *SEPT* are three GPS receivers at NICT (National Institute of Information and Communications Technology, Japan). They are all Septentrio POLARX2 receivers. The distance between each receiver is less than 5 m (See Figure 3.10). Based on the statistics of the jump values during MJD 55600–55750, the correlation coefficient between *SEPA* and *SEPB* is 0.471, which indicates a non-high correlation. For *SEPA* and *SEPT*, the correlation coefficient is even less, 0.215. The correlation coefficient between *SEPB* and *SEPT* is as small as 0.102. Thus, the jumps of several receivers at the same station are not highly correlated, even when the same type of receiver is used. To further confirm this, we performed a similar comparison for *PTBB* and *PTBG* at PTB (See Figure 3.11). The correlation coefficient is again very small, only −0.064. Based on the above analysis, we conclude that the noise from satellites and transmission paths can contribute to boundary discontinuity at some level, but not very much.

We also studied the correlation of jumps between two long-distance stations. It shows that the correlation between two long-distance stations is close to 0, e.g., *NIST* & *PTBB* −0.011, *NIST* & *USN3* −0.020, *USN3* & *PTBB* 0.110. This is exactly what we expect. After all, two long-distance stations have everything different. They observe different sets of GPS satellites. The transmission paths are different. The multipaths, antennas and receivers are also completely different.

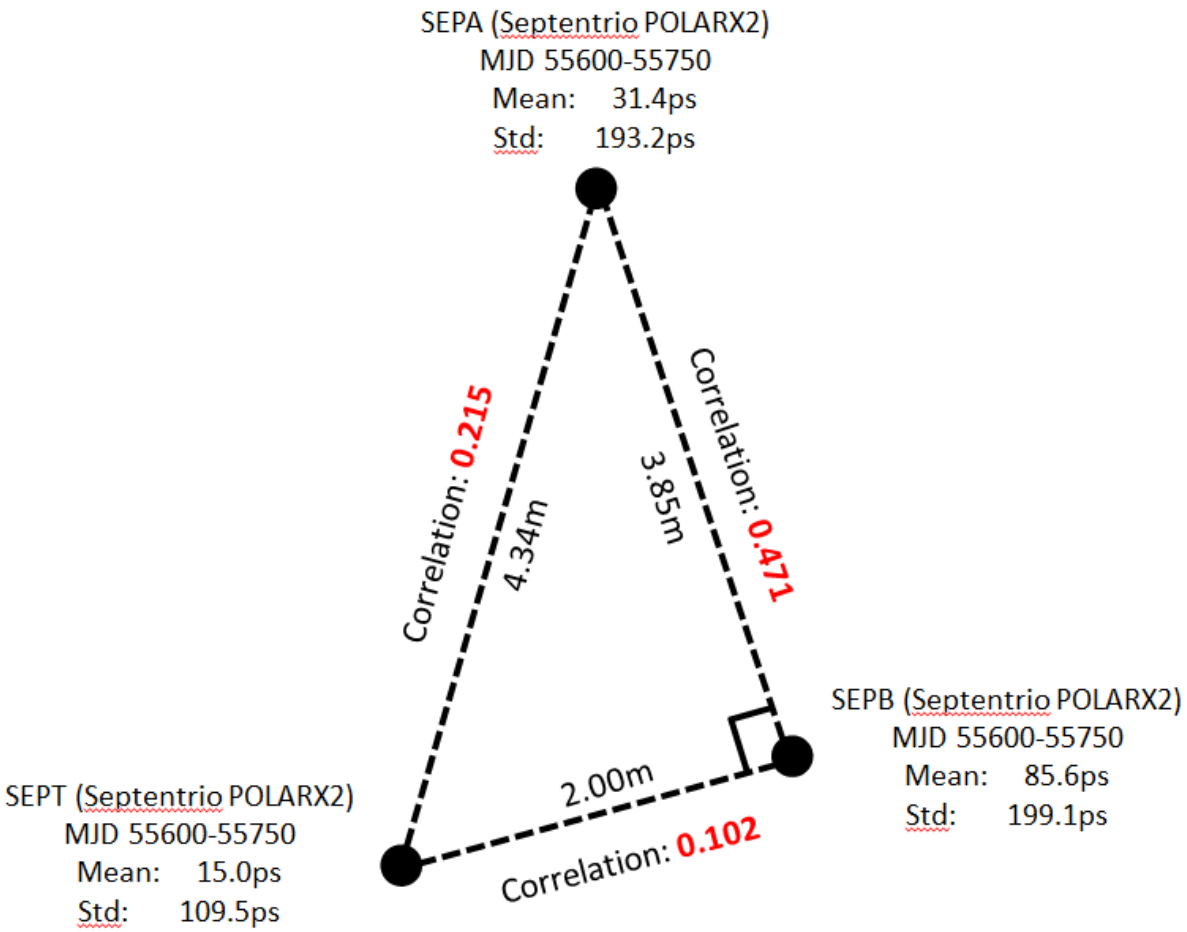

Figure 3.10 Correlation of boundary discontinuity of SEPA, SEPB, and SEPT at NICT, Japan.

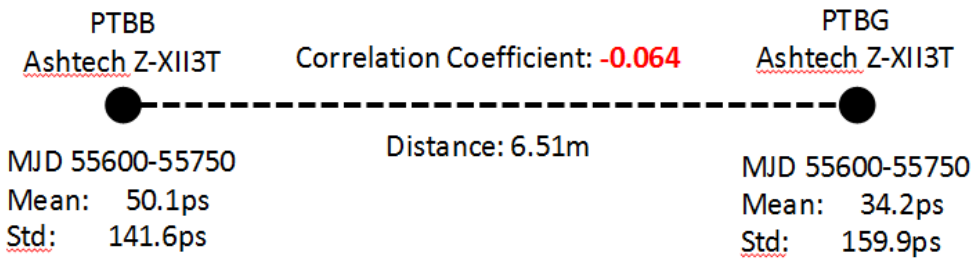

Figure 3.11. Correlation of boundary discontinuity of PTBB and PTBG at PTB, Germany.

3.4.2. Cutoff Elevation and Boundary Discontinuity

Of all types of receiver-related noise, multipath is an important factor to study. It varies from station to station. Multipath in code measurement is usually at the level of a few meters. Even with CP measurement smoothing, the code-measurement bias due to multipath can still be at a several-centimeters level, which can lead to a 100 ps clock bias. Besides, although multipath repeats every 23 h 56 min, it is different every 24 h, which may lead to different phase ambiguities between 2 days. Thus, it is necessary for us to explore the impact of multipath on a boundary discontinuity.

Increasing the cutoff elevation has two impacts. On the one hand, it blocks some multipath from the low elevations which form the main part of the total multipath. So from this point of view, we should expect a decrease of boundary discontinuity, if multipath does affect boundary discontinuity. On the other hand, increasing the cutoff elevation reduces the visible satellite number, which leads to fewer observations, so it increases the uncertainty of the computed phase ambiguity. So from this point of view, we should expect an increase of discontinuity. However, this increase should be very small because low-elevation observations are already given less weight than high-elevation observations. In sum, if the multipath affects our observation seriously, we should expect a big decrease of discontinuity as the cutoff elevation increases.

To find out the impact of multipath on the boundary discontinuity, we study the STD of boundary discontinuity of *USN3*, *PTBB*, and *SEPA* at different cutoff

elevations during MJD 55650–55850 (Figure 3.12). We can see that the increase of cutoff elevation gives little improvement on the boundary discontinuity. This illustrates that the multipath, at least at *USN3*, *PTBB*, and *SEPA*, is not an important factor on the magnitude of the boundary discontinuity.

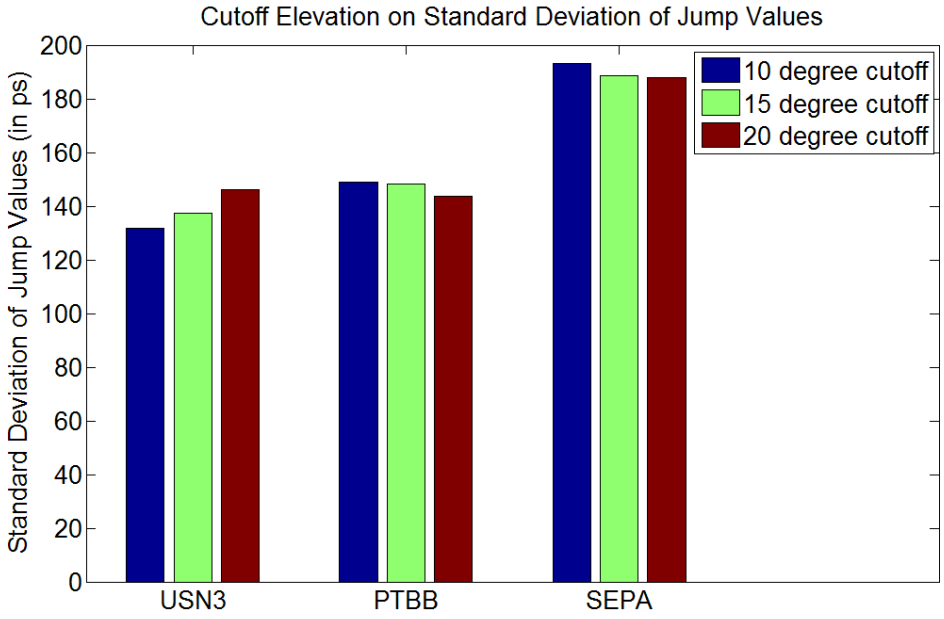

Figure 3.12. Effect of cutoff elevation on boundary discontinuity.

3.4.3. Receiver Noise

Receiver-related noise includes multipath, antenna noise, antenna-to-receiver noise, and receiver noise, as mentioned in Section 3.4.1. In this section, we focus on the receiver noise.

In 2006, two receivers (*NISA* (Ashtech Z12T) and *NISV* (Novatel T-Sync receiver with an OEM4 board) at NIST were connected to the same antenna [53]. We processed the RINEX data on MJD 53737 and get the measurement difference

(Figures 3.13–3.14) between the two receivers. The measurement difference shows the receiver noise and the cable noise.

We can see that the code measurement has greater noise at a low satellite elevation (Figure 3.13). Since the two receivers are connected to a common antenna, the tropospheric noise, the ionospheric noise and the multipath noise, etc are already cancelled by the measurement differencing. So the greater noise at low satellite elevation in Figure 3.13 can only come from the receiver performance, e.g., the tracking loop performance for weak signals.

As shown in Figure 3.13, the standard deviation (STD) of the PRN04 C1 code measurement difference is 0.53 m. The STD of L1 phase measurement difference is 0.012 cycle (Figure 3.14). If we assume that the two receivers are of the same or similar performance, we get that the code noise due to receiver and cable is $0.53/\sqrt{2} = 0.37$ m, and that the phase noise due to receiver and cable is $0.012/\sqrt{2} = 0.0085$ cycle. The code and phase noise due to the receiver and cable could potentially impact the boundary discontinuity significantly, according to the simulation result in Section 3.1 (see Figures 3.1 –3.2).

3.4.4. Average of Receivers and Boundary Discontinuity

According to the results in Sections 3.4.1–3.4.3, we know that the receiver-related noise is an important contributor to the boundary discontinuity. In order to reduce the impact of the receiver-related noise on the boundary discontinuity, one easy way is to use more GPS receivers with connections to different antennas, to

transfer time. In this way, the receiver-related noise (i.e., multipath, antenna noise, cable noise, and receiver noise) can be averaged down.

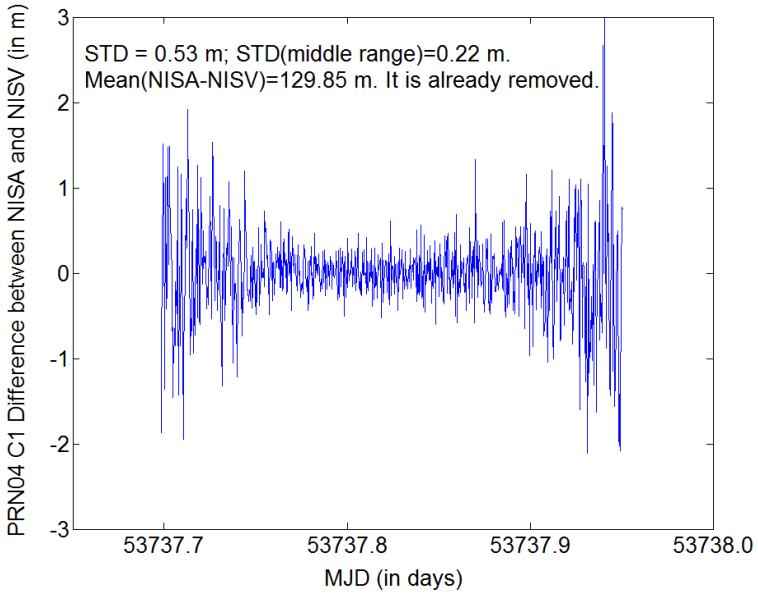

Figure 3.13. C1 pseudorange measurement difference between *NISA* and *NISV* for PRN04 on MJD 53737. The STD of C1 difference is 0.53 m. If we neglect the low elevation part of C1 measurement, the STD becomes around 0.22 m.

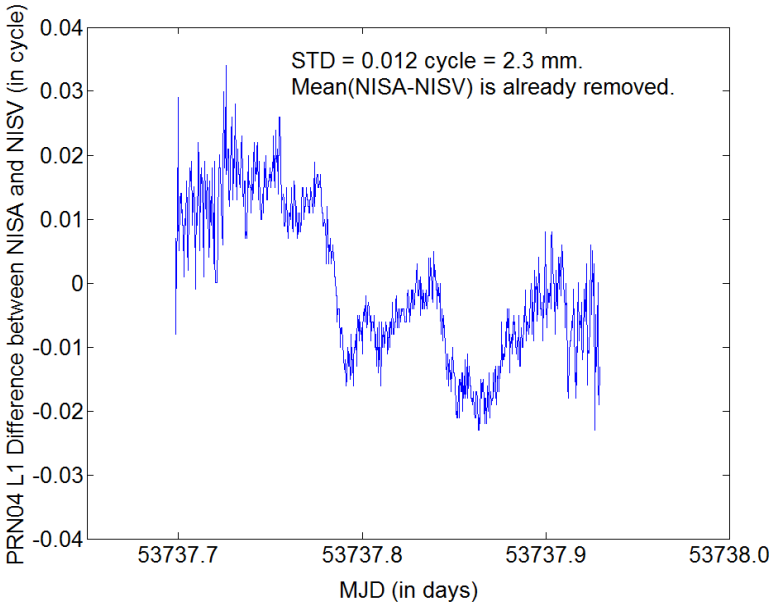

Figure 3.14. L1 phase measurement difference between *NISA* and *NISV* for PRN04 on MJD 53737. The STD of L1 phase difference is 0.012 cycle, which corresponds to 2.3 mm.

For *NISA* at NIST, the STD of the boundary discontinuity jump values is 167.2 ps for MJD 56230–56380. For *NISX* at NIST, the STD is 215.0 ps for the same period. If we do averaging over the two receivers, the STD becomes 124.0 ps, which indicates an improvement of 25.8%. We also do averaging for *SEPA* and *SEPB* at NICT (Japan) for MJD 55927–56077, and *PTBB* and *PTBG* at PTB for MJD 56050–56200. The improvements by averaging two receivers at the same station are 13.7% and 15.9%, respectively (Figure 3.15).

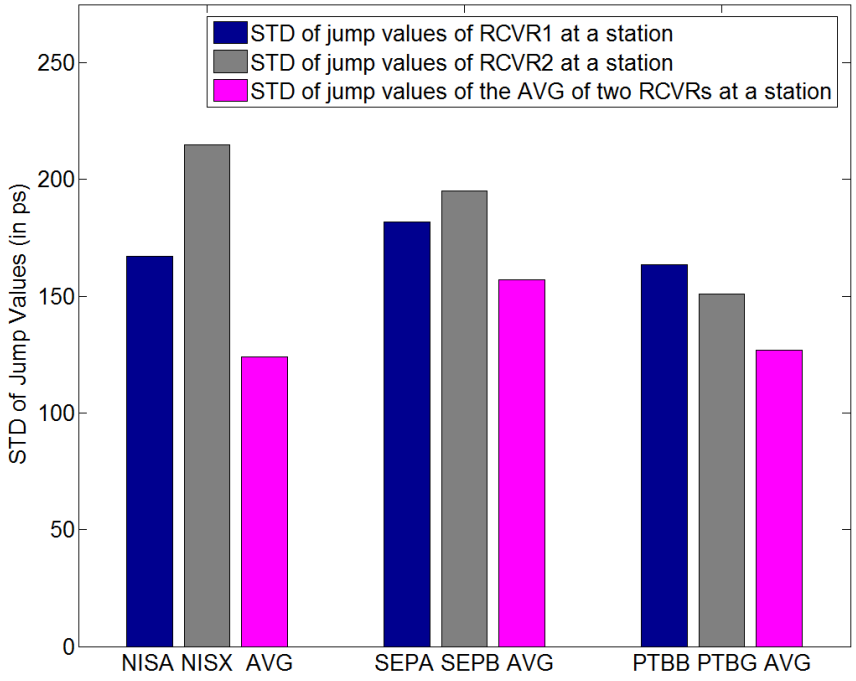

Figure 3.15. Average of receivers and boundary discontinuity for NIST (*NISA* and *NISX*), NICT (*SEPA* and *SEPB*) and PTB (*PTBB* and *PTBG*). The magenta bar is the average of two receivers at a station.

The average of receivers also helps reduce the short-term (< 30 min) noise by 10–20% (Figure 3.16). On the other hand, this also indicates that the conventional

CP time transfer cannot observe the short-term (<30 min) clock noise very well because the actual clock noise cannot be averaged down by using two GPS receivers.

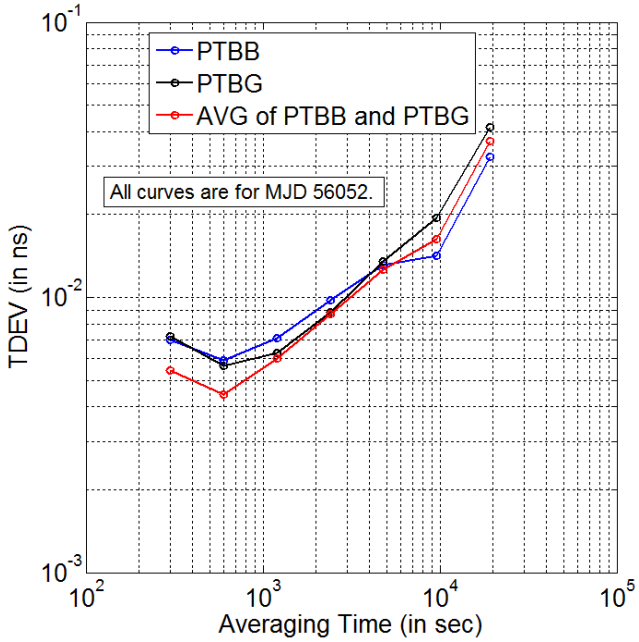

Figure 3.16. Improvement of the average of receivers on the short-term time transfer frequency stability. For the averaging time of 5 min and 10 min, the average of the receivers gives an improvement of 10–20%.

3.5. Bad Points and Boundary Discontinuity

We find that a bad data point (or a data anomaly) in the RINEX file can affect not only the time at that specific epoch, but also the whole time at all epochs and thus the boundary discontinuity, especially when the bad point happens at the beginning or at the end of the data-arc.

For example, we run PPP for *NIST* with the input of the RINEX data-arc from 19:40:00 to 19:39:30 of the next day (e.g., from 19:40:00 of MJD 55647 to 19:39:30 of MJD 55648). The result is shown by the blue curve in Figure 3.17 (blue, red, and

black curves are very close except for the second data-arc in Figure 3.17.). We can see that the boundary discontinuity is obviously below 500 ps. However, if we shift the RINEX data-arc by 5 min (that is, we run PPP for the data-arc from 19:45:00 to 19:44:30 of the next day (red curve in Figure 12)), the boundary discontinuity is now greater than 3 ns. This huge boundary discontinuity comes from the bad point happening at 19:40:00 of MJD 55649. If we remove the two bad PRNs (PRN14 and PRN31) measurements at this epoch, then the huge boundary discontinuity disappears (magenta curve, which is very close to the green curve and the black curve). The black curve shows the case of data-arc of 19:50:00 to 19:49:30 of the next day. The boundary discontinuity of the black curve is again smaller than 500 ps. This example shows that if a bad data point happens at the end of the data-arc, we could have a huge boundary discontinuity.

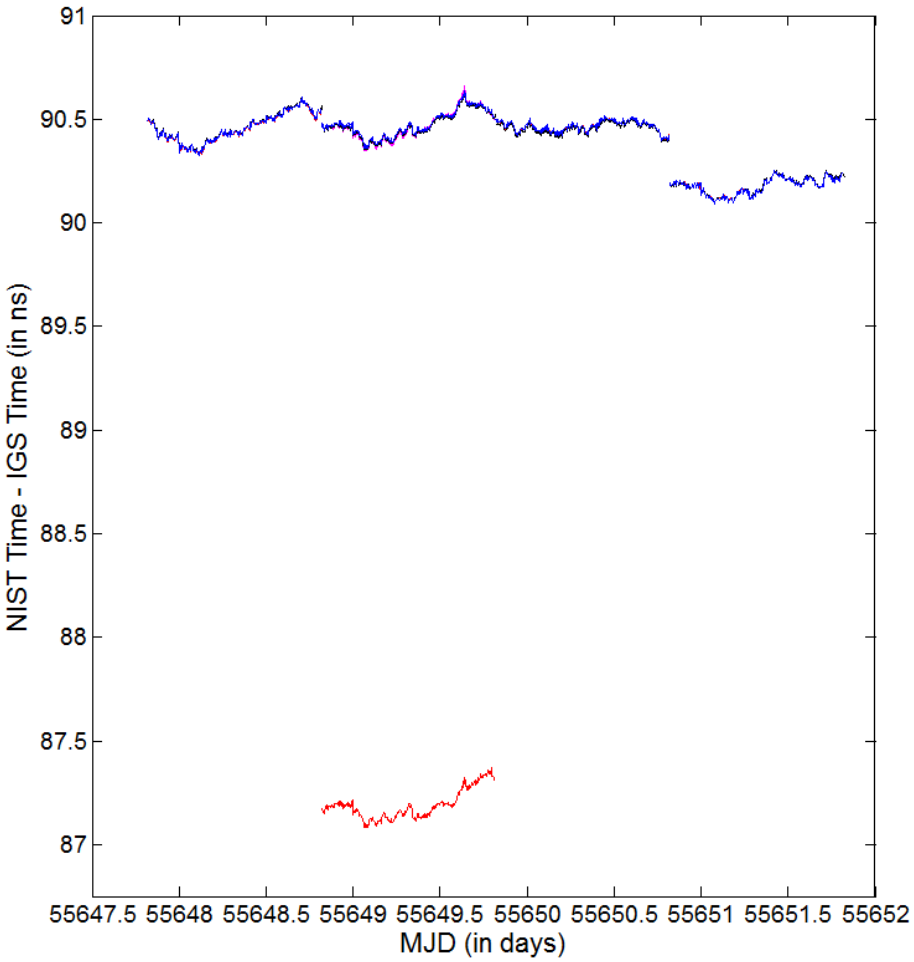

Figure 3.17. Illustration of the impact of a bad data point on the boundary discontinuity. The blue curve is the result for the data-arc of 19:40:00 to 19:39:30 of the next day. The red curve is the result for the data-arc of 19:45:00 to 19:44:30 of the next day. The magenta curve is the corrected result of the red curve on the second data-arc after the bad data are removed. The black curve is the result for the data-arc of 19:50:00 to 19:49:30 of the next day.

Bad points can not only seriously affect the boundary discontinuity as mentioned above, but also damage the whole time transfer result (such as the slope) of a single data-arc. Figure 3.18 shows this problem. We have already detected that there are a few bad points between 15:00:00 and 16:00:00 of MJD 55647 for *USN3* (at USNO, USA). This period (MJD 55647.625–55647.667) is marked by the big

black rectangle in Figure 3.18. At the time around MJD 55646.5, all curves are approximately parallel. That indicates the slope is almost the same no matter how we shift the RINEX data, which is what we expect. The difference between two adjacent curves is around 0.2 ns. The slight difference from 0.2 ns comes from different boundary discontinuities due to shifted data-arcs. The same situation occurs at around MJD 55648.5. However, the slopes of all curves are not the same around MJD 55647.5 because of the bad points happening from 15:00:00 to 16:00:00 on this day. For example, at MJD 55647.60, the bottom black curve reads 7.685 ns. The bottom red curve almost reads the same value as the bottom black curve. At MJD 55647.75, the bottom red curve reads 7.817 ns. However, the bottom black curve reads 7.607 ns. The slope difference between the two curves during MJD 55647.60–55647.75 is as big as 1.4 ns / day. Remember that we use exactly the same RINEX data and run PPP with exactly the same settings. The only difference is that we shift the RINEX data by a few hours. In principle, the slope difference of two curves should be very close to 0. Because of the existence of bad points, we have totally different time transfer results. These different results make us hard to tell which one is correct or whether both of them are wrong. This example demonstrates how seriously a few bad points can damage the whole time transfer result of a single data-arc.

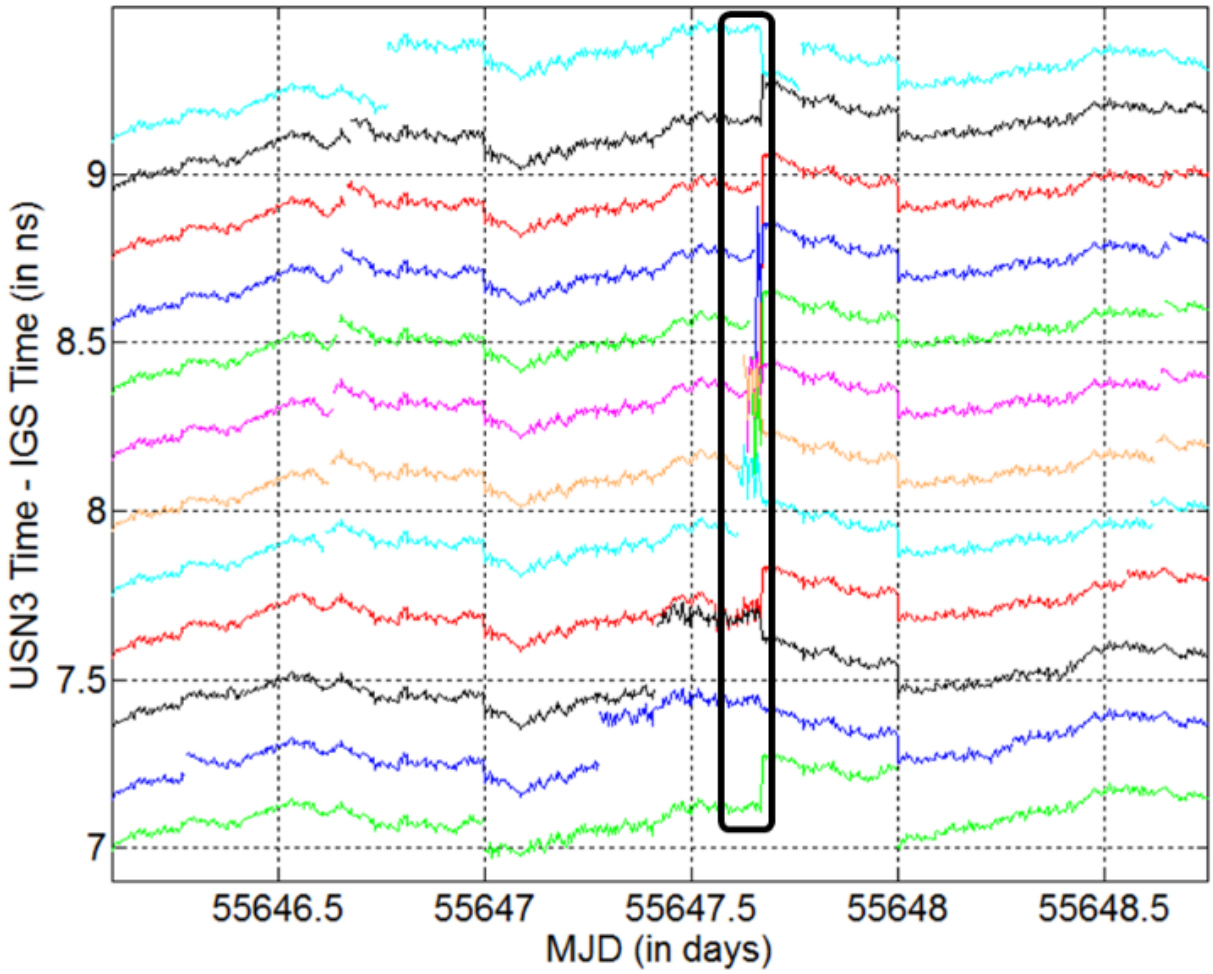

Figure 3.18. Illustration of how bad points damage the time transfer result of the same data-arc. The curves are shifted along the y-axis by multiples of 0.2 ns for better comparison. Each curve begins at a different start point (e.g., the magenta curve begins at 15:15:00; the bottom green curve begins at 00:00:00).

3.6. PPP Method and Network Method on Boundary Discontinuity

As mentioned in Section 1.5.2, there are two implementation methods of GPS carrier-phase time transfer: the network method and the PPP method. The PPP method is easier to implement and faster than the network method. However, the result of the PPP method may not be as good as that of the network method. This

occurs because it does not solve all equations from all stations in the world together. Thus, there could potentially have a small timing and positioning bias in the result of the PPP method. Such a bias may lead to a bigger boundary discontinuity. Thus, we want to compare the two methods in terms of the boundary discontinuity.

Actually, the IGS clock file has already provided the results of the network method for many ground stations. Figure 3.19 shows the comparison between the PPP method and the network method. We can see that the mean jump value is closer to 0 in the network method than the PPP method. Furthermore, the STD is typically more than 20 ps in the network method than in the PPP method. This means that the network method is superior to the PPP method in terms of boundary discontinuity. Any improvement in the algorithm for implementing the GPS carrier-phase time transfer can give a smaller discontinuity, even though the noise in physical measurement is still the same.

3.7. Summary

In this chapter, we find that the code noise is the major contributor to the boundary discontinuity. The code noise can be divided into three categories: satellite-related noise, path-related noise, and receiver-related noise. We find that by using the IGS 30-sec clock product, the boundary discontinuity can be lowered by 10–30%. The tropospheric path noise seems have little impact on the boundary discontinuity. The boundary discontinuity can be further lowered by 10–20% if a few GPS receivers at the same station are averaged. The anomaly in the RINEX

data can also sometimes lead to a big boundary discontinuity and an incorrect slope in the time transfer. The comparison between the PPP method and the network method indicates that the network method provides a smaller boundary discontinuity.

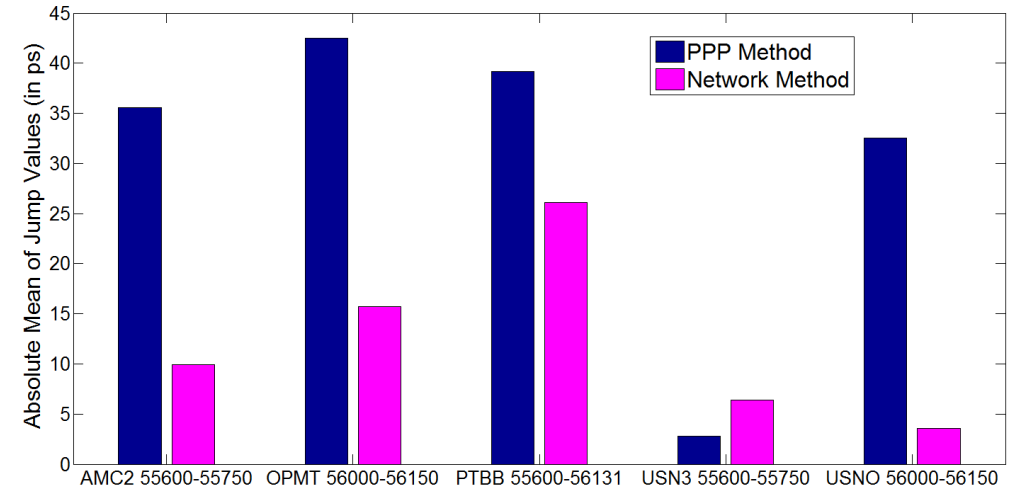

(a)

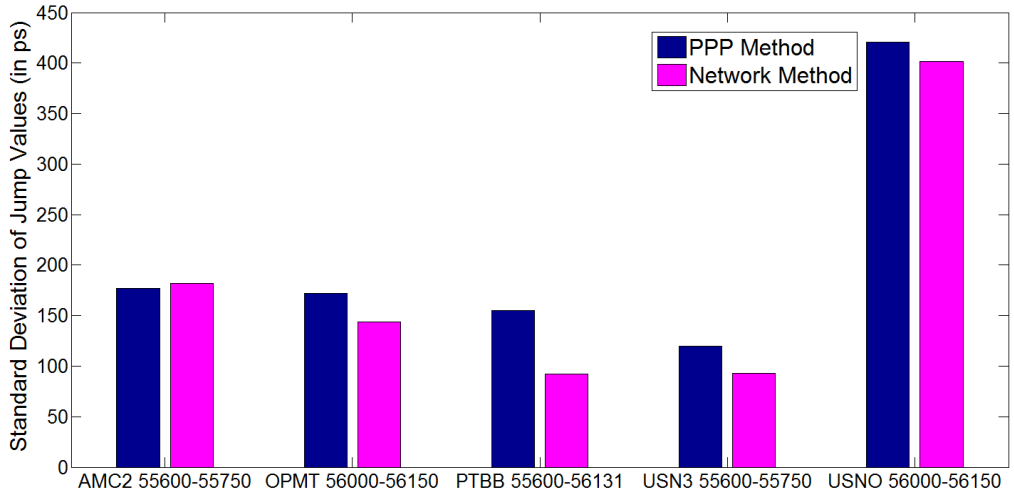

(b)

Figure 3.19. Effect of algorithms of fixing ambiguity on boundary discontinuity. (a) shows the absolute mean of discontinuity of both the PPP method and the network method for five stations. (b) shows the STD of discontinuity.

Chapter 4

Eliminating Day Boundary Discontinuity: RINEX-Shift algorithm[1]

4.1 RINEX-Shift Algorithm

As we discussed in the last chapter, the day boundary discontinuity comes from any type of code noise. Although the code noise can be reduced by some methods, it is impossible to get it down to zero. Thus, the boundary discontinuity cannot be removed by reducing the code noise. However, this does not mean that there is no way to eliminate the boundary discontinuity. In fact, a few algorithms have been proposed to eliminate the boundary discontinuity to achieve continuous GPS CP time transfer [43, 46–47, 54–57]. One promising algorithm among them is the RINEX-Shift (RS) algorithm [47, 54].

Figure 4.1 shows how the RS algorithm works. The conventional PPP runs first forward (from the beginning of the data-arc to the end of the data-arc) and then backward (from the end of the data-arc to the beginning of the data-arc) in order to converge the solutions [38]. The backward results (one point per 5 min) form the final PPP output. As shown in Figure 4.1(a), the blue dots and the red dot together

[1] The results of this chapter are mainly based on [47, 54].

are the backward results of PPP. Since the phase ambiguity is almost always away from the true value due to the code noise, the solution of one data-arc almost always has a jump from the solution of the next data-arc. This jump is the boundary discontinuity.

A good way to "eliminate" the boundary discontinuity is to make the length of the data-arc to be 5 min so that every point has its own estimation of phase ambiguity. Now the boundary discontinuity is actually transformed from a long data-arc (≥ 1 day) to a short data-arc (e.g., 5 min). The boundary discontinuity of a short data-arc cannot be noticed because it is combined with the short-term (e.g., 5 min) noise. In this way, we no longer have the boundary discontinuity, and the carrier-phase (CP) time transfer can be used for a long-term (e.g., 20 days) time comparison without the impact of the day boundary discontinuity.

Another thing to consider is that the use of a short data-arc can hardly give a converged estimate of the zenith path delay of the troposphere, etc. Thus, the short-term noise can be huge because of a large uncertainty in the phase ambiguity. A good way to tackle this issue is to run PPP for a long data-arc and extract the result at the first epoch point of the backward process [the red dot in Figure 4.1(a)]. Then we shift the RINEX data by another time step (e.g., 5 min, or 10 min, or even greater) and executes PPP, and then extracts the result at the new first epoch again [Figure 4.1(b)]. So on and so forth [Figure 4.1(c)-(d)]. The results at all the first epochs [the red dots in Figure 4.1(a)-(d)] form the final result. In this way, we can

not only eliminate the boundary discontinuity, but also have small short-term noise. We call this process the RINEX-Shift (RS) algorithm.

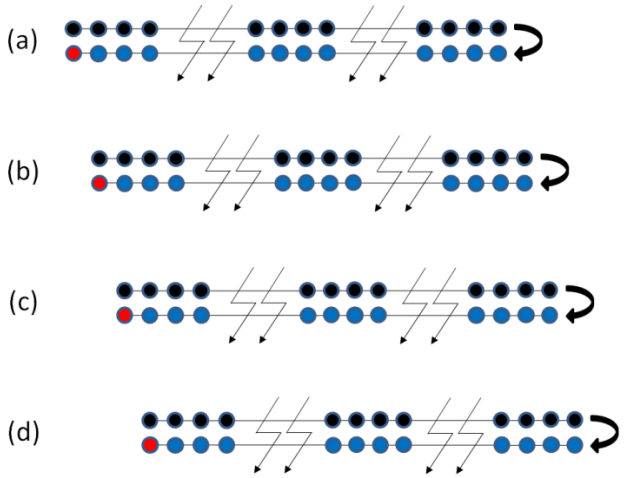

Figure 4.1. Illustration of the RINEX-Shift algorithm.

To test this algorithm, we choose the "*NIST*" receiver at NIST and the "*PTBB*" receiver at PTB (Physikalisch-Technische Bundesanstalt, Germany). We set the data-arc of the RS algorithm to 10 days and the time step to 10 min. Then we run the RS algorithm and get the time difference between the *NIST* time and the *PTBB* time during Modified Julian Date (MJD) 56389–56409 (red curve in Figure 4.2). The black curve in Figure 4.2 is the result of the conventional PPP with a 1-day data-arc, as a reference. As we can see, there are day boundary discontinuities in the black curve. These discontinuities disappear in the red curve. This indicates that the RS algorithm eliminates day boundary discontinuities successfully.

The modified total deviation (MTD) is used to characterize the frequency stability. Figure 4.3 shows the MTD of the black and red curves in Figure 4.2. The RS algorithm reduces the time-transfer noise significantly, especially at the range

of 4 hours to 4 days. The MTD of the RS result (red curve in Figure 4.3) becomes flat for an averaging time of greater than 1 day, which indicates that we have already seen the UTC(k) clock noise after 1 day.

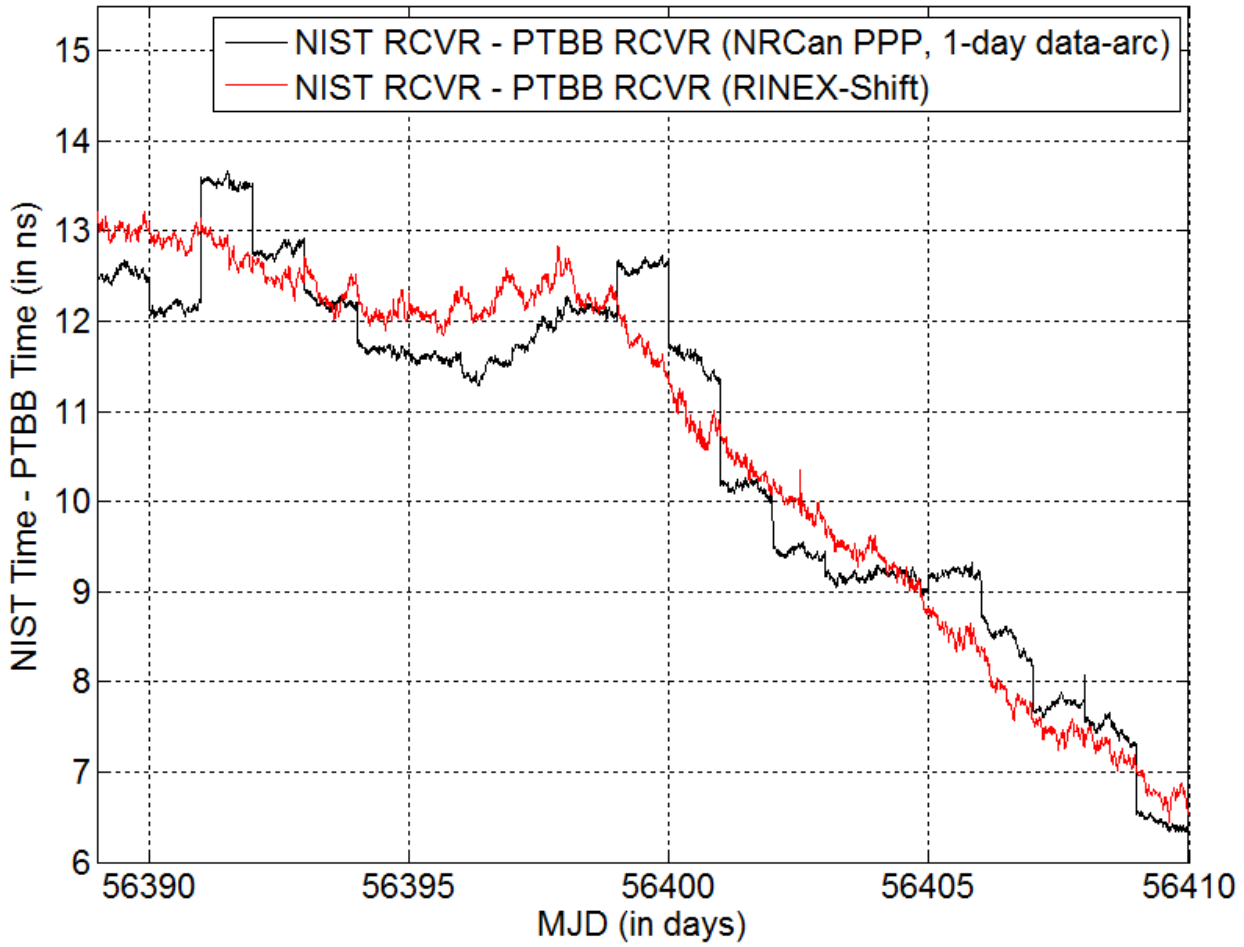

Figure 4.2. Time comparison between *NIST* and *PTBB* during MJD 56389–56409 by NRCan PPP (black curve) and the RINEX-Shift (RS) algorithm (red curve). The curves are shifted to overlay each other for better comparison.

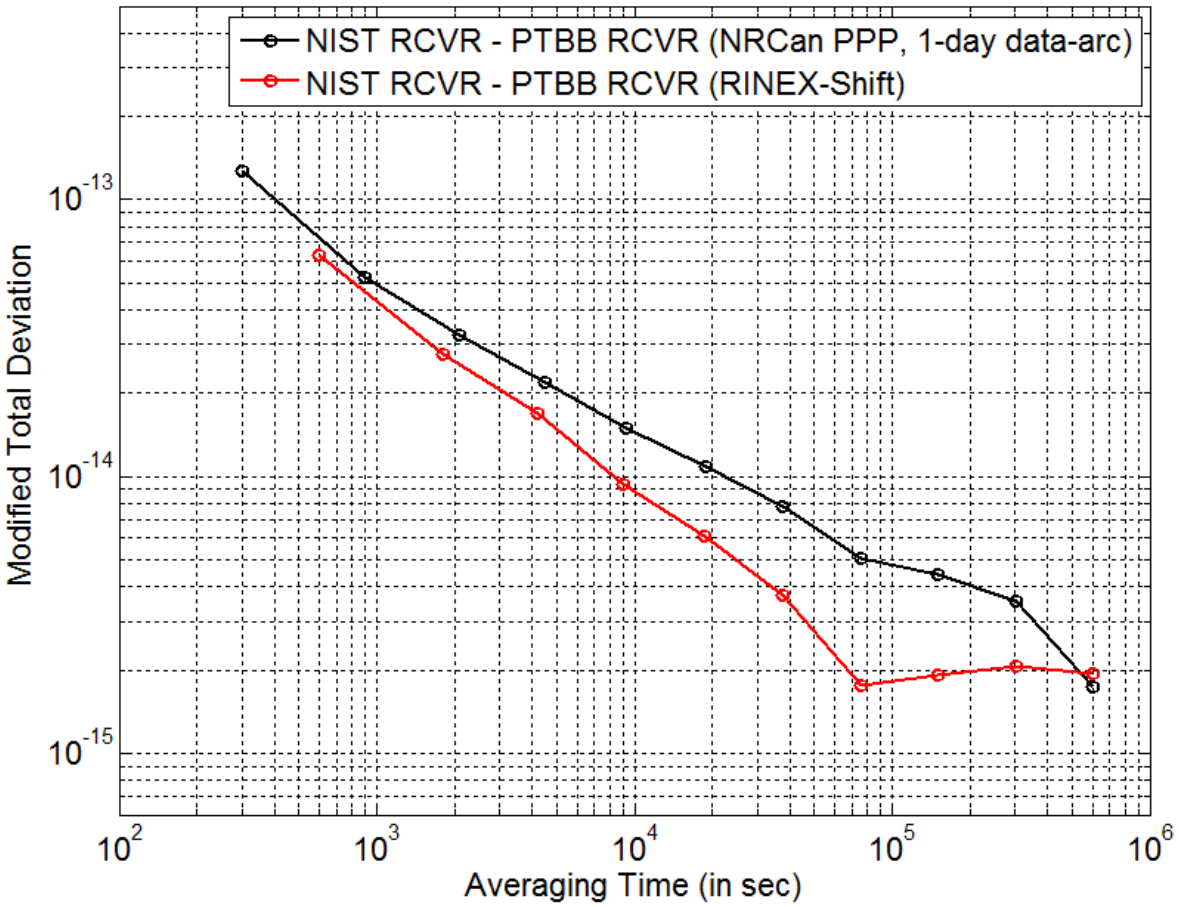

Figure 4.3. MTD of the time difference between *NIST* and *PTBB* for MJD 56389–56409, using NRCan PPP (black curve) and the RINEX-Shift (RS) algorithm (red curve).

4.2 Problem with RINEX-Shift Algorithm

The RS algorithm showed excellent performance in terms of eliminating the boundary discontinuity as shown in Section 4.1. However, this excellent performance is only the case when all of the GPS data are good. Although most timing laboratories have installed state-of-the-art GPS receivers and antennas, it is still inevitable that a GPS receiver malfunctions (e.g., losing track of GPS

satellites), or the satellite-receiver line is blocked by an object, or the reference time for the receiver is adjusted, or even a man-made error occurs. All these problems lead to GPS data anomalies. We find that if there are a few epochs of data anomalies, the result of the RS algorithm deviates from the true value (Figures 4.4–4.5).

In Figure 4.4, we compare the time difference between *PTBB* [a GPS receiver in PTB, Germany] and the International GNSS Service (IGS) final time. The black curve is the result of the NRCan PPP software package. We can see that there is an obvious day boundary discontinuity between MJD 56610 and MJD 56611. Since the standard deviation of the boundary discontinuity of PTBB is only 138.5 ps [18], we can hardly distinguish other small day boundary discontinuities at the scale of Figure 4.4. The red curve is the result computed by the RS algorithm. It eliminates the boundary discontinuity very well (e.g., there is no jump between MJD 56610 and MJD 56611).

(a)

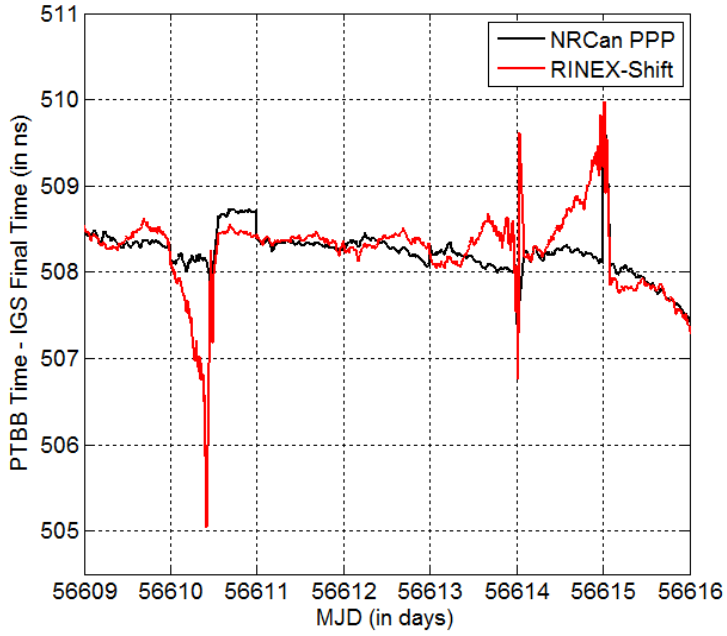

(b)

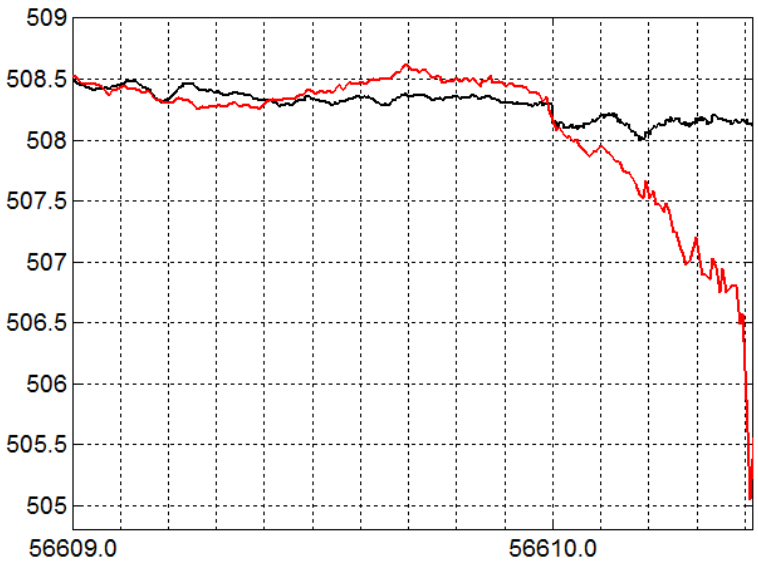

Figure 4.4. Comparison of NRCan PPP (black curve) and the RINEX-Shift algorithm (red curve) at anomalies at PTB. (b) is enlarged from (a).

However, the RINEX data of *PTBB* show that there are three time periods of missing GPS data during MJD 56609.0–56616.0. The first one occurs between

10:00:00 and 10:49:30 on MJD 56610, the second one 01:00:00–01:59:30 on MJD 56614, and the third one 01:00:00–01:59:30 on MJD 56615. The red curve in Figure 4.4(a) shows bad time transfer results of the RS algorithm whenever the missing data occur. The deviation from the NRCan PPP result can be as large as 3 ns. As an example, at 9:50:00 on MJD 56610 (i.e., MJD 56610.410), the red curve reads 505.049 ns, while the black curve reads 508.140 ns [see Figure 4.4(b)]. This discrepancy indicates an error of 3.091 ns in the RS algorithm. Besides, the large deviation occurs only on the left side of the bad epochs. As the time gets away from the bad epochs, the difference between the two curves shows a damped oscillation. For example, from MJD 56610.4 to 56610.0, the difference between the two curves decreases quickly. At MJD 56610.0, the difference is almost 0. Then from MJD 56610.0 to 56609.7, it increases to about 0.25 ns, and again decreases to 0 at MJD 56609.4. For the epochs before MJD 56609.4, the red curve becomes very close to the black curve. This indicates that after about 1 day, the damped oscillation due to a data anomaly in the RS algorithm becomes negligible. Analyzing the two curves from MJD 56612.0–56614.1 and from MJD 56614.1–56615.0 also shows that the damped oscillation almost disappears after approximately a 1-day decay.

Figure 4.5 provides another example. The reference time for the *NIST* receiver was adjusted by approximately +23 ns around MJD 56646, and thus it leads to a GPS-data anomaly. In addition, no data were recorded during 18:22:00–18:28:30 on MJD 56647, and thus another anomaly occured. These two anomalies both result in

damped oscillations in the RS algorithm (red curve). Again, the oscillation is negligible after about a 1-day decay.

From the above analysis, the RS algorithm suffers from a damped oscillation with a maximum amplitude of a few nanoseconds, for the epochs before an anomaly. It takes 1 day for the oscillation to decay to a negligible value. In the next section, we will introduce the "isolated island effect" and then explore the mechanism of the damped oscillation in the result of the RS algorithm in Section 4.4.

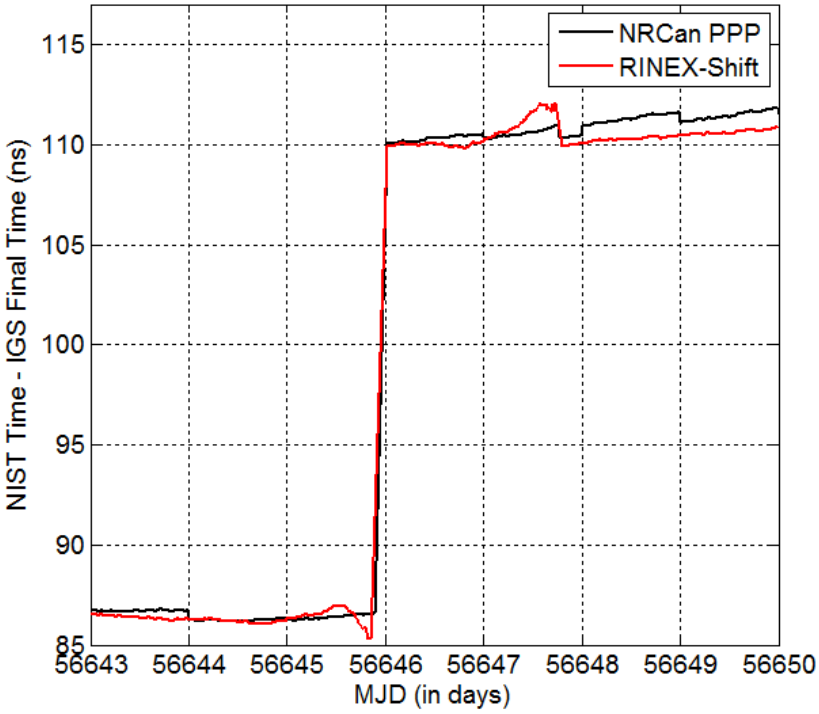

Figure 4.5. Comparison of NRCan PPP (black curve) and the RINEX-Shift algorithm (red curve) at anomalies at NIST.

4.3 Isolated Island Effect

The PPP method must estimate phase ambiguities for each GPS data-arc. If there are a few minutes of data anomaly, the data-arc is split into two pieces: the

first sub-data-arc and the second sub-data-arc. PPP typically treats the second sub-data-arc (i.e., the data after the anomaly) as a new data-arc and thus re-estimates phase ambiguities that are usually different from the estimations for the first sub-data-arc. Because of different phase-ambiguity estimations for the first and second sub-data-arcs, we have a boundary discontinuity at the anomaly (Figure 4.6).

The blue curve in Figure 4.6 shows the PPP result for the original RINEX data of *PTBB* on MJD 56489. It is continuous because there is no anomaly. However, if we delete 10 minutes of RINEX data, e.g., 13:00:30–13:10:00, then the PPP result has a boundary discontinuity of 1.07 ns at 13:00:00 (red curve). If the 10-min missing-data window occurs at other epochs (grey, orange, black, green, and magenta curves), we still have a boundary discontinuity, although the jump value varies. This illustrates that an anomaly leads to a boundary discontinuity. Note that the slopes of all curves are more or less the same. Thus, an anomaly is not too bad, if only frequency transfer, instead of time transfer, is our main concern.

However, the above analysis is based on the premise that an anomaly occurs in the middle range of a data-arc. If an anomaly occurs at the beginning or the end of a data-arc, the behavior of the PPP result becomes quite different.

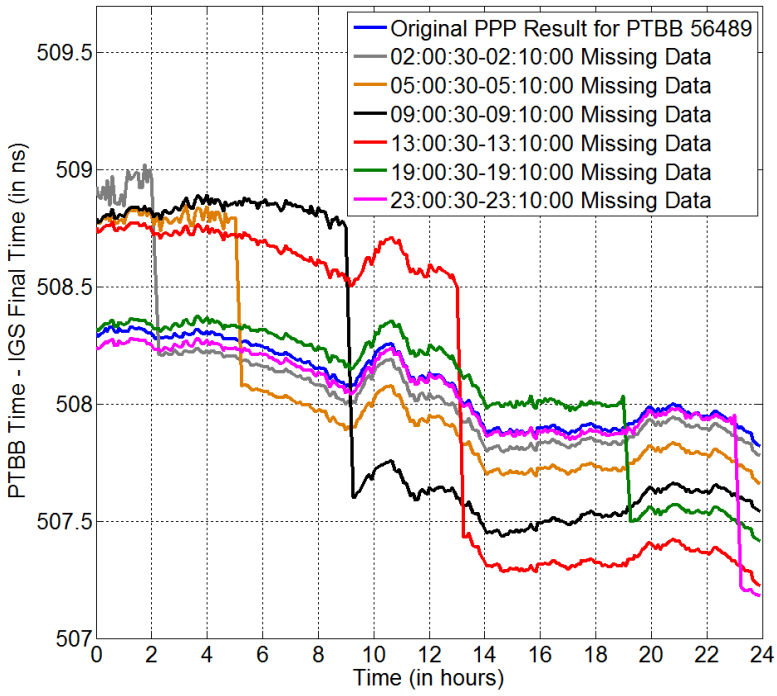

Figure 4.6. Anomaly in the middle range of the data-arc and boundary discontinuity. The blue curve is the original PPP result for *PTBB* on MJD 56489. All other curves are the PPP results with 10-min missing data.

Figure 4.7 shows the PPP results when the 10-min missing-data window is close to the beginning of a data-arc. The blue curve is the PPP result of the original RINEX data, for reference. If the missing-data window occurs at 00:00:30–00:10:00 (that means that 00:00:00 is the only epoch of valid data before the anomaly since the GPS receivers record RINEX data every 30 s.), the time transfer error can be as large as 1.7 ns (solid red curve at 00:00:00). This is because the phase ambiguity cannot be solved for if only one epoch of measurements is provided [19, Chapter 6]. This makes the phase measurements useless. Thus, the time solution at 00:00:00 can only be determined by the code measurements, which are much noisier than the phase measurements. As the missing-data window shifts away from the data-arc

edge (e.g., the dashed red curve), we have a longer period of valid data (in this case, it is 30 min) between the edge and the anomaly. Therefore, we are now getting a better estimation of the phase ambiguities. However, this estimation is still not good enough. Reference [38] tells us that the PPP program requires at least 1 hour of data to converge to an accurate estimation of phase ambiguities. 30 min is still not sufficient for PPP to converge to a reasonable result, which makes the dashed red curve still quite noisy during the first sub-data-arc. When the missing-data window occurs more than 1 hour away from the edge (e.g., the dashed green curve in Figure 4.7), the PPP result for the first sub-data-arc becomes smooth.

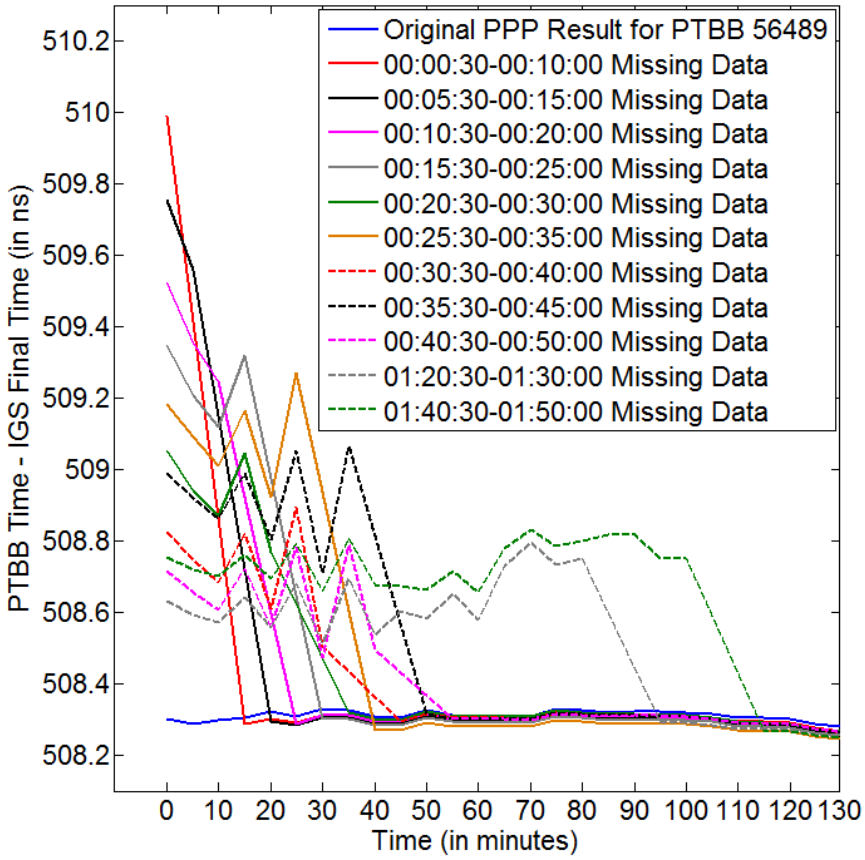

Figure 4.7. Anomaly at the beginning of the data-arc and boundary discontinuity. The blue curve is the original PPP result for *PTBB* on MJD 56489. All other curves are the PPP results with 10-min of missing data.

From the above analysis, we know that an anomaly in the middle range of a data-arc results in a boundary discontinuity, but the time-transfer slope is almost unchanged; an anomaly at the edge of a data-arc (less than 1 hour from the edge) results in a completely damaged PPP result between the anomaly and the edge. We call this phenomenon the "isolated island effect."

4.4 Mechanism of Damped Oscillation in the RINEX-Shift Algorithm

In the RS algorithm, we run PPP for a data-arc of 10 days and extract the PPP result at the first epoch (here, we define the PPP result at the first epoch as "*PPP_FE*"). If the anomaly is more than 10 days away from the first epoch, it does not affect the result of the RS algorithm. However, as we shift the RINEX data step by step, the new data-arc starts to cover the anomaly. The anomaly first shows at the end of the data-arc, and thus the length of the first sub-data-arc is 10 days (here, we define the length of the first sub-data-arc, i.e., the time difference between the anomaly and the first epoch, as *deltaT*). Then the RINEX data continue shifting and *deltaT* changes from 10 days to 0. At the same time, all *PPP_FE*s are extracted to form the RS solution. In the end, the data-arc goes over the anomaly (i.e., *deltaT* becomes negative), and thus the anomaly no longer affects the result of the RS algorithm. From the above, we can see that the RS solution after the anomaly is not affected by the anomaly, but the RS solution before the anomaly is determined by the relationship between *PPP_FE* and *deltaT*. Thus, we next study this relationship.

Actually, we have already had the "*PPP_FE–deltaT*" relationship if we interpret Figures 4.6–4.7 in a different perspective. For the grey curve in Figure 4.6, the length of the first sub-data-arc "*deltaT*" is 2 hours, and the PPP result at the first epoch (i.e., 00:00:00) is 508.926 ns, which is +0.624 ns away from the original PPP result (blue curve in Figure 4.6) at 00:00:00. Thus, we have (*deltaT*, *PPP_FE*) = (2.008 hours, 508.926 ns). Similarly, for the orange curve in Figure 4.6, we have (*deltaT*, *PPP_FE*) = (5.008 hours, 508.794 ns). So on and so forth. This gives a series of (*deltaT*, *PPP_FE*) pairs. The red curve in Figure 4.8 shows the result (note, it uses some curves not shown in Figures 4.6–4.7). The original PPP result at 00:00:00 is given for reference (blue curve).

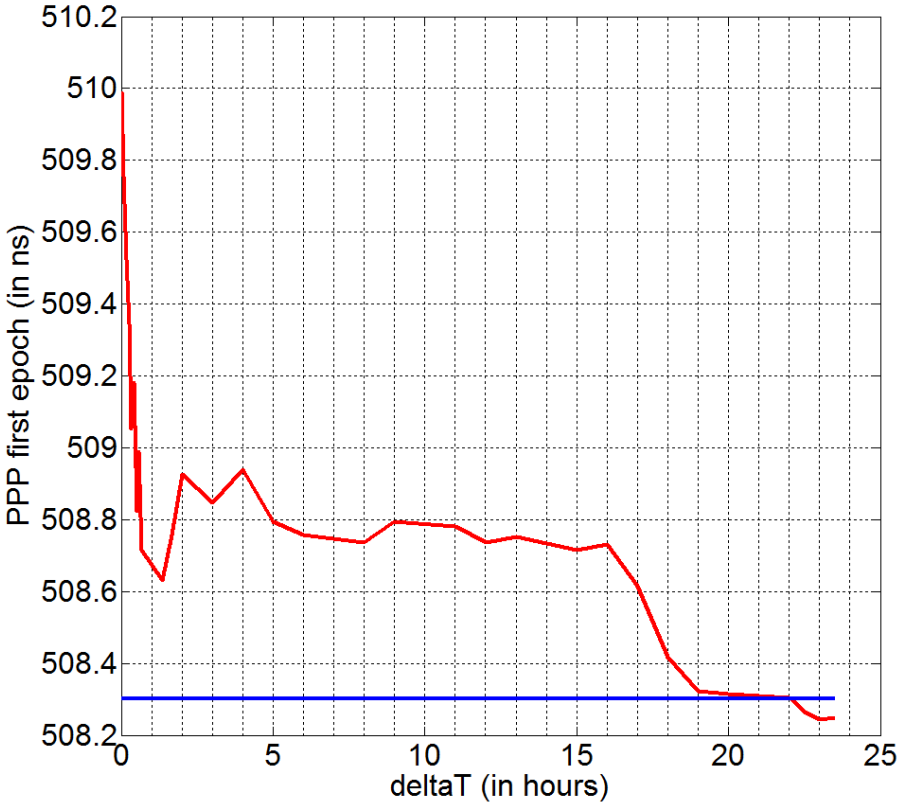

Figure 4.8. *PPP_FE–deltaT* graph. The *PPP_FE–deltaT* relationship determines the RS solution before the anomaly.

We can see that Figure 4.8 and Figure 4.4(b) have many common features, demonstrating that the "*PPP_FE*–deltaT" relationship does determine the result of the RS algorithm. First, in Figure 4.8, we can clearly see that *PPP_FE* (red curve) is approximately 1.7 ns away from the original PPP result (blue curve) when *deltaT* is close to 0. This indicates that the error in the RS algorithm can be as large as several nanoseconds when the anomaly is very close to the first epoch. This matches our results in Figure 4.4(b). Second, when *deltaT* increases from 0 to 40 min, *PPP_FE* decays toward the original PPP result very quickly (Figure 4.8). This decay is very similar to the behavior of the RS solution during MJD 56610.375–56610.403 [red curve in Figure 4.4(b)]. Third, for the range of 2 hours to a few hours, Figure 4.8 shows that *PPP_FE* decreases slowly and steadily toward the original PPP result, which is again quite similar to the RS solution for the time range of 56610.05–56610.33 in Figure 4.4(b). Finally, when *deltaT* is more than 20 hours, *PPP_FE* becomes smaller than the original PPP result (Figure 4.8). But the absolute maximum difference between *PPP_FE* and the original PPP result is only about 0.059 ns, which is much smaller than if *deltaT* is in the range of 2 hours to a few hours. This indicates a damped oscillation in *PPP_FE*. Again, the behavior of *PPP_FE* at *deltaT* > 20 hours matches the damped oscillation behavior in the result of the RINEX-Shift algorithm (Figure 4.4(b)).

The above analysis shows that the *PPP_FE–deltaT* relationship does determine the RS result. Because the *PPP_FE–deltaT* relationship is derived from the isolated island effect, we conclude that it is the isolated island effect that leads

to the damped oscillation behavior in the RS algorithm. In addition, the scope of the isolated island effect is approximately 1 day. Once a sub-data-arc is longer than 1 day, the impact of the isolated island effect on the RS algorithm is negligible.

4.5 Revised RINEX-Shift Algorithm

Based on the discussion in Sections 4.2–4.4, we know that if an anomaly is less than 1 day away from the edge of a data-arc (i.e., $deltaT < 1$ day), the time-transfer result of the RS algorithm in between is incorrect, because of the isolated island effect. If $deltaT > 1$ day, the result in between becomes reasonable. Thus we must avoid the situation when the anomaly is less than 1 day away from the data-arc edge. If we can achieve this, we can solve the damped oscillation problem in the RS algorithm. One good way is to extract the PPP result at the middle epoch of the data-arc, instead of the first epoch of the data-arc as in the RS algorithm. We call this the "revised RINEX-Shift (RRS)" algorithm. The following example explains how this algorithm works.

In Figure 4.4, there is an anomaly occurring at 01:00:00 on MJD 56614 (i.e., 56614.042). When we run PPP for the data-arc of MJD 56604.044–56614.044, the anomaly starts to affect the time-transfer result. We know that the result of the second sub-data-arc (i.e., 56614.043–56614.044) is completely damaged because the length of this sub-data-arc is too short for PPP to converge. However, the result of the first sub-data-arc (i.e., 56604.044–56614.041) is still good because the length of this sub-data-arc is greater than 1 day, and the isolated island effect is negligible. If

the RRS algorithm is applied, the PPP result at the middle epoch (i.e., 56609.044) is extracted. Since the middle epoch is within the first sub-data-arc, the PPP result at this epoch is good. As we continue shifting the data-arc until 56609.040–56619.040, the first sub-data-arc changes from 56604.044–56614.041 to 56609.040–56614.041. When the data-arc is 56609.040–56619.040, the length of the first sub-data-arc is 5.001 days, which is still long enough to make the isolated island effect negligible. Thus, the result at the middle epoch (i.e., 56614.040) extracted by the RRS algorithm is still good. Next, the data-arc shifts to 56609.043–56619.043. Now the PPP result at 56614.043 is extracted. This epoch is within the second sub-data-arc (i.e., 56614.042–56619.043). Since the second sub-data-arc is again longer than 1 day, the PPP result at 56614.043 is still good.

From the above example, we can see that once we extract the middle epoch of the data-arc, the sub-data-arc where the middle epoch lies is always longer than 5 days, which is long enough to eliminate the impact of the isolated island effect. Thus, the RRS algorithm should provide reasonable results at all epochs. We report tests of its performance in the next section.

4.6 Performance of Revised RINEX-Shift Algorithm

In this section, we first test the performance of the RRS algorithm when there is an anomaly in the RINEX data. Figures 4.9–4.10 show the results of the RRS algorithm for the same periods as Figures 4.4–4.5. Similar to NRCan PPP (black curve) and the RS algorithm (red curve), the revised RINEX-Shift algorithm (blue

curve) has a boundary discontinuity at the anomaly (e.g., MJD 56610.417). This discontinuity occurs because the epochs before and after the anomaly belong to two different sub-data-arcs, and thus different phase ambiguities are estimated. Like the RS algorithm, the RRS algorithm eliminates the day boundary discontinuities successfully. Most importantly, as compared to the RS algorithm, there is no damped oscillation problem in the RRS algorithm.

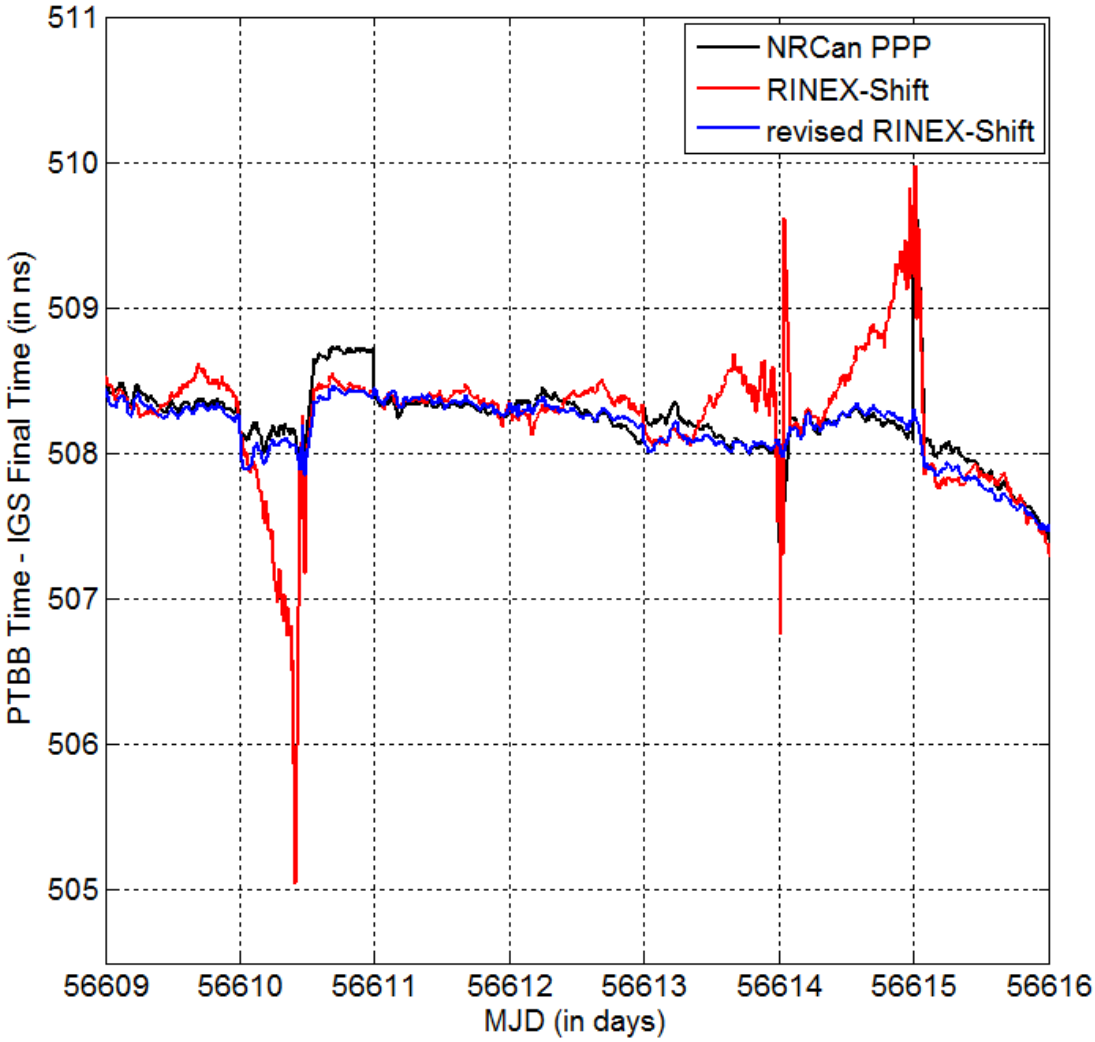

Figure 4.9. Comparison of NRCan PPP (black curve), RS algorithm (red curve) and RRS algorithm (blue curve) at anomalies at PTB.

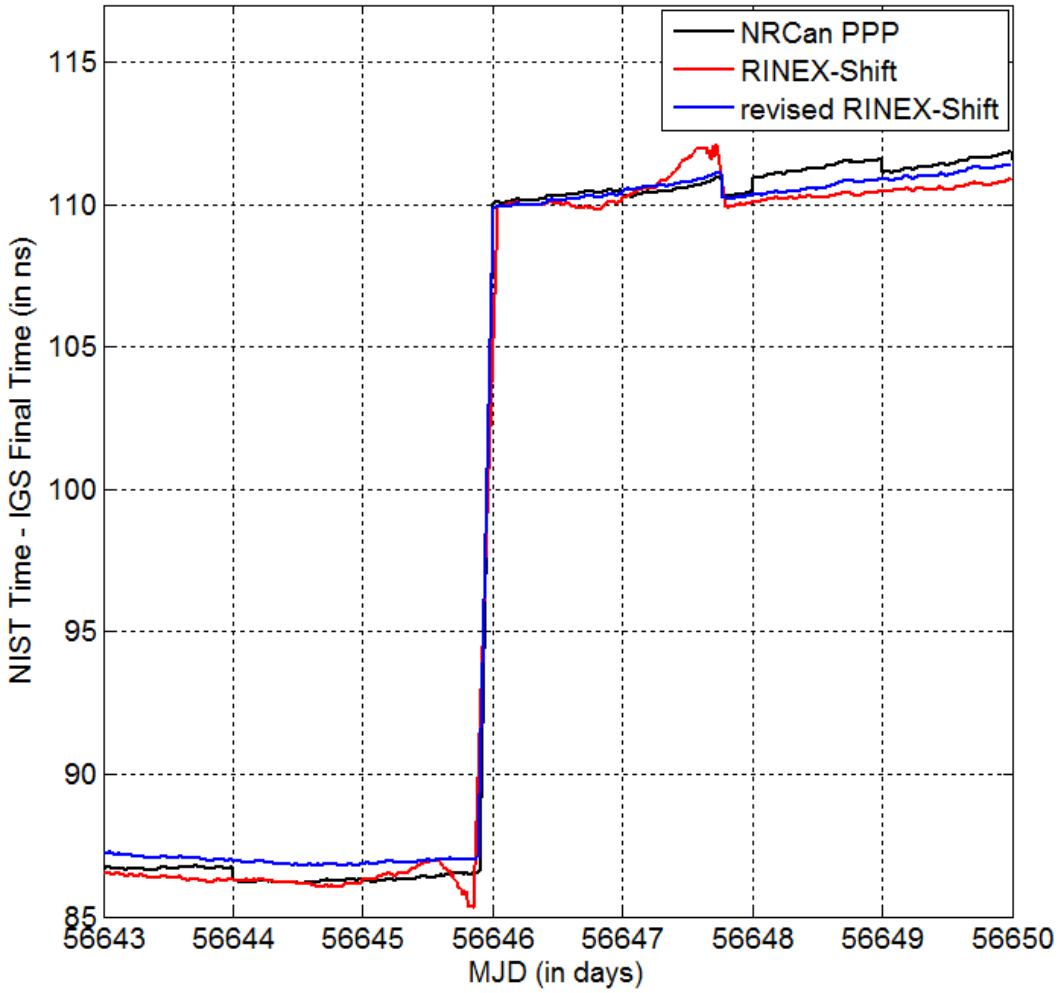

Figure 4.10. Comparison of NRCan PPP (black curve), RS algorithm (red curve) and RRS algorithm (blue curve) at anomalies at NIST.

Next, we test the performance of the RRS algorithm when the RINEX data are all good (e.g., MJD 56389–56409). Here, we use IGS 30-sec clock products, instead of IGS 5-min clock products, as the input of the RRS algorithm, because Section 3.2 shows that the time-transfer results using IGS 30-sec clock products as the input are closer to the true values than if using IGS 5-min clock products. In Figure 4.11, we do a time comparison between the *NIST* receiver and the *PTBB* receiver for

MJD 56389–56409 by NRCan PPP (black curve), RS algorithm (red curve), and RRS algorithm (blue curve). We can see that both RS and RRS provide continuous time-transfer results. The modified total deviation (MTD) is used to characterize the frequency stability of the three time-transfer methods (Figure 4.12). Obviously, the RRS algorithm provides the best frequency stability. It reduces the time-transfer noise of the RS algorithm by 10–55%. The most significant improvement of the RRS algorithm over the RS algorithm occurs at the averaging time of 1–4 days. For an averaging time of 1.75 days, the frequency stability of the RRS algorithm is only 8.6 $\times 10^{-16}$, which makes it the best GPS time-transfer result. In addition, the MTD of the RRS algorithm increases for an averaging time of greater than 1.75 days, which indicates that we have already seen the clock noise after 1.75 days.

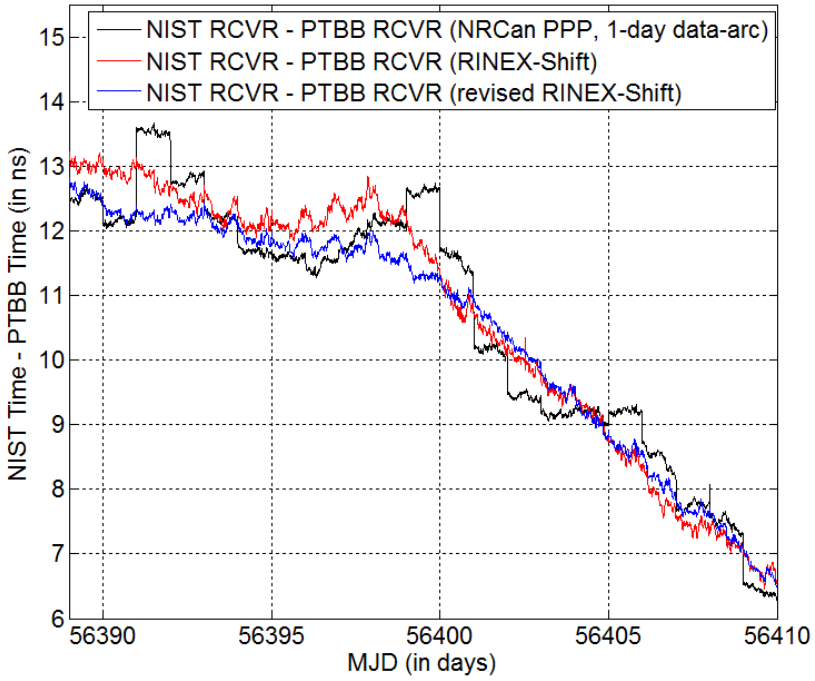

Figure 4.11. Time comparison between *NIST* and *PTBB* during MJD 56389–56409 by NRCan PPP (black curve), RS algorithm (red curve), and RRS algorithm (blue curve). The curves are shifted to overlay each other for better comparison.

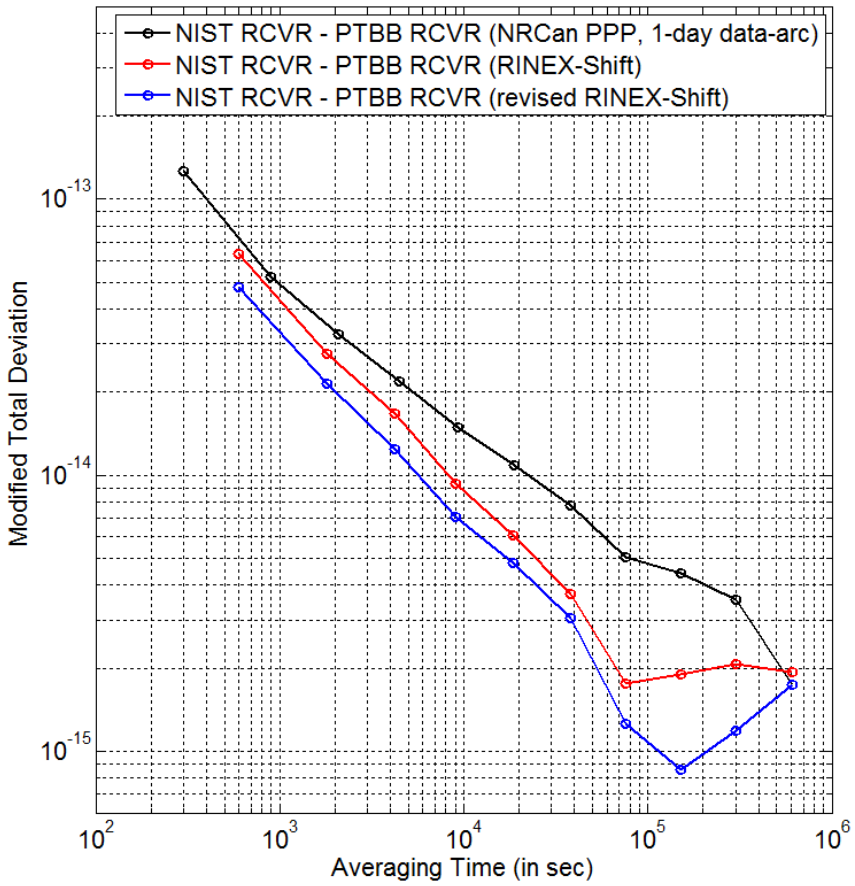

Figure 4.12. MTD of the time difference between *NIST* and *PTBB* for MJD 56389–56409 using NRCan PPP (black curve), RS algorithm (red curve), and RRS algorithm (blue curve).

As stated in [56], the smoothest time-transfer solution is not necessarily the most accurate solution. The above analysis only shows that the RRS algorithm does provide the smoothest solution. Next, we need to test the accuracy of the RRS algorithm. This can be done by comparing two receivers at the same station, because the reference clock noise is cancelled out, and only the time transfer noise remains. Figure 4.13 shows the time difference between the *NIST* receiver and the *NIS2* receiver at NIST determined by using different time-transfer methods [47].

We can clearly see that NRCan PPP solutions (blue, black, and orange curves) are quite artificial. The time difference between the two common-reference-clock receivers is not continuous. The RS algorithm (red curve) provides a continuous time transfer. However, compared to the RRS result, the RS result seems more artificial. For example, at MJD 56400.0, the red curve decreases very quickly. In contrast, there is almost no decrease in the NRCan PPP solutions (black and orange curves) and the RRS solution at this epoch. For another example, there is a peak with an amplitude of about 0.6 ns during MJD 56411–56416 in the red curve. In contrast, the peak is tiny in the RRS solution (green curve), which matches the NRCan PPP 30-day data-arc solution (orange curve). Both the NRCan PPP result and the RRS result for MJD 56440–56460 are smooth. In contrast, the RS solution for this period is quite noisy. All these features lead to the conclusion that the RRS algorithm provides time-transfer results closer to the true values than does the RS algorithm.

To further verify the above conclusion, we do another test. We run the RRS algorithm, together with RS, NRCan PPP, and TWSTFT (Two-Way Satellite Time and Frequency Transfer), for NIST and PTB for MJD 56375–56476 (Figure 4.14). Note, for the red and green curves, two receivers at NIST (*NIST* and *NIS2*) and two receivers at PTB (*PTBB* and *PTBG*) are used and averaged, respectively, because this can potentially provide a better time transfer result (see Section 3.4.4). We can see that TWSTFT (blue curve in Figure 4.14) has a diurnal oscillation that makes it a poor choice for short-term time transfer. The NRCan PPP with a 1-day data-arc

typically has a boundary discontinuity each day, which degrades the long-term time transfer result. Besides, the slope of each day also does not match the trend of TWSTFT well. For example, the black curve goes up on MJD 56378, while the blue curve goes down. For another example, the black curve is flat on MJD 56401, while the blue curve tends to go down. This inconsistency between TWSTFT and the NRCan PPP indicates that the NRCan PPP could have a wrong slope and thus an incorrect time comparison result. The NRCan PPP with a 10-day data-arc (magenta curve) and the NRCan PPP with a 30-day data-arc (orange curve) also do not match TWSTFT very well, though they are better than the NRCan PPP with a 1-day data-arc. We can see that the magenta curve drifts away from the blue curve. Then there is a boundary discontinuity that makes it match the blue curve again (e.g., the boundary at MJD 56385.0, 56405.0, 56425.0, and 56455.0, etc). Thus, the slope and the boundary discontinuity compensate each other. Since the boundary discontinuity should not appear in nature, we can say that the NRCan PPP result has an incorrect slope. Some people propose that we can use a longer data-arc (e.g., 35 days or 40 days) in order to avoid the appearance of the boundary discontinuity in the time range we are interested [44]. This method can still hardly avoid the incorrect slope. Thus, a time comparison using the conventional NRCan PPP with a super long data-arc could still introduce some man-made error. The “RINEX-Shift” result and the “revised RINEX-Shift” result are very close to each other (red curve and green curve in Figure 4.14). Both of them match TWSTFT very well. The boundary discontinuity in RS/RRS disappears, and the slope also matches the trend

of TWSTFT quite well. We should mention that we cannot distinguish RRS from RS in the time domain as shown in Figure 4.14. However, in the frequency domain (next paragraph), we will see the difference between RRS and RS.

To characterize how well all GPS carrier-phase time transfer results in Figure 4.14 match TWSTFT mathematically, we study the MTD of the difference between TWSTFT and each GPS carrier-phase time transfer (see Figure 4.15). Figure 4.15 clearly shows that the RRS result matches TWSTFT best. An obvious improvement of the RRS algorithm over the RS algorithm occurs at the averaging time of 2–15 days. In addition, the slope of the green curve during 1–15 days is approximately −1. This indicates that the flicker phase-modulation noise [15] dominates in the RRS time transfer during 1–15 days. Note that the green curve in Figure 4.15 sets the upper limit of the RRS time transfer noise (e.g., the RRS time-transfer noise is less than 4×10^{-16} for an averaging time of 4.25 days).

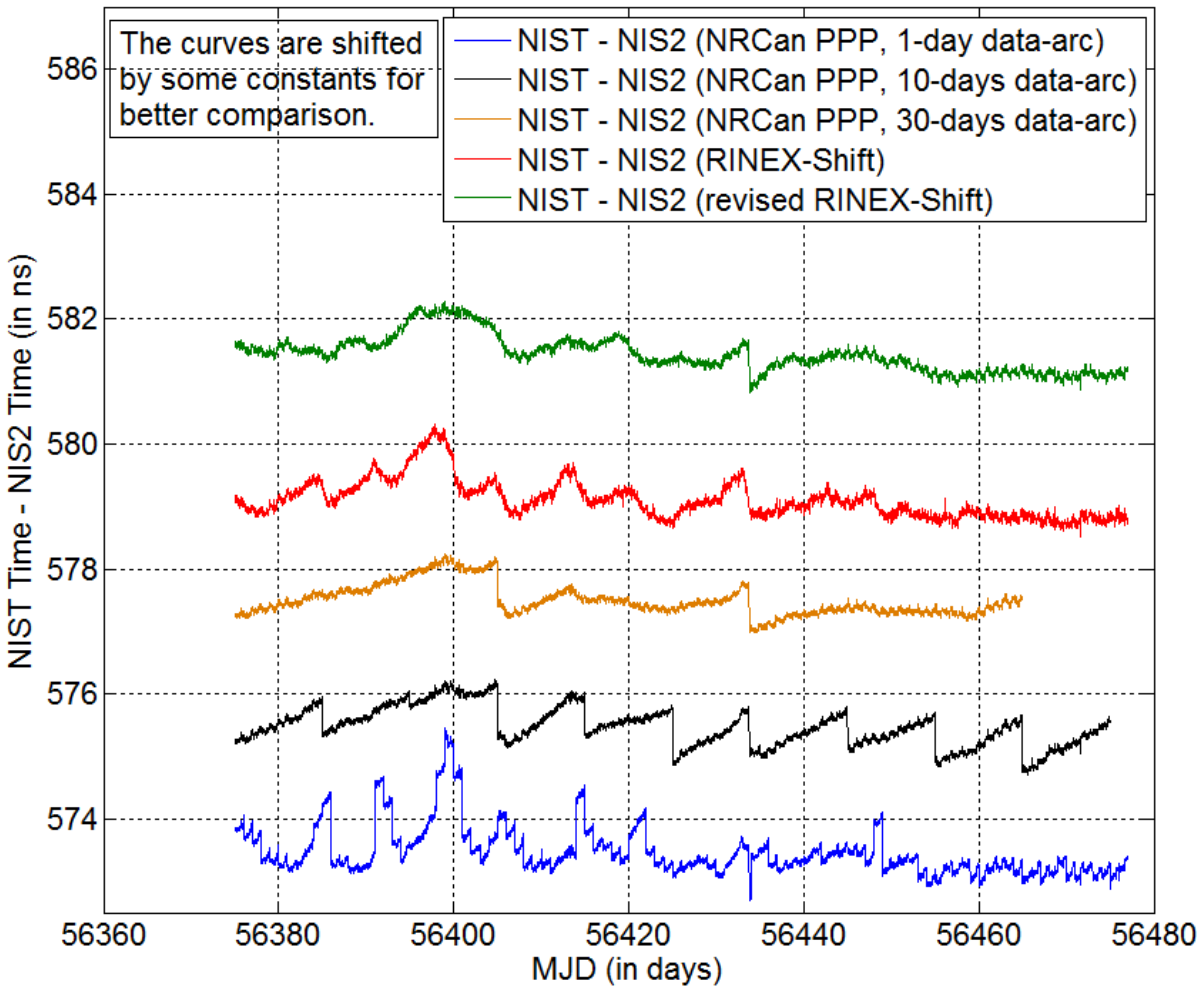

Figure 4.13. Time difference between *NIST* and *NIS2* for MJD 56375–56476, using different PPP time transfer methods [NRCan PPP with 1-day data-arc (blue curve), NRCan PPP with 10-day data-arc (black curve), NRCan PPP with 30-day data-arc (orange curve), RS algorithm (red curve), and RRS algorithm (green curve)].

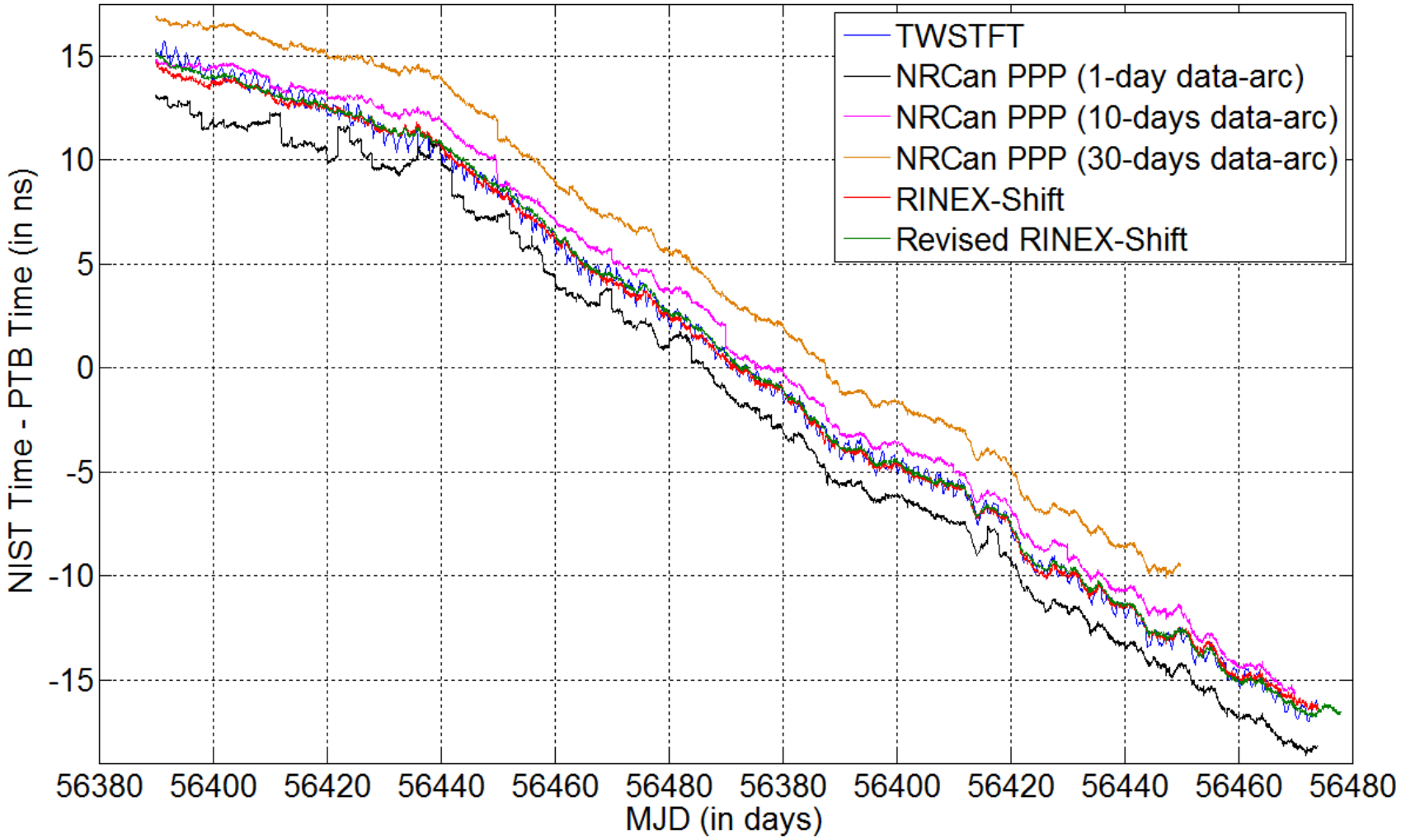

Figure 4.14. Time difference between UTC(NIST) and UTC(PTB) for MJD 56375–56476 by using TWSTFT (blue curve), NRCan PPP with a 1-day data-arc (black curve), NRCan PPP with a 10-day data-arc (magenta curve), NRCan PPP with a 30-day data-arc (orange curve), RS algorithm (red curve), and RRS algorithm (green curve). The curves are shifted by some constants for a better comparison.

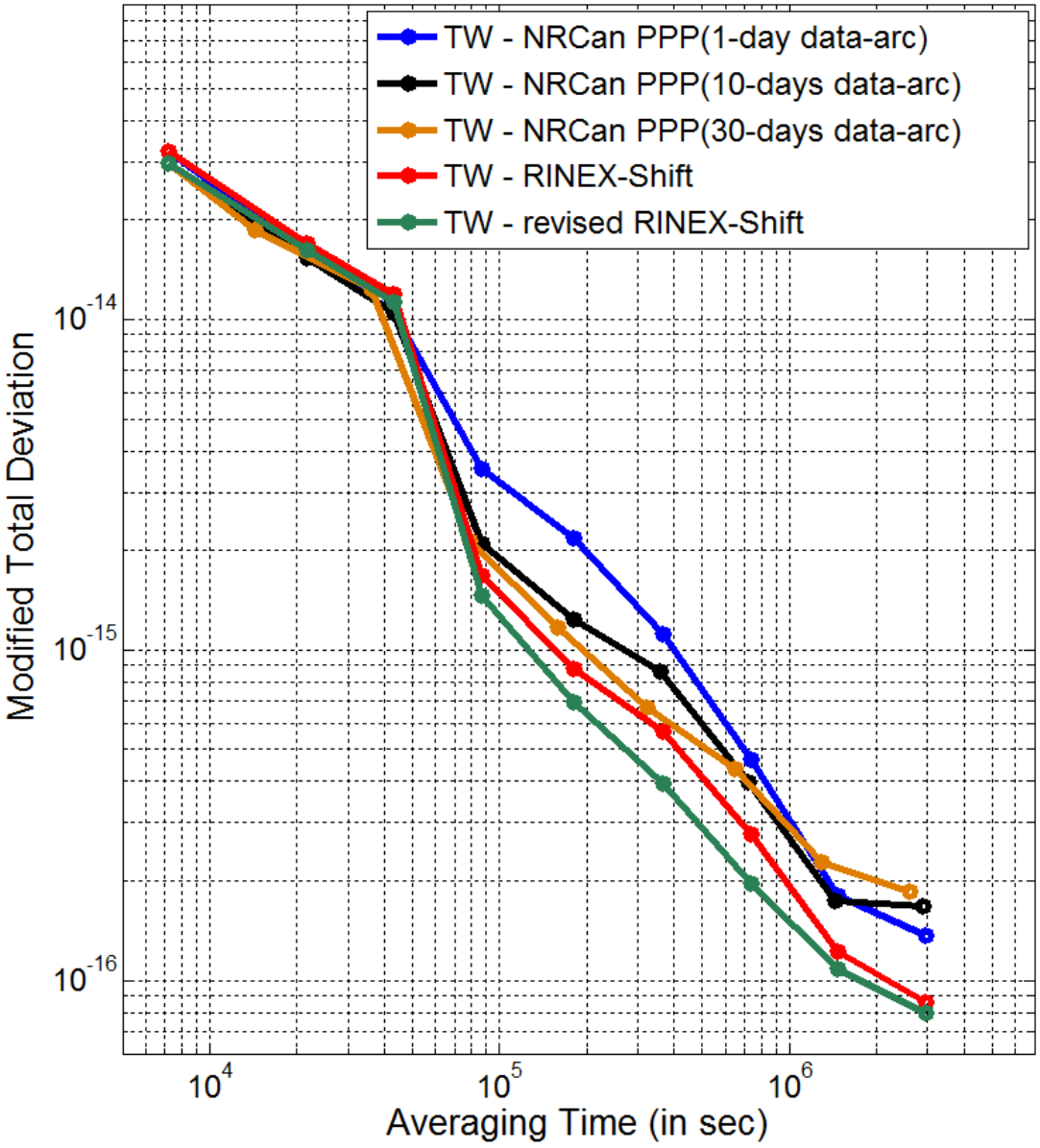

Figure 4.15. MTD of the double difference between TWSTFT and different GPS carrier-phase time-transfer methods [NRCan PPP with 1-day data-arc (blue curve), NRCan PPP with 10-day data-arc (black curve), NRCan PPP with 30-day data-arc (orange curve), RS algorithm (red curve), and RRS algorithm (green curve)], for MJD 56375–56476.

To provide the time transfer noise of the RS and RRS algorithms, we merge Figure 4.12 and Figure 4.15 together. In this way, we have the characteristic of the

RS and RRS time transfer noise for both short term (< 1 day) and long term (> 1 day) (see Figure 4.16).

The details about how we merge Figure 4.12 and 4.15 into Figure 4.16 are worth discussing. First, for a short term, the time difference between two long-distance stations (Figure 4.12) has noise from both clock and time transfer (note that the short-term UTC(k) clock noise is typically smaller than the time transfer noise). Thus, Figure 4.12 sets the upper limit for time transfer noise. To be conservative, we simply set Figure 4.16 the same as Figure 4.12 for the short term. The actual short-term time-transfer noise should be smaller than what Figure 4.16 shows. Second, for a long term, we assume that TWSTFT and carrier-phase time transfer have a comparable noise level (In fact, TWSTFT should be noisier than carrier-phase in the long term. To be conservative, we assume they are the same.). Thus, the long-term time transfer noise in Figure 4.16 comes from the result in Figure 4.15 divided by $\sqrt{2}$.

From Figure 4.16, we know that the RRS algorithm provides the smallest time-transfer noise. For example, the fractional frequency stability is 3×10^{-15} for an averaging time of ~0.5 days; the stability is 1×10^{-15} for an averaging time of ~1 day; and the stability is 1×10^{-16} for an averaging time of ~10 days.

As a whole, the RRS algorithm successfully removes the RS algorithm's damped-oscillation problem that occurs before the anomaly. More importantly, it matches TWSTFT best and reduces the time-transfer noise of the RS algorithm by 10–55%. This makes the RRS algorithm the best GPS time-transfer method.

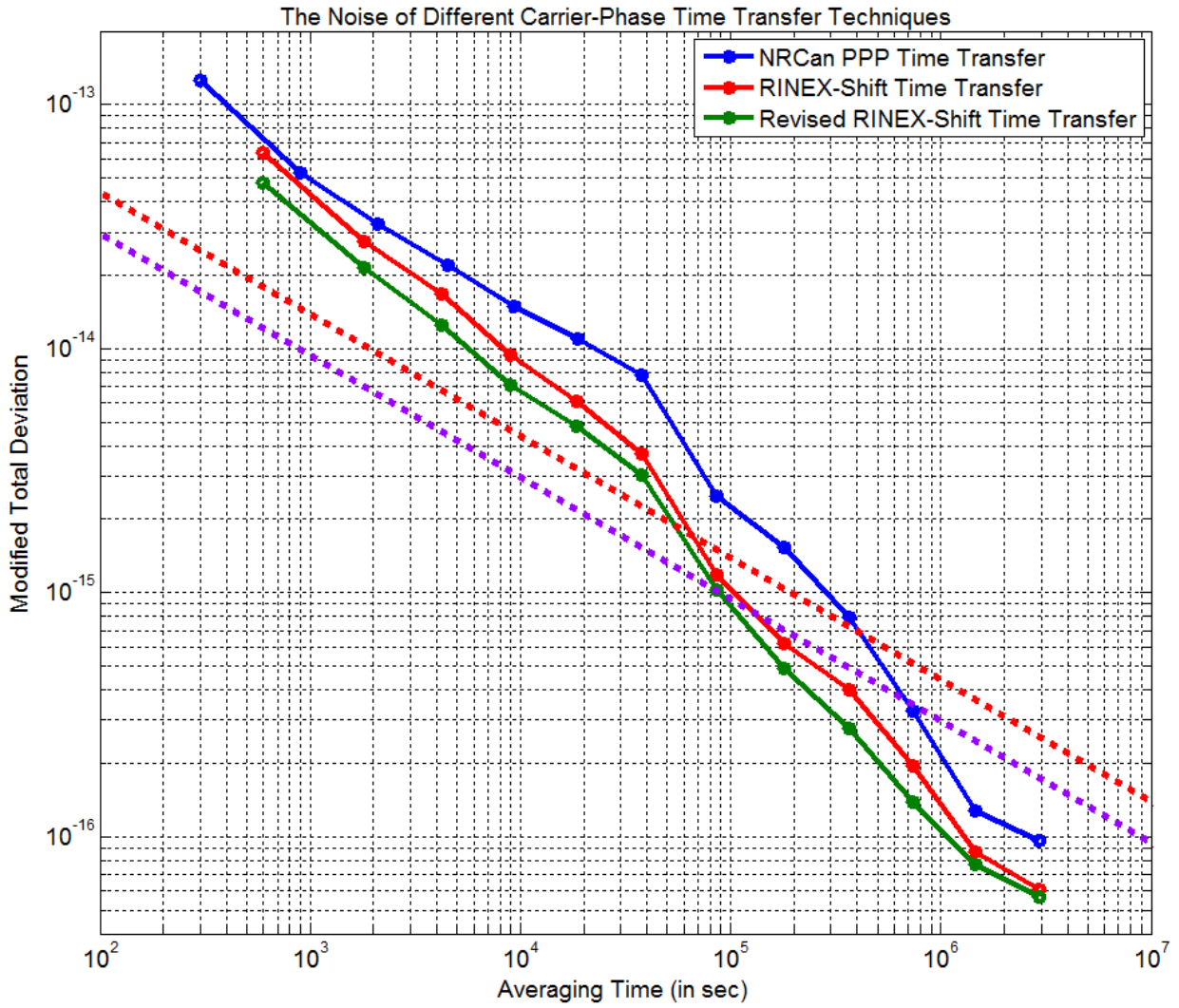

Figure 4.16. Frequency stability of different carrier-phase time-transfer techniques [NRCan PPP with a 1-day data-arc (blue curve), RINEX-Shift algorithm (red curve), and revised RINEX-Shift algorithm (green curve)]. The purple dotted line is the frequency stability of a single Cesium fountain clock [36]. The red dotted line is the frequency stability of two Cesium fountain clocks compared to each other.

4.7 Fountain Comparisons

Now we want to apply the new time-transfer technique (i.e., RS/RRS algorithm) to Cesium (Cs) fountain clock comparisons.

A single Cs fountain-clock noise (purple dotted line in Figure 4.16) was evaluated in [36] (also see Figure 2.2 in Section 2.1). If we want to compare two long-distance fountain clocks, the total fountain-clock noise (red dotted line in Figure 4.16) should be $\sqrt{2}$ of that of a single fountain clock, if we assume the two fountain clocks have the same performance.

From Figure 4.16, we can see that the clock noise is a major contributor after about half a day if the RS/RRS time-transfer technique is applied. In contrast, if the conventional NRCan PPP (or carrier-phase) time-transfer technique is used, the clock behavior only starts to be observed after 5 days! Clearly, the RS/RRS time transfer technique pushes the long-distance clock-observation threshold from 5 days to 0.5 days.

As an example, we compare the NIST F1 Cs fountain with the Paris Observatory (OP, France) FO2 Cs fountain during MJD 56497.7–56533.6 by TWSTFT, NRCan PPP (1-day data-arc), and the RS algorithm (Figure 4.17). The TWSTFT shows that there is a long-term oscillation between two fountain clocks. The period is approximately 20 days. However, the obvious diurnal problem (i.e., about 0.6 ns peak-to-peak) in TWSTFT degrades its short-term resolution. Without solving the diurnal problem in TWSTFT, TWSTFT is not very good for precise time comparison, such as a Cs Fountain-clock comparison. The conventional NRCan PPP (1-day data arc) is accepted by many national laboratories for precision time transfer. Even though NRCan PPP provides a good short-term stability (< 6 hours), it is even worse than TWSTFT in the long term (blue curve). For example, it can

hardly resolve the 20-day oscillation behavior between the two fountain clocks because of the day boundary discontinuity. In contrast, the RS algorithm (red curve) solves the day boundary discontinuity perfectly (note that two GPS receivers, *NIST* and *NISA*, are used at NIST in the RS algorithm.). It resolves the 20-day oscillation behavior very well. Besides, it can also see the short-term (~0.5 day) clock behavior quite well. For example, at around MJD 56520.0, there is a sudden decrease in the red curve. Checking with the trend of the blue curve at around MJD 56520.0, we can also see a decrease. This confirms that this decrease comes from the clock behavior. This also indicates that the RS/RRS time transfer is able to resolve short-term (~0.5 day) clock behavior.

In terms of frequency stability, we get Figure 4.18 based on Figure 4.17 (note, the bump occurring at an averaging time of 10 days comes from the 20-day oscillation behavior in fountain clocks). Clearly, the RS/RRS time transfer has the smallest noise in the fountain comparison. TWSTFT is worse than the RS/RRS time transfer in both the short term (< 1 day) and the long term (> 1 day). NRCan PPP is comparable to the RS/RRS time transfer in the super-short term (< 3 hours). However, it is inferior to the RS/RRS time transfer for an averaging time of longer than 6 hours. When we look at the total fountain clock noise (red dotted line), we can see that the clock noise becomes a major contributor after ~12 hours in the RS/RRS time transfer. In contrast, in TWSTFT and NRCan PPP, the time-transfer noise dominates until approximately 6 days. This result matches our prediction at

the beginning of this section that the RS/RRS time-transfer technique pushes the long-distance clock-observation time threshold from ~5 days to ~0.5 days.

From the above analysis, the RS/RRS algorithm provides an obviously better time-transfer result than both TWSTFT and the conventional carrier-phase time-transfer (or PPP) technique. This makes the RS/RRS algorithm good for observing the short-term (~0.5 day) behavior of a long-distance Cesium fountain clock.

4.8 Summary

This chapter proposed the RINEX-Shift (RS) algorithm to solve the day-boundary-discontinuity problem in the carrier-phase time transfer. This algorithm showed a performance superior to the conventional carrier-phase time transfer. The revised RS (RRS) algorithm was designed to improve the performance of the RS algorithm at data anomalies. In addition, the RRS algorithm also provided 10–55% better short-term and long-term stability than the RS algorithm. Most importantly, the RS/RRS result matched TWSTFT better than the conventional carrier-phase time-transfer techniques. All these features indicate that the RS/RRS algorithm is the best carrier-phase time-transfer technique for the time being. Finally, we explored the applications of the RS/RRS algorithm. It showed that the RS/RRS algorithm allowed us to observe long-distance Cs fountain-clock behavior after 0.5 days. In contrast, TWSTFT and the conventional carrier-phase time transfer required at least 5 days.

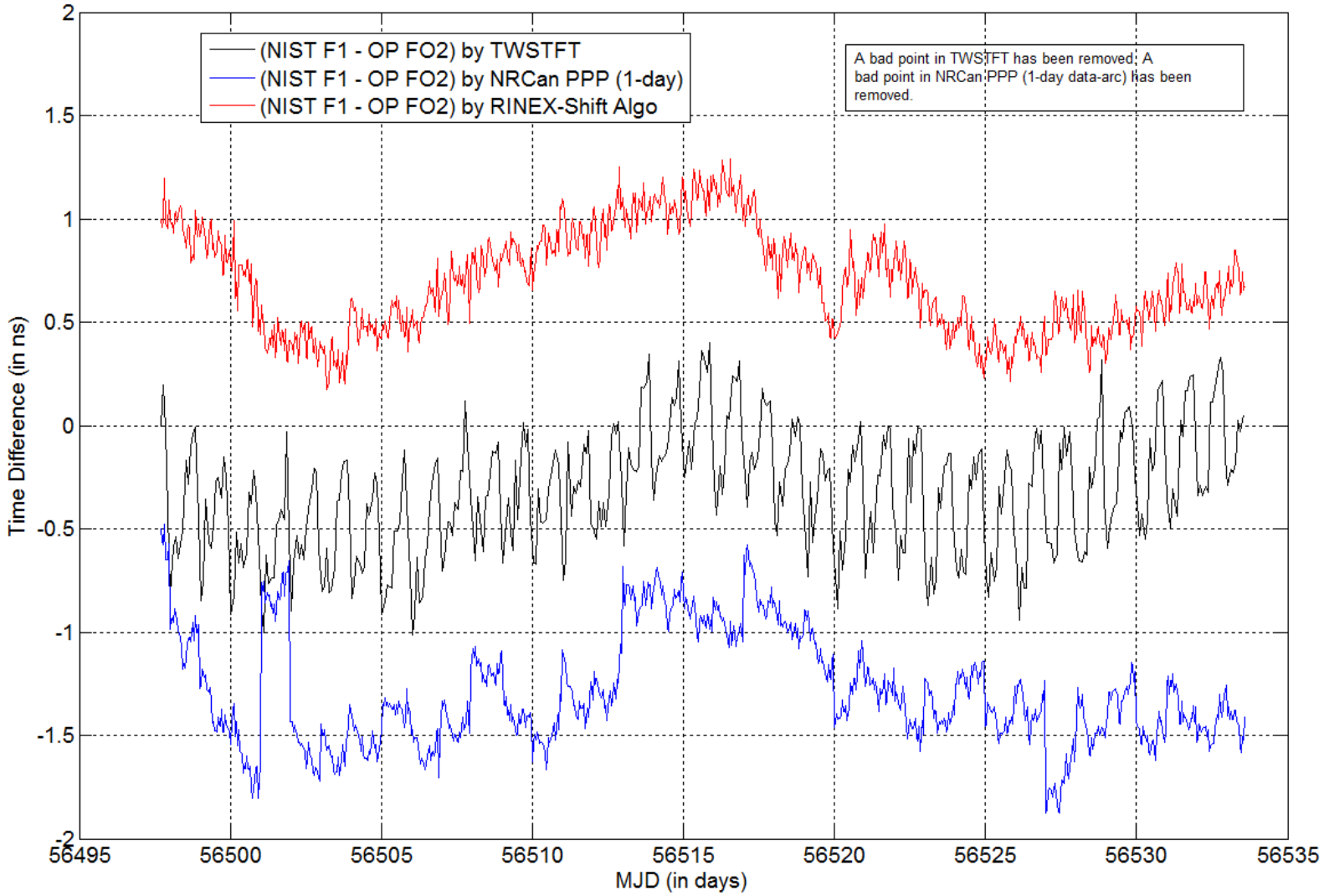

Figure 4.17. Fountain Comparison between NIST F1 Cs fountain and OP FO2 Cs fountain for MJD 56497.7–56533.6 by using TWSTFT (black curve), NRCan PPP with 1-day data-arc (blue curve), and the RS algorithm (red curve).

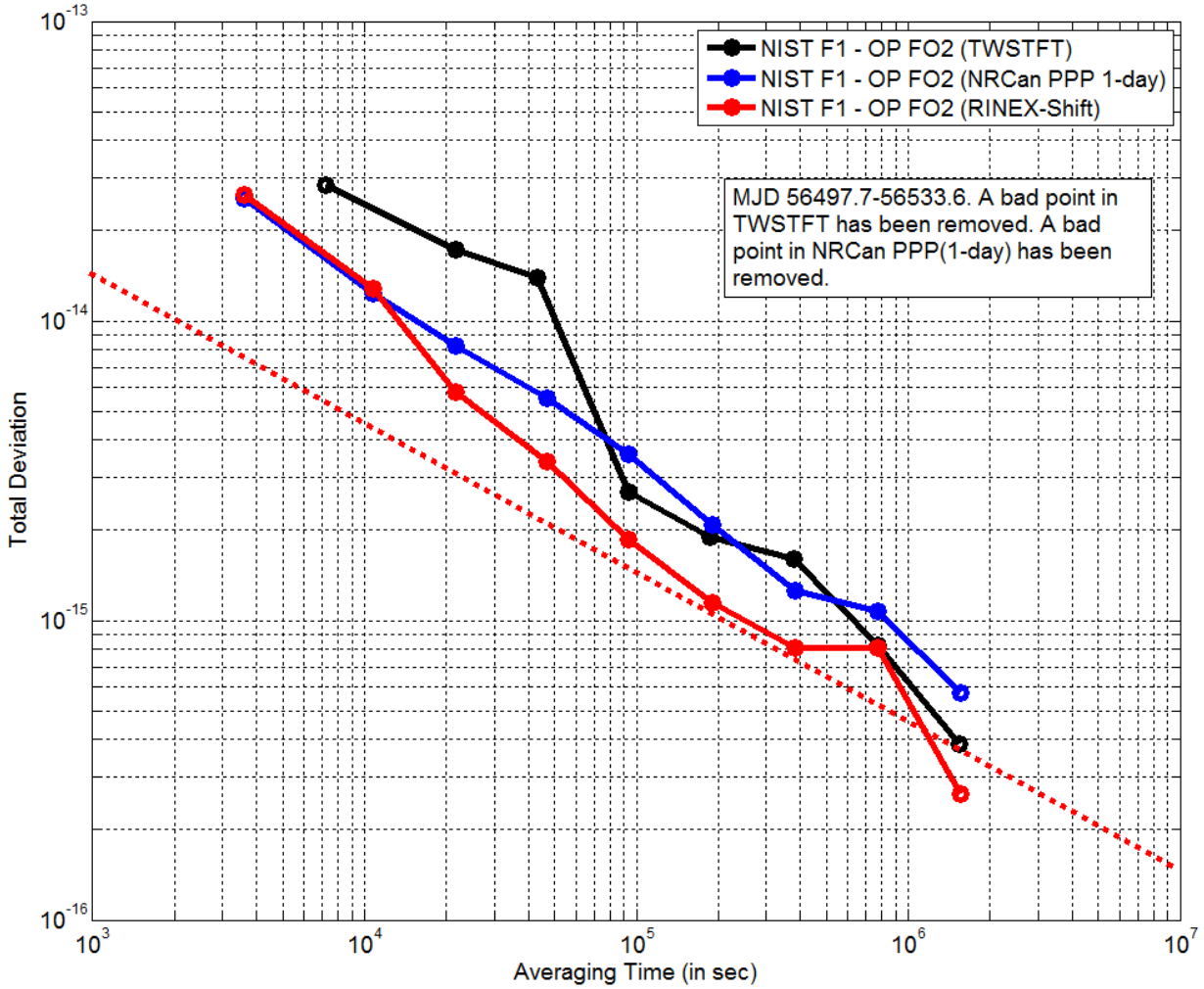

Figure 4.18. Total deviation of time difference between NIST F1 Cs fountain and OP FO2 Cs fountain for MJD 56497.7–56533.6, using TWSTFT (black curve), NRCan PPP with 1-day data-arc (blue curve), and the RS algorithm (red curve).

Chapter 5

Boundary Discontinuity Due To GPS Measurements Anomaly[1]

5.1 Introduction

As stated in Section 1.6, there are two categories of boundary discontinuity. The first category of boundary discontinuity is "data-batch boundary discontinuity", which has been discussed in Chapters 2–4. The second category of boundary discontinuity is "boundary discontinuity due to GPS measurements anomaly" (for short, anomaly-BD). This chapter focuses on the second category of boundary discontinuity.

Within one data batch, there may be some missing data or bad data caused by many reasons. For example, an extreme ionospheric activity can lead to a change of tens of nanoseconds of path delay [59]. The satellite-receiver line may be blocked by some objects. The reference time for the receiver may also be adjusted. Even the receiver may function incorrectly [60]. Although people have proposed some strategies of better monitoring ionosphere [61] or re-designing a GPS receiver, the

[1] The results of this chapter are mainly based on [58].

problem of missing/bad data is almost inevitable. When there are missing/bad data, the PPP software usually re-estimates the phase ambiguity after the anomaly. Thus, there can be a discontinuity at the anomaly.

As an example, we compare the time difference between *NISA* (a GPS receiver at NIST) and the IGS final time on Modified Julian Date (MJD) 56325 by using PPP. The original PPP result is shown by the blue curve in Figure 5.1. The blue curve is continuous because of no data anomaly. However, if we delete 10 min of RINEX data (note that RINEX data provide the code and phase measurements of a GPS receiver), the PPP result (black curve in Figure 5.1) has a discontinuity at the time of the missing data. In this specific case, the discontinuity is as big as ~250 ps.

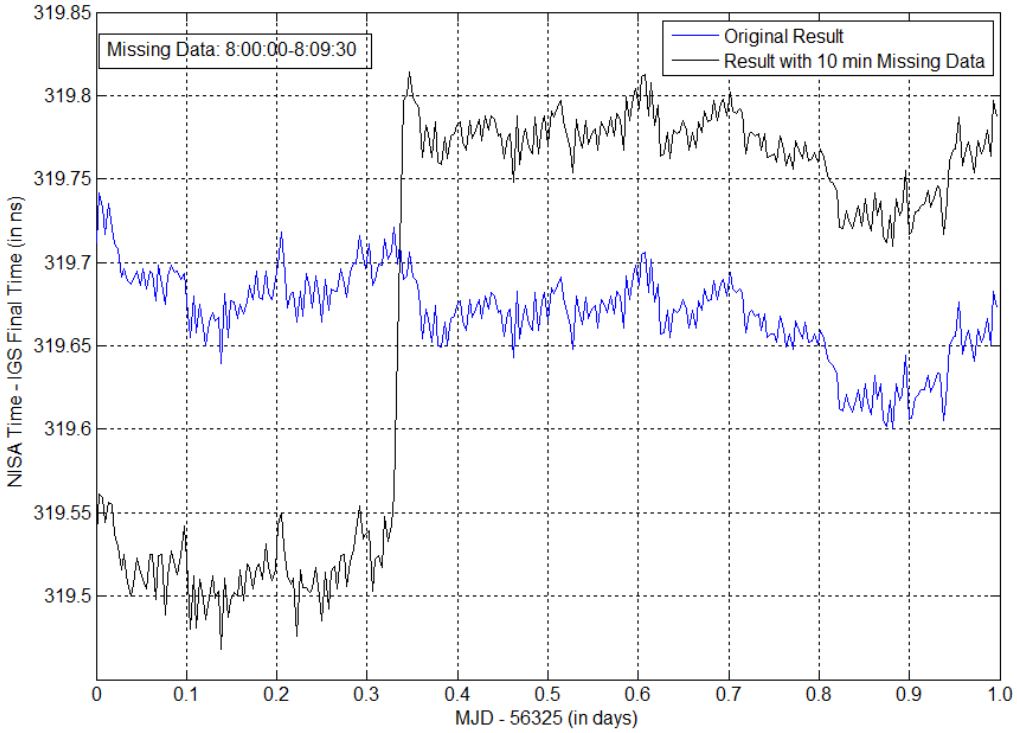

Figure 5.1. Illustration of the "boundary discontinuity due to GPS measurements anomaly". The blue curve is the PPP result with the original RINEX file as the input. The black curve is the PPP result with the RINEX file lacking the data between 8:00:00–8:09:30 as the input. Note, *NISA* is a GPS receiver at NIST.

From the above, we know that a few minutes of GPS measurement anomaly is enough to lead to a discontinuity of a few hundred picoseconds in the GPS carrier-phase time transfer. This anomaly-BD is typically at the same level of the day boundary discontinuity. With the revised RINEX-Shift (RRS) algorithm, we are able to eliminate the day boundary discontinuity very well. However, this algorithm can do nothing with the anomaly-BD. Thus, we want to find a strategy to deal with this category of boundary discontinuity (i.e., anomaly-BD).

5.2 Curve Fitting for GPS Code and Phase Measurements

A straightforward strategy for dealing with the anomaly-BD is to do curve fitting for the anomaly. We first extract the code and phase measurements for each satellite from the RINEX file. Then we detect the anomaly. If there is an anomaly, then we use polynomial regression (typically the 9^{th} or 10^{th} order of the polynomial) to fit the good data both before and after the anomaly. Then the fitted result during the time range of the anomaly is used to replace the missing/bad measurements. In the end, we save the fitted code and phase measurements to the RINEX file. Now, when we run PPP with the revised RINEX file as the input, PPP does not need to re-estimate the phase ambiguities at the anomaly since the anomaly has already been “repaired”. Thus, we should have a continuous time-transfer result at the anomaly. Of course, the time-transfer result during the time range of the anomaly should finally be disregarded, because the RINEX data at the anomaly is “made” by the polynomial regression.

An important reminder here is that this strategy only works very well for national laboratories that have near-perfect reference clocks, or GPS receivers with very good rubidium or cesium clocks as their references. This strategy does not work well for the RINEX data recorded by the GPS receiver without a precise reference clock. For example, a quartz oscillator can drift by more than 100 ns in an hour. If the GPS receiver only has a quartz oscillator as the reference clock, the instability of the quartz oscillator can lead to an uncertainty of the curve-fitted RINEX data being hundreds of nanoseconds or even more. Thus, PPP still needs to re-estimate the phase ambiguities. Therefore, the boundary discontinuity at the anomaly is still there and cannot be removed by the curve-fitting strategy.

5.3 Verification of Curve-Fitting Strategy

To verify the curve-fitting strategy in Section 5.2, we first run carrier-phase time transfer for the original good GPS measurements data recorded by the *NISA* receiver at NIST (from MJD 56325.000 to MJD 56325.999). There is no discontinuity because of no anomaly (see the blue curve in Figure 5.2). Then we delete 20 min of measurements data (6:00:00–6:19:30) and run the carrier-phase time transfer (see the black curve in Figure 5.2). The time difference between 56325.250 and 56325.264 is as big as 260 ps, which indicates a discontinuity.

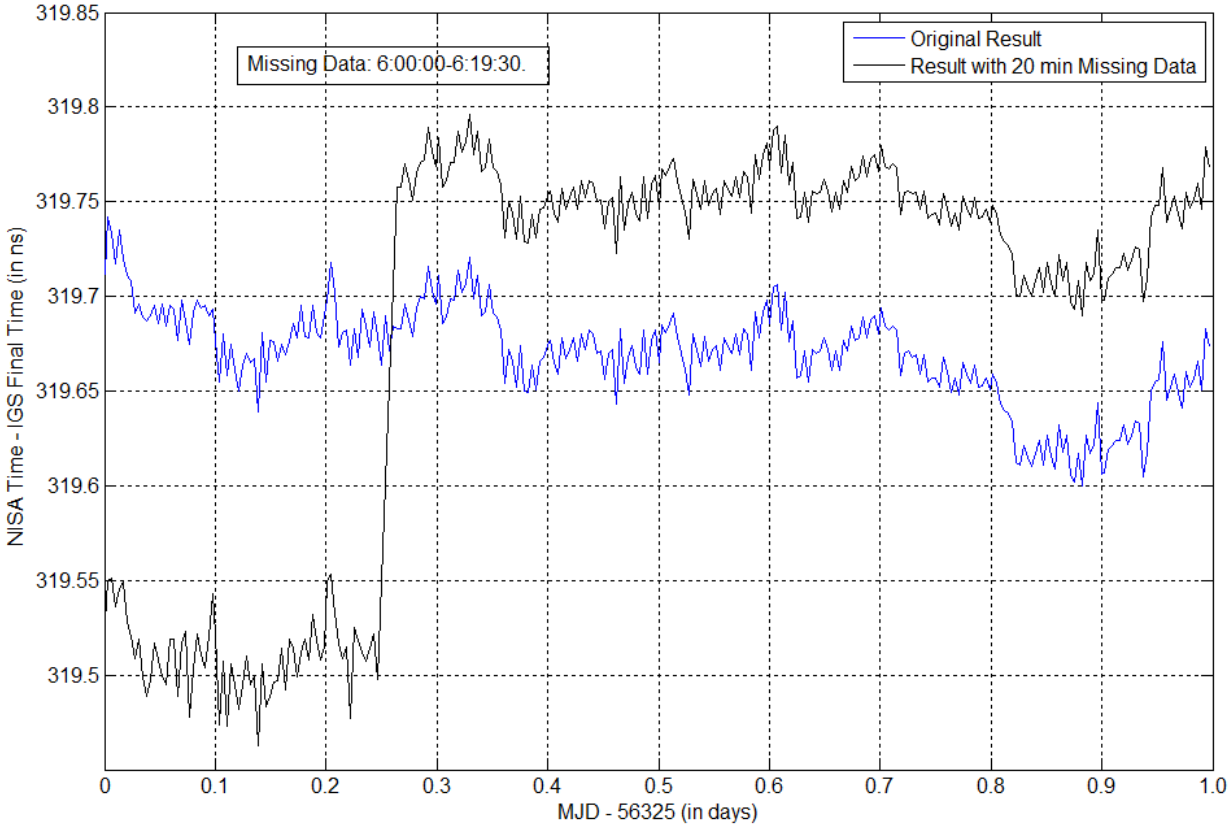

Figure 5.2. Boundary discontinuity due to 20 min of GPS missing data (black curve). The blue curve is the time transfer with all good data, as a reference.

Now, let's implement the curve-fitting strategy. We do curve fitting for the 20 min of missing data for each satellite by using the good data during 5:30:00–5:59:30 and 6:20:00–6:49:30 (i.e., half an hour before the anomaly and half an hour after the anomaly). Figure 5.3(a) shows the fitted result of phase measurements for PRN01, as an example. Figure 5.3(b) shows the difference (or residual) between the original data and the fitted data during 5:30:00–6:49:30. Clearly, during the time range of missing data (6:00:00–6:19:30), the difference between the original data and the fitted data is less than 0.1 cycle (i.e., less than 1.9 cm). The rms of the difference is

0.03 cycle (i.e., 0.57 cm). Figure 5.4 is similar to Figure 5.3, but is for code measurements. The rms of the difference between the original data and the fitted data is 0.67 m.

Admittedly, PRN01, as an IIF-block satellite, has a rubidium clock with a small short-term (< 3 hours) noise. Thus, the satellite clock noise has little impact on the curve fitting result. Because of this, we have a very small rms of phase measurements, as shown in Figure 5.3(b). However, for the PRNs from the old satellite blocks, such as Block IIA and Block IIR, the short-term (< 3 hours) clock noise is larger. Thus, the rms of phase measurements (Figure 5.5) is typically greater than PRN01. However, this does not mean that the rms is very large. Figure 5.5 actually shows that the rms is below 0.3 cycle (i.e., 5.7 cm), which is still an acceptable curve-fitting result. The rms of code measurements for other PRNs (Figure 5.6) is similar to PRN01, i.e., ~0.7 m, because the satellite clock noise is only a small part of the total code noise.

From the above discussion, we can see that the curve fitting for code and phase measurements works very well. Statistically, the rms of the residuals after curve fitting for code measurements is typically less than 0.8 m. And, the rms of the residuals for phase measurements is typically less than 5.7 cm. Thus, with the fitted code and phase measurements, we can potentially "make" the data good. Because the data are "good" after applying the curve-fitting strategy, we can now avoid the re-estimation of phase ambiguities at the anomaly in the PPP processing, and thus eliminates the anomaly-BD.

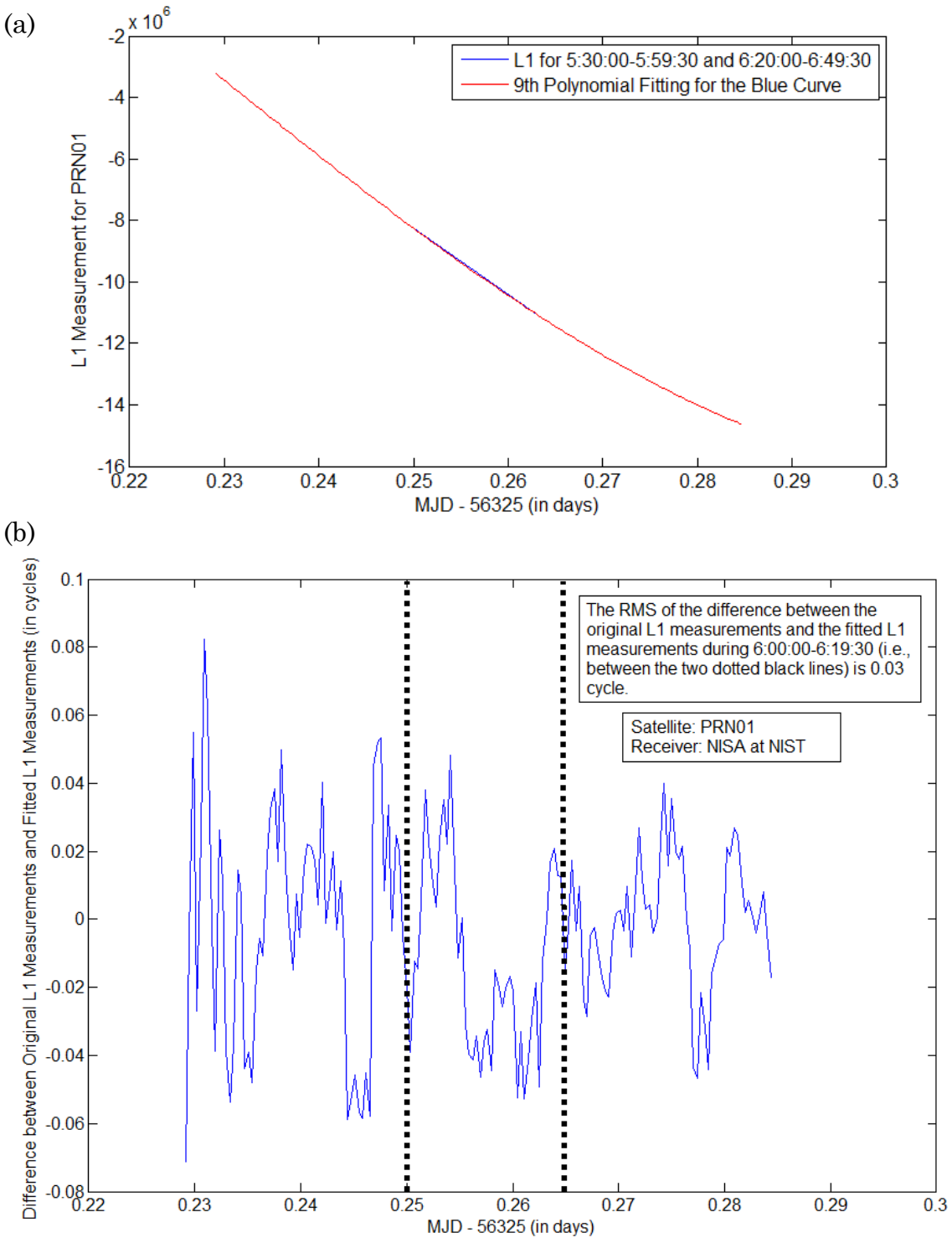

Figure 5.3. Curve fitting of the phase measurements for PRN01. Missing data occurs during 6:00:00–6:19:30. The blue curve in (a) is the phase measurements for PRN01 during 5:30:00–5:59:30 and 6:20:00–6:49:30. The red curve in (a) is the 9th order of polynomial fitting. (b) is the phase-measurements difference (or residual) between the original data and the fitted data during 5:30:00–6:49:30.

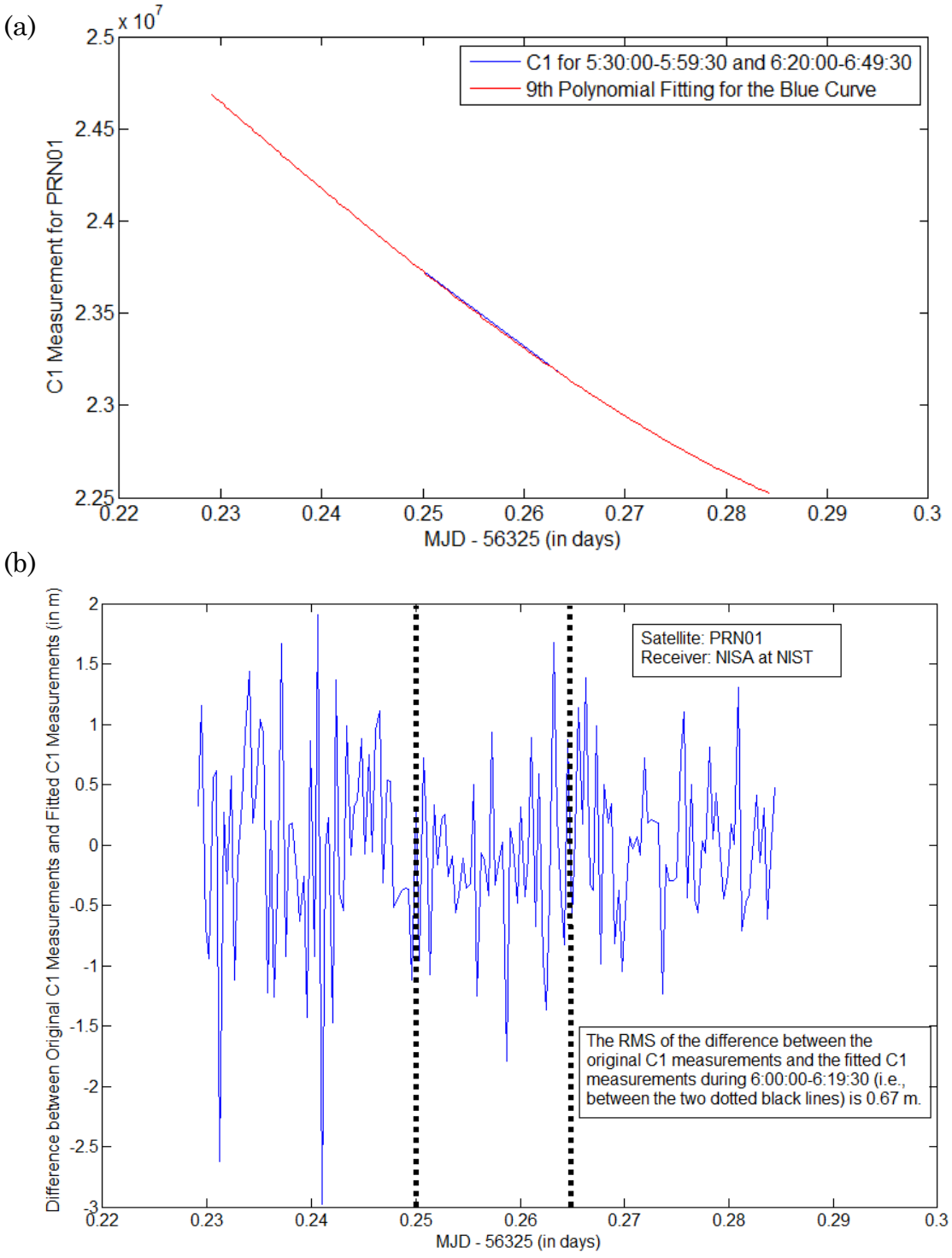

Figure 5.4. Curve fitting of the code measurements for PRN01. Missing data occurs during 6:00:00–6:19:30. The blue curve in (a) is the code measurements for PRN01 during 5:30:00–5:59:30 and 6:20:00–6:49:30. The red curve in (a) is the 9th order of polynomial fitting. (b) is the code-measurements difference (or residual) between the original data and the fitted data during 5:30:00–6:49:30.

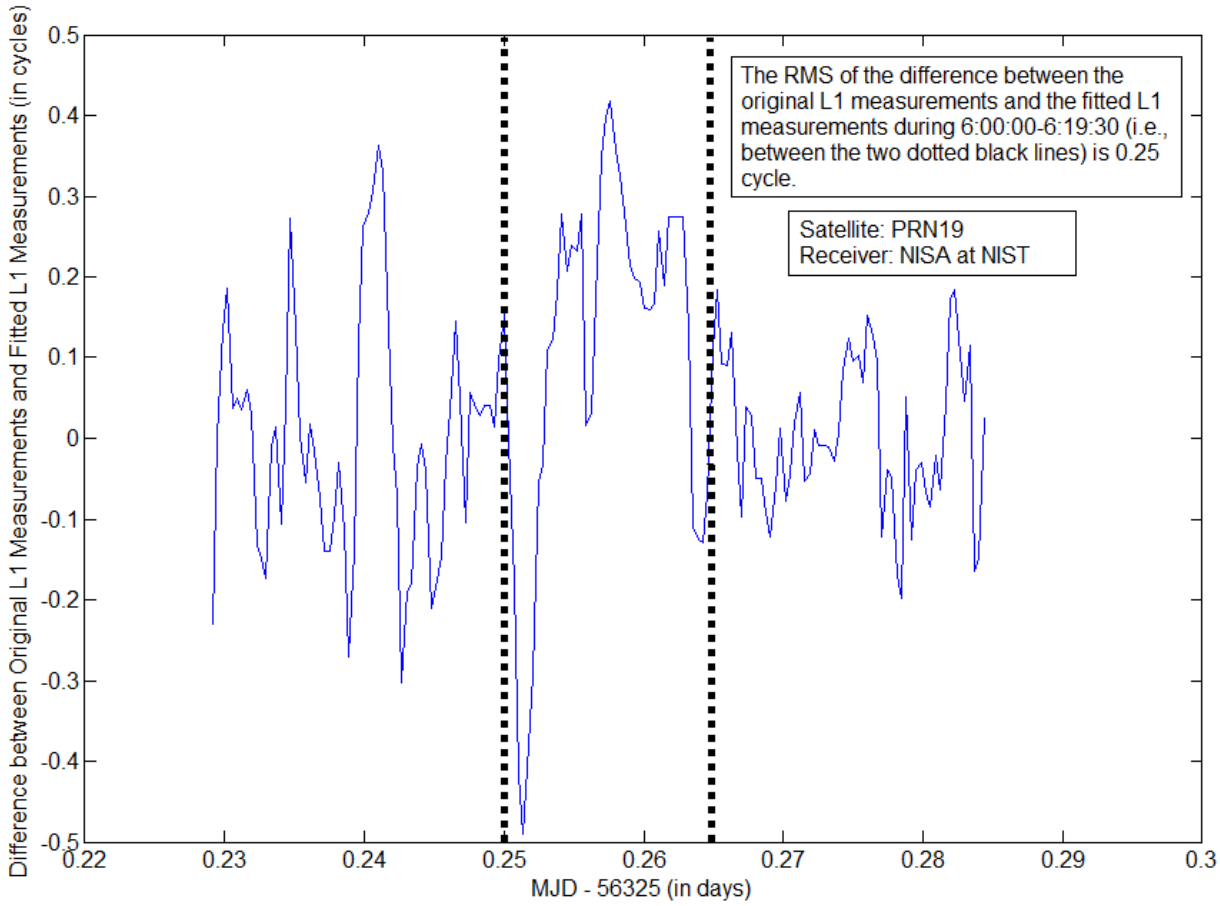

Figure 5.5 The phase-measurements difference (or residual) between the original data and the fitted data during 5:30:00–6:49:30, for PRN19. It is similar to Figure 5.3(b).

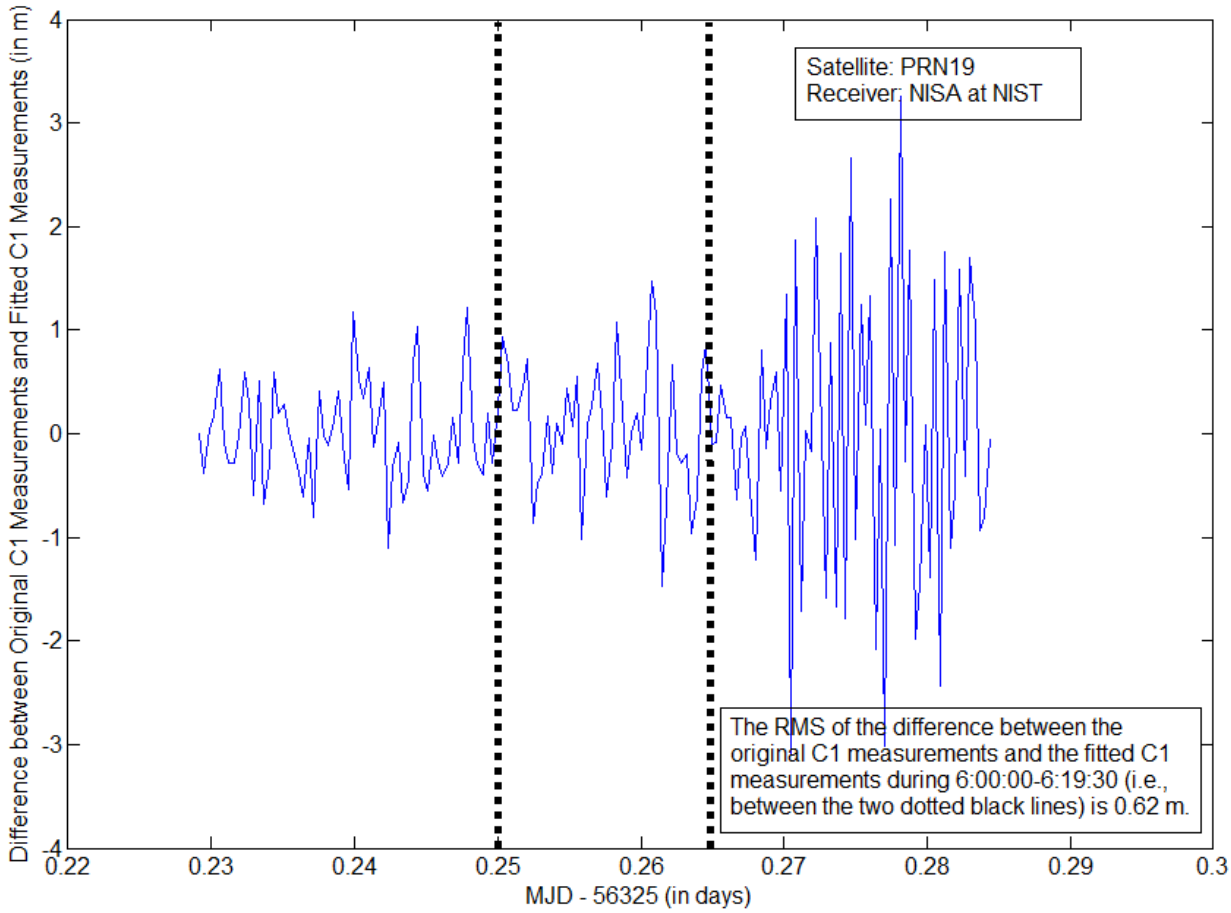

Figure 5.6. The code-measurements difference (or residual) between the original data and the fitted data during 5:30:00–6:49:30, for PRN19. It is similar to Figure 5.4(b).

To test the conjecture that the curve-fitting strategy can eliminate the anomaly-BD, we replace the 20-min missing data in the RINEX file with the fitted data and then run PPP for the revised RINEX file. The result is shown by the red curve in Figure 5.7. Clearly, the discontinuity just disappears. This demonstrates that the curve-fitting strategy successfully solves the discontinuity problem in the black curve. We have also conducted the same procedures as the above for the anomaly occurring at other times, such as 7:00:00–7:19:30, 12:00:00–12:19:30. All of

them show a very similar continuous time-transfer result as shown by the red curve in Figure 5.7. This further confirms our conclusion that the curve-fitting strategy works very well for the boundary-discontinuity problem at a data anomaly.

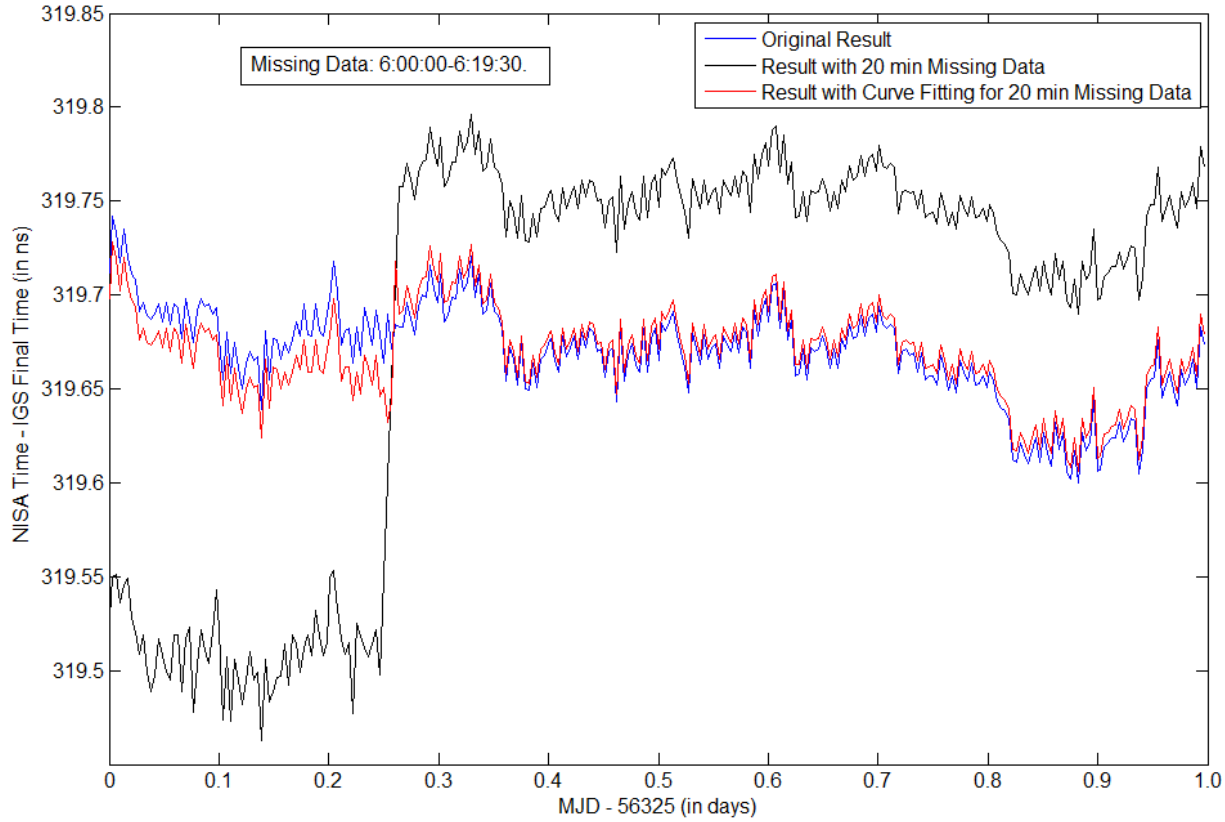

Figure 5.7. Curve-fitting strategy for eliminating the anomaly-BD (red curve). The blue and red curves are the same as Figure 5.2. They are included in this figure for comparison.

5.4 Summary and Outlook

In this chapter, we discussed the anomaly-BD, and proposed the polynomial curve-fitting strategy to solve this problem. Tests showed that this strategy worked quite well for up to 20 min of measurements anomaly.

Admittedly, there is still a lot of work to do in order to completely solve the problem of anomaly-BD. For example, what we discussed in this chapter mainly focused on the situation where we have good data before and after the anomaly. However, in practice, we may have a big step after the anomaly, due to either a cycle slip or a time step in the reference clock of a GPS receiver. Even at national laboratories, a time step of tens of nanoseconds in the reference clock occurs from time to time (typically, a few times a year). This time step may come from changing the current time scale to a backup time scale, or from updating the time-distribution system, or even from replacing the time-reference cable for the GPS receiver. The cycle slips can typically be corrected during the pre-processing of PPP. However, the time steps in the reference clock are not so easy to deal with. For the time steps in the reference clock, the carrier-phase time transfer must re-estimate the phase ambiguities. Thus, the observed time step is a combination of the actual time step and a boundary discontinuity introduced by the time step. If we can find a method to eliminate the boundary discontinuity due to this type of anomaly, we can better estimate the actual time step in the reference clock.

As we know, satellite clock noise can be as big as a few cm for an averaging time of 5 min. In Section 5.3, we do curving fitting for the code and phase measurements. But these measurements include the satellite clock noise. Thus, the residual after curve fitting contains the satellite clock noise. This makes the curve fitting imperfect. A better strategy for curve fitting would be to apply the precise satellite clock offsets (i.e., IGS clk data) to the code and phase measurements first,

and then do polynomial curve fitting next. In this way, the residual after curve fitting will become smaller. I have done some tests on this new strategy. The residual of L1 phase measurements reduces from ~0.8 cycle (peak-to-peak) to 0.06 cycle (peak-to-peak), for most GPS satellites. We expect that this new strategy may push the current allowed data-anomaly window of 20 min further to approximately 1 hour.

Chapter 6

Summary

In this thesis, we report studies of the day boundary discontinuity (day-BD) problem in GPS carrier phase time transfer (GPSCPTT).

In terms of statistics, we find that the day-BD has a near-Gaussian distribution. Different stations have different means and standard deviations (STD) of day-BD. Besides, as the data-arc length increases (e.g., from 1 day to 4 days), both mean and STD of day-BD increases. In particular, the mean increases linearly. This makes the 35-day data-arc GPSCPTT done by the International Bureau of Weights and Measures (BIPM) problematic.

The origin of day-BD comes from the re-estimation of phase ambiguities for the next day. We find code noise, instead of phase noise, mainly leads to day-BD. We find that the boundary discontinuity can be reduced by 10–30% using IGS 30-sec clock products, instead of IGS 5-min clock products. The tropospheric path noise seems have little impact on the boundary discontinuity. The boundary discontinuity can be further lowered by 10–20% if a few GPS receivers at the same station are averaged. The anomaly in the RINEX data can also sometimes lead to a large

boundary discontinuity and an incorrect slope in the time transfer. The comparison between the PPP method and the network method indicates that the network method provides a smaller boundary discontinuity.

To eliminate day-BD, we have designed the RINEX-Shift (RS) algorithm and the revised RINEX-Shift (RRS) algorithm. Both of them provide continuous GPSCPTT results. However, the RS algorithm has a damped-oscillation problem when GPS data have anomalies. We proposed the RRS algorithm to solve this problem. RS/RRS matches two-way satellite time/frequency transfer (TWSTFT) much better than the conventional GPSCPTT. The RS/RRS time transfer noise is typically 1.4×10^{-14} for an averaging time of 1 hr, 2.5×10^{-15} for 0.5 day, 1.0×10^{-15} for 1 day, 3.0×10^{-16} for 4 days, and 7.5×10^{-17} for 20 days. We are able to observe the high-precision Cesium fountain clock behavior after 0.5 day using RS/RRS time transfer, instead of ~5 days using the conventional GPSCPTT. This makes RS/RRS the best GPS time-transfer technique.

In addition to day-BD, we also have a boundary discontinuity at the data anomaly (anomaly-BD) because of re-estimation of phase ambiguities. We proposed a simple polynomial curve-fitting strategy to repair the data anomaly. The curve-fitted GPS phase data are typically less than 6 cm from the actual GPS phase data. Tests show that this strategy works for at least a 20-min data anomaly. Thus, we have successfully eliminated the anomaly-BD.

In a summary, with the effort of studying and eliminating the BD problem, we have achieved continuous GPS carrier-phase time transfer.

Bibliography

[1] S. R. Jefferts, T. P. Heavner, and E. A. Donley, "Cesium primary frequency references," Jpn. J. Appl. Phys., vol. 43, no. 5B, pp. 2803–2807, 2004.

[2] W. H. Oskay, S. A. Diddams, E. A. Donley, T. M. Fortier, T. P. Heavner, L. Hollberg, W. M. Itano, S. R. Jefferts, M. J. Delaney, K. Kim, F. Levi, T. E. Parker, and J. C. Bergquist, "Single-atom optical clock with high accuracy," Phys. Rev. Lett. 97, 020801, 2006.

[3] B. J. Bloom, T. L. Nicholson, J. R. Williams, S. L. Campbell, M. Bishof, X. Zhang, W. Zhang, S. L. Bromley, and J. Ye, "An optical lattice clock with accuracy and stability at the 10^{-18} level," Nature, vol. 506, pp. 71–75, 2014.

[4] N. Hinkley, J. A. Sherman, N. B. Phillips, M. Schioppo, N. D. Lemke, K. Beloy, M. Pizzocaro, C. W. Oates, and A. D. Ludlow, "An atomic clock with 10^{-18} instability," Science, vol. 341, pp. 1215–1218, 2013.

[5] T. Rosenband, D. B. Hume, P. O. Schmidt, C. W. Chou, A. Brusch, L. Lorini, W. H. Oskay, R. E. Drullinger, T. M. Fortier, J. E. Stalnaker, S. A. Diddams, W. C. Swann, N. R. Newbury, W. M. Itano, D. J. Wineland, and J. C Bergquist, "Frequency ratio of Al+ and Hg+ single-ion optical clocks; metrology at the 17th decimal place," Science, vol. 319, pp. 1808–1812, 2008.

[6] F. L. Walls, and D. W. Allan, "Measurements of frequency stability," Proceedings of the IEEE, vol. 74, pp. 162–168, 1986.

[7] S. A. Diddams, D. J. Jones, J. Ye, S. T. Cundiff, J. L. Hall, J. K. Ranka, R. S. Windeler, R. Holzwarth, T. Udem, and T. W. Hänsch, "Direct link between microwave and optical frequencies with a 300 THz Femtosecond laser comb," Phys. Rev. Lett. 84, 5102, 2000.

[8] S. Romisch, S. R. Jefferts, and T. E. Parker, "Towards an all-digital time scale," Proc. IEEE Frequency Control Symposium Joint with the EFTF, pp. 685–689, 2011.

[9] Z. Li, W. Zhou, H. Zhou, X. Zhang, and J. Zhao, "The optimization of super-high resolution frequency measurement techniques based on phase quantization regularities between any frequencies," Rev. Sci. Instrum. 84, 025106, 2013.

[10] W. Lewandowski, and C. Thomas, "GPS time transfer," Proceedings of the IEEE, vol. 79, pp. 991–1000, 1991.

[11] J. R. Ray, "IGS/BIPM time transfer pilot project," GPS Solutions, vol. 2, pp. 37–40, 1999.

[12] W. Lewandowski, and J. Azoubib, "Time transfer and TAI," Proc. IEEE/EIA IFCS 2000 Conference, pp. 586–597, 2000.

[13] S. Bregni, "Synchronization of digital telecommunications networks," Chichester, UK: John Wiley & Sons, 2002.

[14] T. Adam, et al, "Measurement of the neutrino velocity with the OPERA detector in the CNGS beam," arXiv:1109.4897v4, 2012.

[15] W. J. Riley, "Handbook of frequency stability analysis," NIST Special Publication 1065, 2008.

[16] D. W. Allan, N. Ashby, and C. C. Hodge, "The Science of Timekeeping," Hewlett Packard Application Note 1289, 1997.

[17] E. D. Kaplan, "Understanding GPS: principles and applications," Artech House, Boston, MA, 1996.

[18] J. Yao and J. Levine, "GPS carrier-phase time transfer boundary discontinuity investigation," Proc. 44th Annual Precise Time and Time Interval Systems and Applications (PTTI) Meeting, pp. 317–326, 2012.

[19] B. Hofmann-Wellenhof, H. Lichtenegger, E. Wasle, "GNSS global navigation satellite systems: GPS, GLONASS, Galileo and more," Springer, Berlin, 2008.

[20] J. Levine, "A review of time and frequency transfer methods," Metrologia, 45, pp. S162–S174, 2008.

[21] T. E. Parker, and D. Matsakis, "Time and frequency dissemination: advances in GPS transfer techniques," GPS World, November, pp. 32–38, 2004.

[22] D. W. Hanson, "Fundamentals of two-way time transfer by satellite", Proc. 43rd Annual Frequency Control Symposium, pp. 174–178, 1989.

[23] V. Zhang, T. E. Parker, J. Achkar, A. Bauch, L. Lorini, D. Matsakis, D. Piester, and D. G. Rovera, "Two-way satellite time and frequency transfer using 1 MChip/s codes," Proc. 41st PTTI Meeting, pp. 371–382, 2009.

[24] D. W. Allan and M. A. Weiss, "Accurate time and frequency transfer during common-view of a GPS satellite," Proc. 34th Ann. Freq. Control Symposium, 1980.

[25] D. W. Allan, M. A. Weiss, and N. Ashby, "Around-the-world relativistic sagnac experiment," Science, vol. 228, pp. 69–70, 1985.

[26] G. Petit and Z. Jiang, "GPS All in View time transfer for TAI computation," Metrologia, 45, pp. 35–45, 2008.

[27] K. M. Larson, and J. Levine, "Carrier-phase time transfer," IEEE Trans. Ultrason., Ferroelect., Freq. Contr., vol. 46, pp. 1001–1012, 1999.

[28] C. Hackman, J. Levine, T. E. Parker, D. Piester, and J. Becker, "A straightforward frequency-estimation technique for GPS carrier-phase time transfer," IEEE Trans. Ultrason., Ferroelect., Freq. Contr., vol. 53, pp. 1570–1583, 2006.

[29] P. Defraigne and C. Bruyninx, "On the link between GPS pseudorange noise and day-boundary discontinuities in geodetic time transfer solutions," GPS Solutions, vol. 11, pp. 239–249, 2007.

[30] K. Senior, E. Powers, and D. Matsakis, "Attenuating day-boundary discontinuities in GPS carrier-phase time transfer," Proc. 31st PTTI Meeting, pp. 481–490, 1999.

[31] N. Guyennon, G. Cerretto, P. Tavella, and F. Lahaye, "Further characterization of the time transfer capabilities of precise point positioning (PPP): the sliding batch procedure," IEEE Trans. Ultrason., Ferroelect., Freq. Contr., vol. 56, no. 8, pp. 1634–1641, 2009.

[32] M. Weiss, J. Yao, and J. Li, "In search of a new primary GPS receiver for NIST," Proc. 44th PTTI Meeting, pp. 179–186, 2012.

[33] R. Dach, G. Beutler, U. Hugentobler, S. Schaer, T. Schildknecht, T. Springer, G. Dudle, and L. Prost, "Time transfer using GPS carrier phase: error propagation and results," J. Geodesy, vol. 77, pp. 1–14, 2003.

[34] P. Misra, and P. Enge, "Global positioning system: signals, measurements, and performance (revised 2nd edition)," Ganga-Jamuna Press, Lincoln, MA, 2012.

[35] J. Zumberge, M. B. Hefflin, D. C. Jefferson, M. M. Watkins, F. H. Webb, "Precise point positioning for the efficient and robust analysis of GPS data from large networks," J. Geophys. Res., vol. 102, pp. 5005–5017, 1997.

[36] S. R. Jefferts, T. P. Heavner, T. E. Parker, and J. H. Shirley, "NIST Cesium fountains – current status and future prospects," Proc. of SPIE Vol. 6673, 667309, 2007.

[37] C. Hackman, J. Levine, and T. E. Parker, "A long-term comparison of GPS carrier-phase frequency transfer and two-way satellite time/frequency transfer," Proc. 38th PTTI Meeting, pp. 485–498, 2006.

[38] J. Kouba and P. Heroux, "Precise point positioning using IGS orbit and clock products," GPS Solutions, vol. 5, pp. 12–28, 2001.

[39] J. Kouba, "A guide to using International GNSS Service (IGS) products," IGS Central Bureau, Pasadena (available at ftp://ftp.igs.org/pub/resource/pubs/UsingIGSProductsVer21.pdf).

[40] http://igscb.jpl.nasa.gov/igscb/data/format/sp3_docu.txt.

[41] http://igscb.jpl.nasa.gov/igscb/data/format/rinex_clock300.txt

[42] http://igscb.jpl.nasa.gov/igscb/data/format/rinex210.txt

[43] C. Bruyninx, P. Defraigne, "Frequency transfer using GPS code and phases: short- and long-term stability," Proc. 31st PTTI Meeting, pp. 471–480, 1999.

[44] G. Petit, "The TAIPPP pilot experiment," Proc. EFTF-IFCS 2009 Joint Conference, pp. 116–119, 2009.

[45] Q. Baire, C. Bruyninx, P. Defraigne, and J. Legrand, "Precise point positioning with Atomium using IGS orbit and clock products: first results," Bulletin of Geodesy and Geomatics, vol. 69, n. 2-3, pp. 396–404, 2010.

[46] P. Defraigne, C. Bruyninx, and N. Guyennon, "PPP and phase-only GPS time and frequency transfer," Proc. IEEE Frequency Control Symposium Joint with the 21st EFTF, pp. 904–908, 2007.

[47] J. Yao and J. Levine, "A new algorithm to eliminate GPS carrier-phase time transfer boundary discontinuity," Proc. 45th PTTI Meeting, pp. 292–303, 2013.

[48] E. Mohino, M. Gende, C. Brunini, and M. Heraiz, "SiGOG: simulated GPS observation generator," GPS Solutions, vol. 9, pp. 250–254, 2005.

[49] J. Griffiths, and J. R. Ray, "On the precision and accuracy of IGS orbits," J. Geod., vol. 83, pp. 277–287, 2009.

[50] S. Datta-Barua, T. Walter, J. Blanch, and P. Enge, "Bounding higher-order ionosphere errors for the dual-frequency GPS user," Radio Science, vol. 43, RS5010, 2008.

[51] C. Hackman and J. Levine, "New frequency comparisons using GPS carrier-phase time transfer," Proc. IEEE IFCS 2003 Conference, pp. 258–265, 2003.

[52] J. Boehm, A. Niell, P. Tregoning, and H. Schuh, "Global mapping function (GMF): a new empirical mapping function based on numerical weather model data," Geophys. Res. Lett., vol. 33, L07304, 2006.

[53] M. Hottovy and M. Weiss, "Differential delay between two geodetic GPS receivers for L1 and L2 code and carrier signals," Proc. IEEE IFCS 2008 Conference, pp. 496–500, 2008.

[54] J. Yao, and J. Levine, "An improvement of RINEX-Shift algorithm for continuous GPS carrier-phase time transfer," Proc. 27th ION GNSS+ 2014 Conference, pp. 1253–1260, 2014.

[55] R. Dach, T. Schildknecht, T. Springer, G. Dudle, and L. Prost, "Continuous time transfer using GPS carrier phase," IEEE Trans. Ultrason., Ferroelect., Freq. Contr., vol. 49, no. 11, pp. 1480–1490, 2002.

[56] R. Dach, T. Schildknecht, U. Hugentobler, L.-G. Bernier, and G. Dudle, "Continuous geodetic time transfer analysis method," IEEE Trans. Ultrason., Ferroelect., Freq. Contr., vol. 53, no. 7, pp. 1250–1259, 2006.

[57] J. Delporte, F. Mercier, D. Laurichesse, and O. Galy, "GPS Carrier-Phase Time Transfer Using Single-Difference Integer Ambiguity Resolution," International Journal of Navigation and Observation, vol. 2008, Article ID 273785, 7 pages, 2008.

[58] J. Yao, and J. Levine, "GPS measurements anomaly and continuous GPS carrier-phase time transfer," To be published in Proc. 46th PTTI Meeting, 2014.

[59] V. Zhang, "GPS time and frequency transfer activities at NIST," 54th Civil GPS Service Interface Committee (CGSIC) Meeting, 2014.

[60] D. Matsakis, “Report from the U. S. Naval Observatory,” 53rd Civil GPS Service Interface Committee (CGSIC) Meeting, 2013.

[61] J. Jing, S. K. Khanafseh, F. C. Chan, S. Langel, and B. Pervan, “Detecting ionospheric gradients for GBAS using a null space monitor,” Proc. IEEE-ION PLANS, pp. 1125–1133, 2012.